Universidade Federal do Espírito Santo

Centro Tecnológico

Programa de Pós-Graduação em Engenharia Elétrica

Tiago Tadeu Wirtti

Adaptive X-ray Tomography Image Reconstruction

Vitória

2019

Tiago Tadeu Wirtti

Adaptive X-ray Tomography Image Reconstruction

PhD Thesis submitted to the Graduate Program in Electrical Engineering – PPGEE – of the Federal University of Espirito Santo – UFES – as partial fulfillment of the requirements to obtain the degree of Doctor of Philosophy in Electrical Engineering, in the research lines Biomedical Engineering and Signal Processing.

Universidade Federal do Espírito Santo

Centro Tecnológico

Programa de Pós-Graduação em Engenharia Elétrica

Advisor: Dr. Evandro Ottoni Teatini Salles

Vitória

2019

Ficha catalográfica disponibilizada pelo Sistema Integrado de
Bibliotecas - SIBI/UFES e elaborada pelo autor

W799a

Wirtti, Tiago Tadeu, 1972-
Adaptive X-ray Tomography Image Reconstruction / Tiago Tadeu Wirtti. - 2019.
96 f. : il.

Orientador: Evandro Ottoni Teatini Salles.
Tese (Doutorado em Engenharia Elétrica) - Universidade Federal do Espírito Santo, Centro Tecnológico.

1. Signal processing. 2. Biomedical engineering. 3. X-ray computed tomography. 4. Image reconstruction. 5. Optimization techniques. I. Salles, Evandro Ottoni Teatini. II. Universidade Federal do Espírito Santo. Centro Tecnológico. III. Título.

CDU: 621.3

Tiago Tadeu Wirtti

Adaptive X-ray Tomography Image Reconstruction

PhD Thesis submitted to the Graduate Program in Electrical Engineering – PPGEE – of the Federal University of Espirito Santo – UFES – as partial fulfillment of the requirements to obtain the degree of Doctor of Philosophy in Electrical Engineering, in the research lines Biomedical Engineering and Signal Processing.

Approved in August 8, 2019, by

Dr. Evandro Ottoni Teatini Salles
PPGEE/UFES – Advisor

Dr. Hae Yong Kim
USP, São Paulo/SP

Dr. Luiz Alberto Pinto
IFES, Serra/ES

Dr. Mário Sarcinelli Filho
PPGEE/UFES

Dr. Rodrigo Varejão Andreão
IFES, Vitória/ES

Vitória
2019

To Priscila, Antônia and Alberto

Acknowledgements

To the members of this Thesis examination board my sincere thanks for having accepted this invitation. I would also like to thank my Advisor, Dr. Evandro Ottoni Teattini Salles, for all the precious conversations, guidance and encouragement.

To my dear wife, Priscila, for all the support and unshakable confidence in this insane dream of trying to scratch the distant sky of knowledge. To Antonia, pure and loving daughter, for the lonely company during the long hours of intellectual reverie. To beautiful Alberto for taking me from the computer and guiding me to his small, affable little cartoon world. To all of them, my sincere thanks!

To my parents, for all the good they did (and do) for me and my brothers. To my brothers, Theo and Tatiana, for being my brothers, with all the good that comes with it. I am so grateful for that!

To my friends at ArcelorMittal Tubarão for all their support, my sincere thanks.

To my friends at LabCisne for sharing the good and the bad times of this arduous journey, my sincere thanks.

To my many friends from FAESA for encouraging me and wishing my success over these long years of dedication, my sincere thanks.

Finally, I warmly thank to the Federal University of Espírito Santo, and especially the PPGEE, for embracing me for so many years, definitely transforming me into a better version of myself.

"I enjoyed the rich color spectrum of the earth. It is surrounded by a light blue aureole that gradually darkens, becoming turquiose, dark blue, violet, and finally coal black." - Yuri Gagarin

Abstract

In X-ray tomography image reconstruction, one of the most successful approaches involves a statistical modeling with l_2 norm function for fidelity regularized by a functional with l_p norm, $1 < p < 2$, with $p \in \mathbb{R}$. Among them stands out, for its results and computational performance, a technique that reconstructs an image by alternating minimization for (i) solving the l_2 norm fidelity term by Simultaneous Algebraic Reconstruction Technique (SART) and (ii) constraining the regularization term, defined by a Discrete Gradient Transform (DGT) sparse transformation, using Total Variation (TV) minimization. This work proposes an improvement to the reconstruction process by adding a Bilateral Edge-preserving (BEP) regularization term to the objective function, resulting in a three-step method. BEP is a noise reduction framework and has the purpose of adaptively eliminating noise in the initial phase of reconstruction process. BEP improves optimization of the fidelity term and, as a consequence, improves the result of DGT minimization by total variation. Regular dosage experiments shown favorable results compared to classical methods, such as Filtred Backprojection (FBP), and more modern ones, such as l_2 norm optimization by using SART, and the l_2 norm SART solution regularized by l_1 norm TV optimization of DGT (SART+DGT), especially with the Structural Similarity Index Measurement (SSIM) metric. Although not so prominent in the case of regular dosing reconstruction, Peak Signal-to-noise Ratio (PSNR) results are consistent with those of SSIM. For low dosage, the quality of the reconstruction worsens for all methods, but is markedly lower for the FBP and SART methods. In this context of limited number of projections (low dosage), the reconstructions with the method here proposed presents better defined edges, in addition to better contrast and less artifacts in surfaces of regular intensity (low intensity variation). These results are generally obtained with a smaller number of steps compared to the other iterative methods implemented in this Thesis. However, this behavior (of the proposed method) depends on the parameterization of the l_p norm, $1 \leq p \leq 2$, used in the BEP stage. It is experimentally shown that by varying the norm during the reconstruction process it is possible to keep the proposed method stable over a sufficiently large number of iteractions. It is also graphically shown that the method converge, meaning that the SSIM and PSNR metrics can be continuously improved by a sufficiently large number of iteractions. For reconstructions with a limited number of projections (low-dose reconstruction), the proposed method can achieve higher PSNR and SSIM results because it can better control the noise in the initial processing phase.

Keywords: Signal processing, Biomedical engineering, X-ray computed tomography, Image reconstruction, Optimization techniques, Bilateral edge preservation

Resumo

Em reconstrução de imagem de tomografica de raios-X, uma das abordagens mais bem sucedidas envolve a modelagem estatística de uma função fidelidade de norma l_2 combinada com algum tipo de regularização de norma l_p, $1 < p < 2$, onde $p \in \mathbb{R}$. Entre elas, se destaca por seus resultados e desempenho computacional uma técnica que envolve minimização alternada entre (i) a solução da função fidelidade de norma l_2 pela técnica de reconstrução algébrica simultânea (SART, simultaneous algebraic reconstruction technique) e (ii) a solução de um termo regularizador que usa transformação gradiente discreta (DGT, discrete gradient transform) minimizada por variação total (TV, total variation). O presente trabalho propõe a melhoria desse processo de reconstrução através da adição à função objetivo de um termo baseado em preservação bilateral de bordas (BEP, bilateral edge preservation), resultando em um método de três etapas. BEP é uma metodologia de redução de ruído e tem o propósito de eliminar de forma adaptativa o ruído na fase inicial do processo de reconstrução. Como consequência, a adição de BEP melhora a otimização do termo de fidelidade e o resultado da minimização da DGT por variação total. Experimentos com dosagem regular mostram resultados favoráveis em comparação com métodos clássicos, tais como Retroprojeção com Filtragem (Filtered Backprojection, ou FBP) e outros mais modernos, tais como solução por otimização de norma l_2 por SART, especialmente para a métrica SSIM. Embora não sejam proemintes no caso de reconstrução com dosagem regular, os resultados com PSNR são coerentes com os do SSIM. Para baixa dosagem, a qualidade da rescontrução piora para todos os métodos, mas é notadamente inferior para FBP e SART. Neste contexto de número limitado de projeções (baixa dosagem), o método proposto apresenta reconstruções com bordas mais bem definidas, além de melhor constraste e menos artefatos em superfícies regulares (pouca variação de intensidade). Esses resultados são obtidos geralmente com um menor número de iterações em comparação com os demais métodos implementados nesta Tese. É experimentalmente mostrado que variando a norma no decorrer do processo de reconstrução é possível manter o método proposto estável ao longo de um número suficientemente grande de iterações. Para reconstruções com um número limitado de projeções (reconstrução de baixa dosagem), o método proposto pode alcançar resultados consideráveis em termos de PSNR e SSIM devido à possibilidade de controlar melhor o ruído na fase inicial do processo de reconstrução.

Palavras-chave: Processamento de sinal, Engenharia biomédica, Tomografia computadorizada de raios-X, Reconstrução de imagem, Técnicas de otimização, Preservação bilateral de bordas

List of Figures

List of Tables

List of abbreviations and acronyms

ALARA	As-low-as-reasonably-achievable
AMP	Approximate message passing
ART	Algebraic reconstruction technique
BEP	Bilateral edge preserving
BTV	Bilateral total variation
CT	Computer tomography
DGT	Discrete gradient transform
FBP	Filtered backprojection
FFT	Fast Fourier transform
MAP	Maximum a posteriori
MMSE	Minimum mean square error
ML	Maximum likelihood
OS-SART	Ordered subset – Simultaneous algebraic reconstruction technique
PSNR	Peak signal-to-noise ratio
TV	Total variation
SART	Simultaneous algebraic reconstruction technique
SNR	Signal-to-noise ratio
SSIM	Structural similarity
VW-SART	Variable weighted simultaneous algebraic reconstruction technique

List of symbols

$\boldsymbol{\mu}$	original synthetic image (vector of attenuation coefficients)
$\mathcal{N}_p$	Poisson degradation
$\mathcal{N}_g$	Gaussian noise
$\mathcal{R}\left(.\right)$	Radon transform
$\boldsymbol{y}_{\mathcal{N}}$	noisy generated input signal
I_0	number of detected photons when the beam finds no obstacle
N_I	maximum number of projections
i	index of CT projections
L_i	line of integration of projection i
ΔL	thickness of a slice of material
$\sum\limits_{L_i}$	summation over the line L_i
$\int\limits_{L_i}$	integral over the line L_i
I_i	count of detected photons over integral line L_i
(x, y)	2-D coordinates in reconstructed image
$\mu(x, y)$	attenuation coefficient in (x, y)
N_J	maximum number of pixels in reconstructed image
j	index of pixels of an image
p_i	i-th projection, integral of $\mu\left(x, y\right)$ over L_i
$\hat{p}_i$	estimate of p_i
$\mathbf{A}$	matrix representing the system geometry
a_{ij}	element in position (i, j) in matrix $\mathbf{A}$
y_i	projection along the i-th X-rays beam
$\bar{y}_i$	expected value of y_i

$\mathbf{y}$	a vector of y_i
$P\left(\mathbf{y}\vert\boldsymbol{\mu}\right)$	joint probability of $\mathbf{y}$ given $\boldsymbol{\mu}$
$\mathcal{H}$	notation for Hilbert space
$\left(\varphi_\gamma\right)_{\gamma\in\Gamma}$	an orthogonal basis in the Hilbert space $\mathcal{H}$
$\prod_{i=1}^{N_I}(.)$	product of all terms (.) from $i = 1$ to N_I
$\Phi\left(\boldsymbol{\mu}\right)$	objective function of $\boldsymbol{\mu}$
$R_{DGT}\left(\boldsymbol{\mu}\right)$	regularization term based on DGT function
H	maximum number of rows in the matrix image
m	any row in an image with $m = 1, 2, ..., H$ rows
W	maximum number of columns in the matrix image
n	any column in an image with $m = 1, 2, ..., W$ columns
$D_{m,n}\boldsymbol{\mu}$	DGT function of $\boldsymbol{\mu}$, same as $D_j\boldsymbol{\mu}$ with $j = (m-1)\times W + n$
$TV\left(\boldsymbol{\mu}\right)$	total variation of $\boldsymbol{\mu}$
$\Lambda = diag(.)$	diagonal matrix of (.) elements
$\mathbf{A}_\Lambda$	matrix $\mathbf{A}$ diagonalized, same as $\Lambda\mathbf{A}$
$\hat{\boldsymbol{p}}$	a vector of $\hat{p}_i$ elements, with $i = 1$ to N_I
$\Vert.\Vert_2^2$	l_2 norm
$\Vert.\Vert_1$	l_1 norm
$\Vert.\Vert^p$	l_p norm
$F\left(\boldsymbol{\mu}\right)$	fidelity term in function of $\boldsymbol{\mu}$
$\tilde{\boldsymbol{\mu}}$	result of optimization of $F\left(\boldsymbol{\mu}\right)$
$\boldsymbol{X}$	image in reconstruction/regularization
$R_{BTV}\left(\mathbf{X}\right)$	Bilateral total variation (BTV) regularization function over $\boldsymbol{X}$
S_x^l	displacements by l pixels in the horizontal direction
S_y^m	displacements by m pixels in the vertical direction
α	spatial decay effect for the sum of terms in BTV regularization

$\rho\left(.\right)$	BEP regularization function
$\psi\left(.\right)$	Influence function of $\rho\left(.\right)$
$R_{BEP}\left(\tilde{\boldsymbol{\mu}}\right)$	Bilateral edge preserving operator over $\tilde{\boldsymbol{\mu}}$
$\tilde{\mu}_j$	j-th pixel of image $\tilde{\boldsymbol{\mu}}$
$\rho_a\left(s\right)$	same as $\rho\left(a,s\right)$, with a being an adjustment term and s the difference to be adjusted
$\boldsymbol{\sigma}$	auxiliary variable representing $R_{BEP}\left(\tilde{\boldsymbol{\mu}}\right)$
γ	positive adjustment parameter to balance the terms of fidelity and adaptive regularization
$\left\Vert\left(.\right)\right\Vert_\eta$	norm l_η of $\left(.\right)$, with $1 \leq \eta \leq 2$
$\tilde{\mu}_j^k$	k-th estimate of $\tilde{\mu}_j$
a_{+j}	short notation for $\sum_{i=1}^{N_I} a_{ij}$, $j = 1, 2, ..., N_J$
a_{+i}	short notation for $\sum_{j=1}^{N_J} a_{ij}$, $i = 1, 2, ..., N_I$
$\boldsymbol{\Lambda^{+N_J}}$	diagonal matrix with $\Lambda_{jj}^{+N_J} = \frac{1}{a_{+j}}$
$\boldsymbol{\Lambda^{+N_I}}$	diagonal matrix with $\Lambda_{ii}^{+N_I} = \frac{1}{a_{+i}}$
$\hat{\boldsymbol{\mu}}$	result of optimization of $\tilde{\boldsymbol{\mu}}$ by gradient descent using BEP
$\triangledown R_{BEP}$	gradient descent contribution
φ	adjustment parameter that balances terms inside gradient descent
$\odot$	element-by-element product of two matrices of compatible dimensions
ω	threshold in TV soft-threshold filtering method
$\boldsymbol{\Theta}$	set of angles in CT scan process

Contents

1 Introduction

X-ray computer tomography (CT) measures the attenuation of X-ray beams passing through an object, generating projections. Such projections are processed, resulting in an image (slice) of the examined object. This is known as CT image reconstruction. The CT scan, formed by concatenating a large number of adjacent reconstructed images, has been proven to have great value in delivering rapid and accurate diagnoses for many diseases in modern medicine. The central theme of this work is the reconstruction of images generated by the CT equipment, where the X-ray dosage is a concern. In this chapter we will reinforce the importance of low dosage in X-ray CT, to develop in the reader the fundamental concepts of acquisition and mathematical modeling of CT image reconstruction. In addition, we will present the most important classical, iterative, statistical techniques and understand how CT image reconstruction has evolved to the current state of the art.

1.1 The "as-low-as-reasonably-achievable" – ALARA – principle

Although CT scanning has evolved considerably since its creation in 1972 by Godfrey Hounsfield, the risk associated with the long-term effects of radiation exposure during CT exams is still of great concern to the medical community, especially in children (BRODY et al., 2007; PEARCE et al., 2012; MIGLIORETTI et al., 2013). Reinforcing this view, CT scans accounts for a considerable portion of radiation exposure related to medical imaging, and medical professionals should have a working knowledge of the benefits and risks of medical radiation (COSTELLO et al., 2013). Radiation doses for CT vary significantly between patients, institutions, and countries. CT scans uses ionizing radiation, a known carcinogen, and, for this reason, is associated with increased cancer incidence. In addition, absorbed radiation in tissues from CT is among the highest observed from diagnostic radiology, and, to reinforce the concern, participation in CT scans has doubled in the last two decades (SMITH-BINDMAN et al., 2019). Despite this, radiation doses in CT scans have not decreased as it has happened in conventional radiography (KIM et al., 2016).

General concern about radiation levels in radiological examinations led to the "as-low-as-reasonably-achievable" principle (known as the ALARA principle), which states that only the minimum amount of radiation should be applied to the patient. For this reason, ALARA is widely accepted in the medical CT community (NEWMAN; CALLAHAN, 2011; PEARCE et al., 2012; MAYO-SMITH et al., 2014; SODHI et al., 2015; YEUNG, 2019). To reduce the X-ray dose of the patient during the CT scan, there are two possibilities: (1) reduce the amount of projections (the quantity of X-rays emitted) during the CT scan or (2) reduce the power of the X-ray source during the image acquisition. Both cases generally lead to low-quality reconstructed CT images. Then, a state-of-the-art problem is to propose a method that allows good-quality CT image reconstruction with a low-dose X-ray source. Before discussing CT image reconstruction approaches with low-dose X-rays, we present in the next section the signal aquisition model for CT.

1.2 CT aquisition model and modeling considerations

Tomography, from the Greek *thomos* (slice, section) and *graphos* (pictorial representation), consists of indirectly obtaining a graphic representation (image) of a transverse slice in an object. More specifically, the data is acquired by beams (bundles of rays) that run through lines on a slice in the object at different angles, such as θ_1 and θ_2, (see Figure 1). Part of the beams is absorbed by the material and part survives to reach the detectors, generating projections, such as $\mathbf{p}(\boldsymbol{r}, \boldsymbol{\theta_1})$ and $\mathbf{p}(\boldsymbol{r}, \boldsymbol{\theta_2})$, as ilustrated in Figure 1.

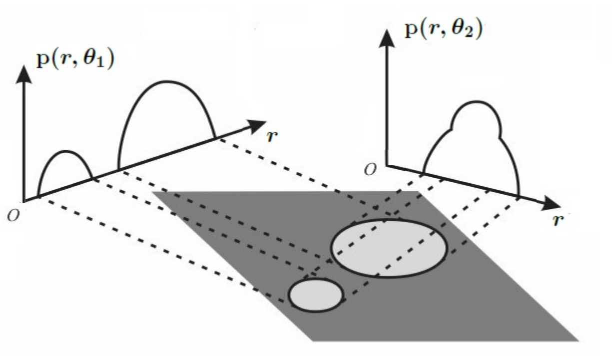

Figure 1 – Projections at differente view-angles.

On X-ray computed tomography (X-ray CT), these beams are composed of X-ray photons. The process of X-ray emission is in the field of physics. X-ray photons are produced when a substance is bombarded by high-speed electrons. X-ray photon emission is a rare event and up to 99% of the input energy is converted to heat. The diagnostic X-rays varies wavelength from 0.1 nm to 0.01 nm, corresponding to an energy range of 12.4 keV to 124 keV. The energy, E, of an X-ray photon is proportional to its frequency, f, and is expressed as

$$E = hf = \frac{hc}{\lambda}, \tag{1.1}$$

where h is Planck's constant (6.63×10^-34 Js), c is the light speed (3×10^8 m/s), and λ is the wavelength of the X-ray (HSIEH, 2009a).

Before embarking on the details of data acquisition on CT equipment, it is briefly presented the most popular CT sampling geometries, commonly known as CT architectures. Figure 2a,b,c shows, respectively, the parallel beam, fan beam and cone beam architectures (HSIEH, 2009a). It is wise to have several detectors for a few (or even one) emitters (sources).

This is related to the cost of CT equipment. Therefore, cone beam-type equipment is widely used in the real world. However, for the sake of simplicity, without losing the generality, this work will use parallel architecture for mathematical simplicity.

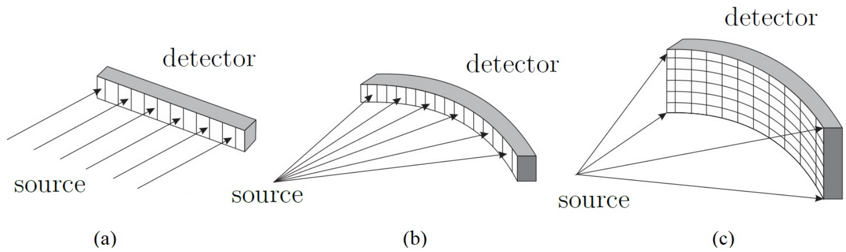

Figure 2 – (**a**) Parallel beam, (**b**) fan beam, and (**c**) cone beam architectures for CT scanners.

Most modern CT scanners uses energy integration detectors whose photon counts are proportional to the total energy incident on them. Energy, in turn, is proportional to the number of X-ray photons that affect the detectors (sensors) of the tomograph. X-ray beams passing through any material may be partially or totally retained, an effect known as attenuation. Each material has properties that influence the amount of photons it can hold or let pass. Such properties can be expressed as the material attenuation coefficient, μ. Let I_i be the intensity of the incident (detected) X-rays in a line L_i, I_0 the intensity transmitted (generated), ΔL the (constant) thickness of each slice of the material and μ_1 , μ_2 , ... , μ_N, the specific attenuation coefficients of each material, as ilustrated in Figure 3.

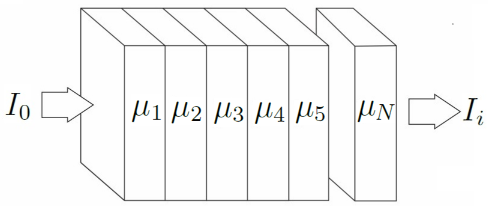

Figure 3 – X-ray attenuation through different materials.

Then, the relation between the detected, I_i, and generated I_0 beams, known as the Beer-Lambert law (SWINEHART, 1962), is given by:

$$I_i = I_0 exp\left(-\left(\mu_1 + \mu_2 + ... + \mu_N\right)\Delta L\right) = I_0 exp\left(-\sum_{L_i} \mu_{L_i}\Delta L\right), \tag{1.2}$$

where L_i is the path of the X-ray beam through the material. When we make ΔL very small (making the slices of the scanned object very thin), tending to zero, we have

$$I_i = I_0 exp\left(-\int_{L_i} \mu\left(x, y\right) dL\right). \tag{1.3}$$

It is straightforward to observe that the intensity, I_i, is inversely proportional to the sum of the attenuations, $\mu\left(x, y\right)$, on the integration line, L_i, where the pair (x, y) denotes coordinates inside de scanned area, as shown in Figure 4. Through simple manipulations of Equation (1.3), we have

$$p_i = -\ln\left(\frac{I_i}{I_0}\right) = \int_{L_i} \mu(x, y)\, dL, \tag{1.4}$$

where p_i, is the projection resulting from the CT acquisition process over the integral line, L_i.

Up to this point, we have modeled the process of obtaining the signal, I_i, in Equation (1.3), in a detector, as well as its projection, p_i, in Equation (1.4). Now we can explore the model of signal acquisition in an ideal CT equipment using as an inspiration Figure 4. First, we use parallel architecture, in which the relation between emitters (X-ray source) and detectors is one-to-one. However, the modeling developed here can easily be adapted to other architectures such as fan beam and cone beam (HSIEH, 2009a; SUETENS, 2009). The section area (Figure 4) corresponds to the scanned region and, after reconstruction, will result in an image of 512 × 512 pixels. The X-ray source has $n_p = 300$ emitters that cast parallel beams over the section area, reaching the detectors on the other side of the scanned object, generating projections $\mathbf{p}(\boldsymbol{r}, \boldsymbol{\theta}) = \{p_i\}$, with $i = 1, ..., np$, $i \in \mathbb{N}^+$, and $(\boldsymbol{r}, \boldsymbol{\theta})$ being the polar coordenates of any projection in relation to $(\boldsymbol{x}, \boldsymbol{y})$ coordinate system. In detail, each beam traverses a line of integration, L_i (the red line, for instance), resulting in a projection p_i (shown as a blue line). The projection, p_i, as indicated by Equation (1.4), is directly proportional to the sum of the attenuation coefficients, $\mu(x, y)$, of the materials reached on the integration line, as ilustrated in Figure 4.

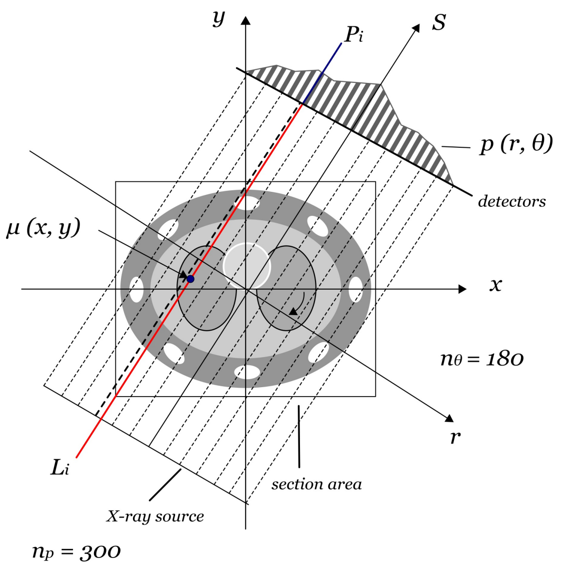

Figure 4 – Aquisition model. In red it is represented the integral line composed of all the intensities, $\mu(x, y)$, that generate the projection, p_i.

The generation of the array of projections $\mathbf{p}(\boldsymbol{r}, \boldsymbol{\theta})$ should be done for all the angles, $\boldsymbol{\theta} = \{\theta_i\}$, with $i = 1, ..., n_\theta$, $i \in \mathbb{N}^+$, and $n_\theta = 180$, assuming that a complete (180°) scan will be performed. In the next section we discretize the aquisition problem and derive the Maximum a Posteriori (MAP) model.

1.3 Acquisition problem discretization and Bayesian model derivation

The key aspect of the modeling process is that reconstruction estimates the discrete attenuation, $\mu(x,y)$ for each j pixel of the image, with $j = 1, ..., N_J$. Thus, the integral over the line, $p_i = \int\limits_{L_i} \mu(x,y)\, dL$, Equation (1.4), can be discretized as

$$p_i \approx \sum_{j=1}^{N_J} a_{ij}\mu_j = [\mathbf{A}\boldsymbol{\mu}]_i \,, i = 1, ..., N_I, \tag{1.5}$$

where $\mathbf{A} = \{a_{ij}\}_{N_I \times N_J}$ is the matrix representing the system geometry, $N_I = n_p n_\theta$ is the total number of projections acquired (n_p projections for each n_θ angles), $[\boldsymbol{\mu} = \mu_1 ... \mu_{N_J}]^T$ is the linear attenuation coefficient vector with μ_j representing the j-th pixel. In this model, every a_{ij} is defined as the normalized length of the intersection between the i-th projection beam and the j-th rectangular pixel centered in (x,y), as ilustrated in Figure 5.

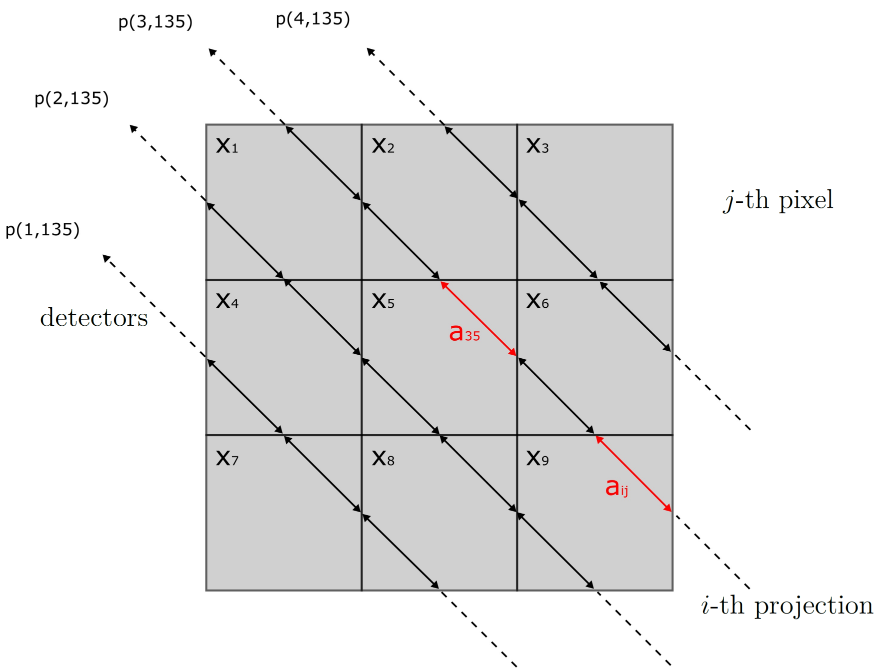

Figure 5 – Representation of an element a_{ij} of the system matrix $\mathbf{A}$. For instance, element a_{35} represents the size of intersection between projection $\mathrm{p}(3,135)$, in line 3, and the area of pixel x_5.

As a didactic effort, we present in Figure 6 a sequence of 5 scans separated from each other by angles of 45°, with each scan presenting 4 projection lines on an image (to be reconstructed) of dimensions 3×3.

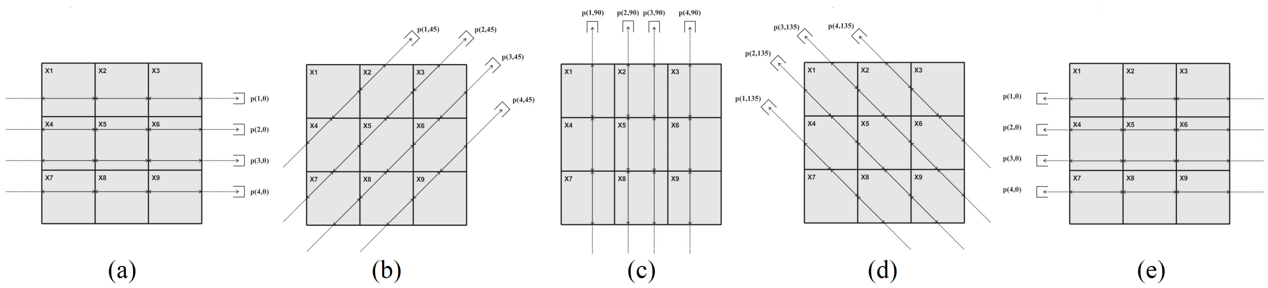

Figure 6 – Didactic representation of a sequence of 5 scans separated by angles of 45°, with 4 projections each, on an image of dimensions 3×3.

Therefore, from the example of Figure 6, we have the projection vector $\mathbf{P}_{N_I 1}$ with dimensions 20×1 (see Figure 7), where each of the 5 scans of Figure 6 contributes with 4 projection values. The vector $\boldsymbol{\mu}_{N_J 1}$, in Figure 7, represents the image to be reconstructed, with dimensions 9×1. Like the projection vector, $\boldsymbol{\mu}_{N_J 1}$ is represented lexicographically[1]. The system matrix $\mathbf{A}_{N_I N_J}$, as ilustrated in Figure 7, has dimensions $N_I N_J$, and its coeficientes a_{ij} are obtained as previously explained in Figure 5. Finally, the vector $\mathbf{e}_{N_J 1}$ represents the error in the reconstruction processes. It is noteworthy that each projection illustrated in Figure 6 is represented as an equation in the system of Figure 7 with coefficients in each row of matrix $\mathbf{A}$ and unknowns in the vector $\boldsymbol{\mu}$.

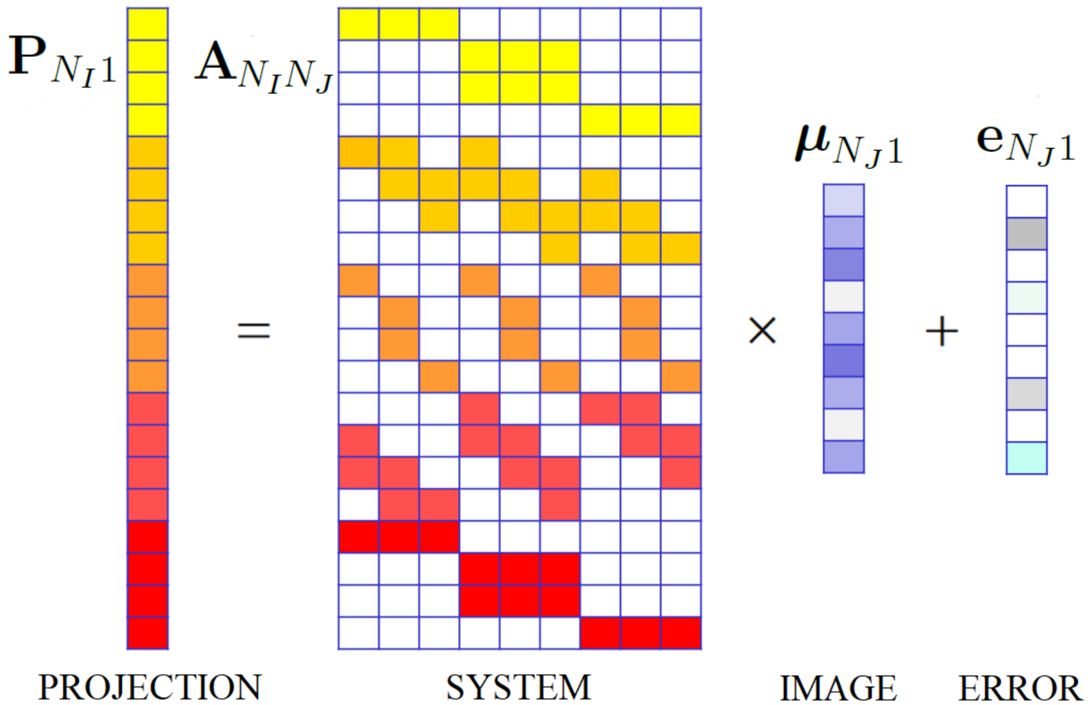

Figure 7 – Didactic representation of the inverse problem of CT image reconstruction, where $\mathbf{P}_{N_I 1}$ is the projection vector, $\boldsymbol{\mu}_{N_J 1}$ is the image to be reconstructed, $\mathbf{A}_{N_I N_J}$ is the system matrix, and $\mathbf{e}_{N_J 1}$ is the error inherent in the process.

[1] To represent lexicographically a matrix consists of stacking the columns of the matrix with dimensions (m, n) from the first to the last column, forming a column vector of dimensions $(mn, 1)$.

The emission of X-ray photons is a rare event, so a Poisson distribution is usually adopted to describe the probabilistic model (HSIEH, 2009b), expressed as

$$y_i \sim \text{Poisson}\left\{\bar{y}_i = I_0 e^{-p_i}\right\}, i = 1, ..., N_I \tag{1.6}$$

where y_i is the projection (measurement) along the i-th X-rays beam and $\bar{y}_i$ is its expected value. Because the X-rays beams are independent one from each other, taking into account Equation (1.6) the joint probability of $\mathbf{y} = \{y_1, y_2, ..., y_{N_I}\}$ given $\boldsymbol{\mu}$, $P(\mathbf{y}|\boldsymbol{\mu})$, observing y_i countable events, may be expressed as

$$P(\mathbf{y}|\boldsymbol{\mu}) = \prod_{i=1}^{N_I} P(y_i|\boldsymbol{\mu}) = \prod_{i=1}^{N_I} \left(\frac{(\bar{y}_i)^{y_i}}{y_i!} e^{-\bar{y}_i} \right). \tag{1.7}$$

Applying the ln operator to Equation (1.7), we have

$$L(\mathbf{y}|\boldsymbol{\mu}) = \ln P(\mathbf{y}|\boldsymbol{\mu}) = \sum_{i=1}^{N_I} \left(y_i \ln\left(I_0 e^{-p_i}\right) - I_0 e^{-p_i} - \ln y_i! \right), \tag{1.8}$$

and, by eliminating the constant terms, using Equation (1.5), we obtain

$$L(\mathbf{y}|\boldsymbol{\mu}) = -\sum_{i=1}^{N_I} \left(y_i p_i + I_0 e^{-p_i} \right) = -\sum_{i=1}^{N_I} \left(y_i \left[\mathbf{A}\boldsymbol{\mu}\right]_i + I_0 e^{-\left[\mathbf{A}\boldsymbol{\mu}\right]_i} \right). \tag{1.9}$$

Applying the Bayesian rule to CT reconstruction (ELBAKRI; FESSLER, 2002; YU; WANG, 2009; XU et al., 2011), we have

$$P(\boldsymbol{\mu}|\mathbf{y}) = \frac{P(\mathbf{y}|\boldsymbol{\mu})\, P(\boldsymbol{\mu})}{P(\mathbf{y})}, \tag{1.10}$$

and the original image, $\boldsymbol{\mu}$, can be reconstructed obtaining the Maximum a Posteriori (MAP) of function $P(\boldsymbol{\mu}|\mathbf{y})$. The natural logarithm is monotonically increasing, so the maximization of a posterior $P(\boldsymbol{\mu}|\mathbf{y})$ can be obtained by maximizing its logarithm. Applying the $\ln(.)$ operator to Equation (1.10), we have

$$\hat{\Phi}(\boldsymbol{\mu}) = L(\mathbf{y}|\boldsymbol{\mu}) + \ln\left(P(\boldsymbol{\mu})\right) - \ln\left(P(\mathbf{y})\right), \tag{1.11}$$

where $L(\mathbf{y}|\boldsymbol{\mu})$ is defined in Equation (1.9), and the term related to $P(\mathbf{y})$ can be disregarded for the optimization problem, since it is a known value, adding only offset to $\hat{\Phi}(\boldsymbol{\mu})$. In the optimization problem the term $L(\mathbf{y}|\boldsymbol{\mu})$ is known as the fidelity term, and its optimization corresponds to the Maximum Likelihood (ML) problem. The term $\ln(P(\boldsymbol{\mu}))$ expresses the prior knowledge on the problem and aim to restrict the solutions to a set that approaches the ideal solution. Therefore, $\ln(P(\boldsymbol{\mu}))$ is a regularizing term and, by rewriting $-\ln(P(\boldsymbol{\mu}))$ as $R(\boldsymbol{\mu})$ we have

$$\hat{\Phi}(\boldsymbol{\mu}) = -\sum_{i=1}^{N_I} \left(y_i \left[\mathbf{A}\boldsymbol{\mu}\right]_i + I_0 e^{-\left[\mathbf{A}\boldsymbol{\mu}\right]_i} \right) - R(\boldsymbol{\mu}). \tag{1.12}$$

Maximize Equation (1.12) is the same as minimize

$$\Phi(\boldsymbol{\mu}) = \sum_{i=1}^{N_I} \left(y_i \left[\mathbf{A}\boldsymbol{\mu} \right]_i + I_0 e^{-[\mathbf{A}\boldsymbol{\mu}]_i} \right) + R(\boldsymbol{\mu}). \tag{1.13}$$

However, working with Equation (1.13) is uncomfortable, since it presents an exponecial term, difficult to manipulate. Applying a second-order Taylor's expansion to $h_i(p_i) = y_i p_i + I_0 e^{-p_i}$, and $\hat{p}_i = \ln\left(\frac{I_0}{y_i}\right)$, we have

$$\begin{aligned} h_i(p_i) &\approx h_i(\hat{p}_i) + \dot{h}_i(p_i)(p_i - \hat{p}_i) + \frac{\ddot{h}_i(p_i)}{2}(p_i - \hat{p}_i)^2 = \\ &= y_i \ln\left(\frac{I_0}{y_i}\right) + y_i + \frac{1}{2} y_i (p_i - \hat{p}_i)^2. \end{aligned} \tag{1.14}$$

Eliminating the irrelevant terms to the optimization process and using the expansion promoted by Equation (1.14), we have the fidelity (or discrepancy) term, $F(\boldsymbol{\mu})$, defined as

$$F(\boldsymbol{\mu}) = \sum_{i=1}^{N_I} \frac{y_i}{2} \left([\mathbf{A}\boldsymbol{\mu}]_i - \hat{p}_i \right)^2, \tag{1.15}$$

and Equation (1.13) becomes

$$\begin{aligned} \Phi(\boldsymbol{\mu}) &= F(\boldsymbol{\mu}) + R(\boldsymbol{\mu}) \\ &= \sum_{i=1}^{N_I} \frac{y_i}{2} \left([\mathbf{A}\boldsymbol{\mu}]_i - \hat{p}_i \right)^2 + R(\boldsymbol{\mu}). \end{aligned} \tag{1.16}$$

Obtaining $\boldsymbol{\mu}$ from $F(\boldsymbol{\mu})$ is an inverse problem. According to Daubechies et al. (2004), such problems can be solved using a generalized inverse operator. However, this type of operator may be unbounded (ill-posed problem) or present very large norm (ill-conditioned problem). In such cases, the generalized inverse operator has to be replaced by a bounded or with smaller norm approximants, so that numerically stable solutions can be defined and used as approximations of the true solution correspondig to the exact data. This is known as regularization, and is performed by optimizing the term $R(\boldsymbol{\mu})$ in Equation (1.16) with a l_p norm, $1 \leq p < 2$. Next, we present a discussion on norm regularization and optimization and relate norm with sparsity.

1.4 Norm optimization considerations

Solving the inverse problem of Equation (1.15) implies a l_2 norm optimization. Functions that minimize $F(\boldsymbol{\mu})$ are called pseudosolutions of the inverse problem (DAUBECHIES et al., 2004). Such solutions generally produces blurred images with poorly defined edges, since the l_2 norm solution behaves like a low-pass filter. In addition, the CT reconstruction problem is considered as ill-posed, sparse and presents systems of large dimensions, as discussed in Section 1.3. Just for the sake of illustration, the optimization problem proposed in Equation (1.15) can be represented by Figure 8. The goal is to find the global minimum, f^{∞}, starting from a initial condition, f^{0}, through the minimization of $||Kf - g||^2$, where K represents the system description, f is the unknown, and g is a projection of the system's solution. In such systems there are several solutions, corresponding to the lower region of Figure 8 (the valley region). One can expect intuitively that a good solution starts from a good initial condition, and this is usually true. However, in real CT reconstruction problems it is not easy to define a good initial condition. These difficulties lead to the need of adding a constraining function in order to mitigate the unboundness (ill-poseness) of the optimization problem, as proposed in Equation (1.16). The constraint of the objective function limits the possible solutions to a set that is physically possible. As an example, the intensity of a pixel must be within a finite range, a pixel cannot assume negative values, or the difference between neighboring pixels should not be greater than a given value. An interesting point of arguement is that if for a simple solution like that of Figure 8 there is a well-established dependence between the solution and the initial conditions, a relationship that tends to become more intricate for real and more complex problems such as CT reconstruction.

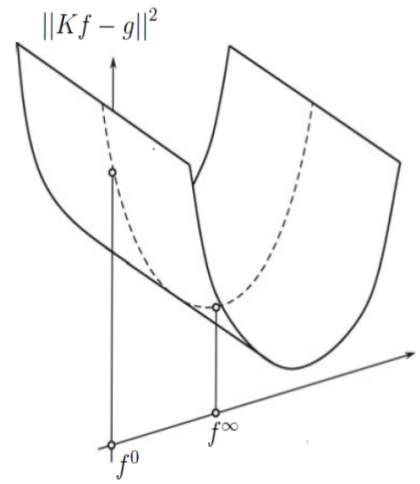

Figure 8 – Exemplifying the problem of limitating solutions of an overdeterminated system.

Daubechies et al. (2004) proposed a penalization term that is a weighted l_p norm, $1 \leq p \leq 2$, of the coefficients of $\boldsymbol{\mu}$ with respect to a orthonormal basis of $\mathcal{H}$, where $\mathcal{H}$ is a Hilbert space[2]. Formally, given an orthogonal basis $(\varphi_\gamma)_{\gamma\in\Gamma}$ in the domain of $\mathcal{H}$ and a sequence of positive real weights $\mathbf{w} = (w_\gamma)_{\gamma\in\Gamma}$, the functional $\Phi_{\mathbf{w},\mathrm{p}}$ can be defined as

$$\Phi_{\mathbf{w},\mathrm{p}}(\boldsymbol{\mu}) = F(\boldsymbol{\mu}) + \sum_{\gamma\in\Gamma} w_\gamma \left|\langle \boldsymbol{\mu}, \varphi_\gamma \rangle\right|^p, \tag{1.17}$$

[2] A Hilbert space generalizes the notion of Euclidean space to multidimensional spaces and is usually defined as an abstract vector space structured as an inner product that allows length and angle measurements.

where $F(\boldsymbol{\mu})$ is defined in Equation (1.15), and $\boldsymbol{\mu}$ is the image we intend to unveil.

For the particular case of $p = 2$ and $w_\gamma = \beta$ (constant) for all $\gamma \in \Gamma$, we have

$$\Phi_{\mathbf{w},\mathrm{p}=2}(\boldsymbol{\mu}) = F(\boldsymbol{\mu}) + \beta \, ||\triangledown \boldsymbol{\mu}||_2^2 \, , \tag{1.18}$$

where $||\triangledown \boldsymbol{\mu}||_2^2$ denotes a l_2 norm regularization functional to $\Phi_{\mathbf{w},\mathrm{p}=2}(\boldsymbol{\mu})$. The penalty function in Equation (1.18) is suitable when we know previously the image to be reconstructed should be smooth, that is, the constraining function $||\triangledown \boldsymbol{\mu}||_2^2$ suppresses the significant differences and preserves the smooth transitions between pixels. Thinking now to the other extreme, when $p = 1$, the objective function of Equation (1.17) can be rewritten as

$$\Phi_{\mathbf{w},\mathrm{p}=1}(\boldsymbol{\mu}) = F(\boldsymbol{\mu}) + \beta \, ||\triangledown \boldsymbol{\mu}||_1 \, , \tag{1.19}$$

where, in analogy to Equation (1.18), $||\triangledown \boldsymbol{\mu}||_1$ denotes a l_1 norm regularization functional to $\Phi_{\mathbf{w},\mathrm{p}=1}(\boldsymbol{\mu})$. In this case, the penalty function $||\triangledown \boldsymbol{\mu}||_1$ tends to preserve the significant differences between pixels, but smooth areas may suffer some disturbance. Indeed, regularization with l_1 norm often leads to the piecewise constant result and hence will produce artificial edges on the smooth areas (CHARBONNIER et al., 1997; ZENG; YANG, 2010; ZENG; YANG, 2013).

At this point, we make a didactic effort to illustrate how the constraint function knows which is the edge we intended to preserve and which is the noise we want to smooth. Generally, we assume that the noise consists of small jumps, while edges corresponds to large jumps (ZENG, 2010). We can address this problem by comparing functions s^2 and $|s|$, as shown in Figure 9, where $\mathcal{C}(r)$ is the cost function of a generic penalty function, $F(\boldsymbol{S}) = \sum_{i,j} w_{i,j}\mathcal{C}(s_i - s_j)$, with $\boldsymbol{S}$ been the all image and s been any pixel of it. When the difference $r = s_i - s_j$ is such that $r \in (-r_k, +r_k)$, we have $|s| > s^2$ and, thus $|s|$ promotes heavier penalization than s^2. Indeed, for this case the cost function for $|s|$, is greather than the cost function for the s^2, that is, $\mathcal{C}_{|s|}(r) > \mathcal{C}_{s^2}(r)$, as it can be observed in Figure 9. On the other hand, for $r > |r_k|$, we have $\mathcal{C}_{|s|}(r) < \mathcal{C}_{s^2}(r)$, meaning that s^2 promotes heavier penalization than $|s|$.

Finally, returning to Equation (1.17), making $\mathbf{w} = \beta\mathbf{w}_0$, with β constant and $\mathbf{w}_0 = [1, 1, ..., 1]$ (a large enough vector of ones), and making p decreasing from $p = 2$ to $p = 1$, we have the effect of gradually increasing the penalization of coefficients with low projections (small coefficients) on the basis $(\varphi_\gamma)_{\gamma\in\Gamma}$ (meaning that $|\langle \boldsymbol{\mu}, \varphi_\gamma \rangle| < 1$), while simultaniously decreasing the penalization of coefficients with higher projections on $(\varphi_\gamma)_{\gamma\in\Gamma}$ (meaning $|\langle \boldsymbol{\mu}, \varphi_\gamma \rangle| > 1$). Then, following this line of thought, as we move from the l_2 to l_1 norm we are penalizing less and less the $\boldsymbol{\mu}$ functions with large projections but with few components with respect to basis $(\varphi_\gamma)_{\gamma\in\Gamma}$, and, at the same time, increasing the penalization on smaller (but more frequent) $\boldsymbol{\mu}$ components, in comparison with the classical l_2 norm regularization presented in Equation (1.18). This effect becomes more

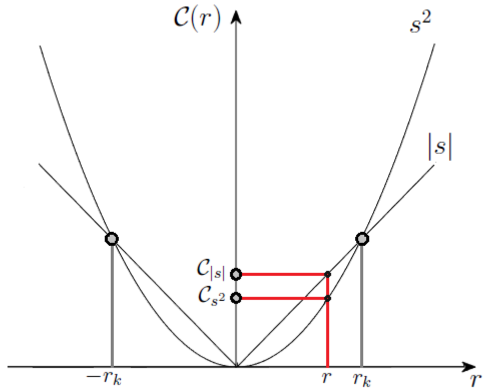

Figure 9 – Explanation of how the constraint function acts to eliminate noise while preserving edges.

evident for lower values of p, and, as a consequence, taking $p < 2$, and especially for p =1, the minimization procedure indeed promotes sparsity on the expansion of $\boldsymbol{\mu}$ with respect to the basis $(\varphi_\gamma)_{\gamma\in\Gamma}$. With these concepts in mind we write a generic objective function of l_p norm as

$$\Phi_{\mathbf{w},\mathrm{p}}(\boldsymbol{\mu}) = F(\boldsymbol{\mu}) + \beta\,||\triangledown\boldsymbol{\mu}||_p\,, \tag{1.20}$$

where β is a constant to balance between fidelity and restriction terms, and $1 \leq p \leq 2$ with $p \in \mathbb{R}$.

As will be suitably detailed in Section 1.8, this Thesis explores iterative CT image reconstruction in a Bayesian framework with regularization term on l_p norm, $1 \leq p \leq 2$. In the next section, the reader is introduced to the most relevant classical and iterative CT image reconstruction approaches.

1.5 Classical and iterative CT image reconstrucion approaches

The first approach to become popular, especially for its performance, was the Filtered Backprojection (FBP) reconstruction technique (SHEPP; LOGAN, 1973; HORN, 1979). FBP is a classic method based on the Fourier central slice theorem and is implemented with the Fast Fourier Transform (FFT). Although exhibiting good performance, FBP requires high-dose radiation, in comparison to modern methods, and, for this reason, is not consistent with the ALARA principle (YEUNG, 2019). FBP works with a simplified CT system model, as described in Section 1.2, that results in a more manageable mathematical model. As a consequence, equations in analytical closed-form can be derived, enabling an efficient reconstruction of CT images. However, the simplification of the CT system model comes at a price. It becomes quite challenging to incorporate new CT system geometries, such as cone-beam and multislice, in FBP implementation, and, threfore, it is difficulty to adapt FBP to new CT scanner architectures (HSIEH, 2009c).

An alternative to the lack of flexibility of the classical approach is to consider the reconstruction problem as a linear system, $\mathbf{y} = \mathbf{A}\mathbf{x} + \boldsymbol{e}$, where $\mathbf{A}$ describes the process of obtaining the image, $\mathbf{y}$ describes the projections captured by CT scanner sensors, $\mathbf{x}$ is the image to be reconstructed, and $\boldsymbol{e}$ is the error in the process. Therefore, for iterative reconstruction, it is natural that numerical linear algebra methods have been proposed. Along this line, the Algebraic Reconstruction Technique (ART) was proposed as an alternative to FBP (GORDON et al., 1970). Among the main advantages of ART are the easiness for introducing prior knowledge regarding CT scanner geometry, the possibility of processing truncated projections, and better performance in CT scans with limited angles (HSIEH, 2009c). However, the use of ART implies that the computational cost increases dramatically with the number of projections. To handle this, the Simultaneous Algebraic Reconstruction Technique (SART) was proposed by Andersen and Kak (1984). The main advantage over the ART method is that SART generates a complete reconstruction of the image at each iteration. Variations of the SART have been proposed in combination with other methods. OS-SART (Ordered-subset SART) presented gains over the original method by decomposing and processing data in chunks called “ordered subsets” (GE; MING, 2004); VW-OS-SART (Variable Weighted OS-SART) also showed greater potential compared to SART or OS-SART by assigning weights to the OS-SART subsets (PAN et al., 2006); sparsity properties combined with SART were used to reconstruct images with limited number of projections (YU; WANG, 2010a); the SART method was adapted to a half-threshold filtering algorithm by (YU; WANG, 2014) with great potential to improve the quality of the image reconstructed from a small number of projections in the presence of noise; the Least Square QR (from QR factorization) method was adapted with soft threshold filtering technique for few-view image reconstruction, resulting in the LSQR-STF algorithm, implemented using SART (FLORES et al., 2015); and a few-view CT reconstruction method based on SART and group-sparsity regularization, named as GSR-SART, was proposed using the concept of a group as the basic unit of sparse representation, instead of a patch, so that the image domain prior regularization term aims to eliminate the over-smoothing effect caused by the classical TV based methods (BAO et al., 2018). These are the most relevant contributions to the SART method.

For real systems, however, matrix $\mathbf{A}$ can be determined based on many system parameters, such as detector response, focal spot shape, scattering of X-ray beams, and other physical and/or geometrical parameters (HSIEH, 2009c). The measurement of each of these parameters is subject to the uncertainty principle (HEISENBERG, 1927), making the deterministic model generate noisy reconstructions. To deal with the uncertainty inherent in the CT image reconstruction process, statistical methods have been developed. Next, the reader is presented to CT image reconstruction statistical approaches.

1.6 Statistical CT image reconstruction approaches

The classical approaches, while successful, do not favour the incorporation of physical-statistical phenomena in the CT framework. For example, photon emission is a rare event and may be well described by the Poisson distribution, as mentioned in Section 1.3; beam behaviour is best described by a response function that models the shadows cast onto detectors using a Gaussian model (HSIEH, 2009c); the beam hardening phenomenon (lines and shadows adjacent to high-density reconstructed areas) that appears due to the polyenergetic nature of X-ray emissions can be statistically corrected (LANGE et al., 1987); the loss of photons by sensors, known as photon read-out, is a Gaussian phenomenon (SNYDER et al., 1995); data acquisition electronic noise and energy-dependent signals can be modeled as compound Poisson plus Gaussian noise (WHITING, 2002).

In this context, a statistical approach means adding to the mathematical model elements that describe physical-statistical phenomena present in the CT image reconstruction process. As a consequence, the incorporation of detailed statistical models into CT reconstruction is not straightforward. In this sense, many solutions for the CT image reconstruction problem use some form of statistical approach (CARSON; LANGE, 1984; MAN et al., 2000; MAN et al., 2001; ELBAKRI; FESSLER, 2002; YU; WANG, 2009; YU; WANG, 2010b; XU et al., 2011; DEáK et al., 2013; YU; WANG, 2014; CHOUDHARY et al., 2014; FLORES et al., 2015; BAO et al., 2018; ZHU; PANG, 2018). Adaptive statistical iterative reconstruction techniques have shown significant results compared to non-adaptive techniques (DEáK et al., 2013; CHOUDHARY et al., 2014; KIM et al., 2016; Zhang et al., 2018). In general, although the models incorporate part of the statistical phenomena, most of these phenomena are not modeled since the practical effects are relatively insignificant and result in high-cost computational solutions.

An important method is proposed by Clark et al. (2015), which consists of using rank-sparse kernel regression filtering with Bilateral Total Variation (BTV) to map the reconstructed image into spectral and temporal contrast images. In this work, the authors strictly constrain the regularization problem while separating temporal and spectral dimensions, resulting in a highly compressed representation and enabling substantial undersampling of acquired signals. The method (5D CT data acquisition and reconstruction protocol) efficiently exploits the rank-sparse nature of spectral and temporal CT data to provide high-fidelity reconstruction results without increased radiation dose or sampling time. However, a remark should be made regarding the use of BTV (regularization based on l_1 norm). This often leads to the piecewise constant result and hence tends to produce artificial edges on the smooth areas. In order to mitigate this counterpoint of l_1 norm regularization, Charbonnier et al. (1997) developed an edge-preserving regularization scheme known as Bilateral Edge Preservation (BEP), which allows the used of a l_p norm, $1 < p < 2$, and is applied in this work.

Sreehari et al. (2016) proposed a plug-and-play (P&P) priors framework with a Maximum a Posteriori (MAP) estimate approach used to design an algorithm for electron tomographic reconstruction and sparse image interpolation that exploits the non-local redundancy in images. The power of the P&P approach is that it allows a wide array of modern denoising algorithms to be used as a prior model for tomography and image interpolation. Perelli et al. (2016) propose the denoising CT generalized approximate message passing algorithm (DCT-GAMP), an adaptation of approximate message passing (AMP) technique that represents the state of the art for solving undersampling compressed sensing problems with random linear measurements. In contrast, this approach uses minimum mean square error (MMSE) instead of MAP, and the authors show that using MMSE favors decoupling between the noise conditioning effects and the system models.

The statistical approach, most notably based on the Bayesian framework, is widely applied to the reconstruction of X-ray tomography, with some variations, (YU; WANG, 2009; YU; WANG, 2010b; XU et al., 2011; CAMPONEZ et al., 2012; ZENG; YANG, 2013; CHOUDHARY et al., 2014; ZHU; PANG, 2018; SUN et al., 2019; GU et al., 2019), and make possible the insertion of prior knowledge into the CT system model. This approach promises two advantages.

First, it provides the search with more satisfactory solutions (noiseless ones) through the limitation of the searchable set of solutions using an a priori function (known as restriction). In the context of computed tomography, this means that large differences in intensity between neighbor pixels tend to be interpreted as an outlier, and therefore, such a solution should be disregarded (HSIEH, 2009c). For example, it is strongly unlikely that a small part of a human tissue, represented in the image by a single pixel, has a characteristic of intensity totally different from its surroundings. In this sense, such a pixel should be discarded and replaced with some version more compatible with its neighborhood. Moreover, solving the CT reconstruction system, $\mathbf{y} = \mathbf{A}\mathbf{x} + \boldsymbol{e}$, is an inverse and ill-posed problem, and prior knowledge often ensures the stability of the solution.

Second, we can adopt a simplified mathematical model for tomographic image reconstruction and compensate its inefficiency (instability and noisy reconstruction) by adding the statistical component (prior knowledge) to the objective function. However, the model simplification has its limitations and should be used accordingly (HSIEH, 2009c). As a consequence of prior knowledge introduction, more satisfactory solutions – low noise level – can be found. Maximum a Posteriori (MAP) is a useful statistical framework for CT reconstruction and favors the incorporation of the regularization term with prior knowledge into the model.

The MAP strategy, as developed in Section 1.3, provides an objective function composed by the sum of the probability (also known as fidelity) and the regularization function that establishes the optimization restriction criteria, also known as a prior (or priori function). In the next section, we present a signal model and discuss the error issues.

1.7 Signal modeling and error considerations in CT image reconstruction

As previously discussed, the statistical approaches can reduce deficiencies caused by classical mathematical modeling without having to literally incorporate the complexity of a real-world model. However, before proposing a statistical (non-deterministic) model that results in a lower noise reconstruction, it is necessary to establish the process as a whole. As shown in Figure 10, the process begins with a synthetic image, $\boldsymbol{\mu}$. In this work we use

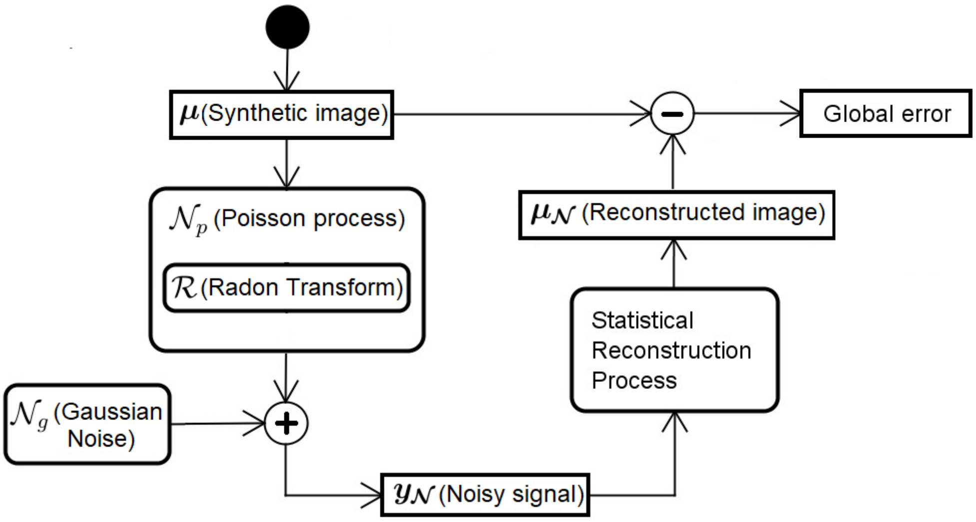

Figure 10 – From acquisition to reconstruction and measurement of error.

different synthetic images as pointed in Section 1.9. The synthetic image is submitted to the Radon transform, $\mathcal{R}(.)$, generating the ideal (free of noise) signal of the CT scan.

Despite the ideal scenario illustrated above, X-rays are generated in CT scanners by accelerating electrons through an electrical potential field into a target. This process produces quanta (energy packages) with a range of energies up to the maximum tube potential in kVp (Kilovoltage peak)[3]. The generated quanta passes through the scanned object, interacting with the material. In the interaction process, they can either be removed from the beam (absorption), or they can arrive at the detector (detection). Arriving at the detector, the quanta packages have a probability of being measured by the scanner sensor. Indeed, there is a remote probability that the quanta package will not be read by the detector, and this is known as photon read-out, as mentioned in Section 1.6. Each of these processes is an independent event and, as a consquence, the statistics of the interaction of

[3] Kilovoltage peak (kVp) is the peak voltage applied to the X-ray tube. It defines the maximum energy of X-ray photon being responsible for the acceleration of electrons from the cathode to the anode of a vacuum tube.

quanta with the CT scanner are governed by Poisson statistics. Then, the mean number of detected quanta at any energy level can be defined as $\lambda(E) = N(E)\,T(E)\,A(E)$, where E is the energy level, $N(E)$ is the number of created quanta at a particular energy level, $T(E)$ is the survival probability of these quanta through the scanned object, and $A(E)$ is the probability of measurement in the detector. The probability of measuring a finite number of quanta Q for a process with a mean, λ, is defined by the Poisson distribution, $P(Q,\lambda) = \frac{\lambda^Q}{Q!}e^{-\lambda}$ (WHITING, 2002). Once photon detection problem in CT exams is a particle countable process, well described by Poisson statistics, it is used in the model in Figure 10, represented by the $\mathcal{N}_p$ random variable.

However, if we assume a high number of photons is detected at each sensor of the CT equipment, the acquisition process can be modeled as Gaussian due to the central limit theorem. In addition, the Gaussian model leads to additive algorithms, whereas the Poisson model leads to multiplicative, and therefore less efficient, algorithms – as argumented by Charbonnier et al. (1997). In this work, we assume that the signal arriving at the CT equipment detectors is influenced by Gaussian additive noise and, from the dosage reduction methods presented in Section 1.1, we chose to emulate the low radiation dosage by reducing the number of projection angles processed. This means we assume that each detector absorbs an amount of photons that allows modeling the noise as a Gaussian additive one and the low dosage occurs by reducing the number of projections captured by the detectors (by reducing scanning angles). Accordingly, even with the process having a Poissonian nature, Gaussian additive noise can be added to the process, as

$$\boldsymbol{y}_{\mathcal{N}} = \mathcal{R}(\boldsymbol{\mu}) + \mathcal{N}_g, \tag{1.21}$$

where $\boldsymbol{y}_{\mathcal{N}}$ is the resulting signal that approximates a tomography signal, $\mathcal{R}(\boldsymbol{\mu})$ is the result of applying the Radon transform on the synthetic image, $\boldsymbol{\mu}$, and $\mathcal{N}_g$ is the Gaussian additive noise.

The remainder of this work is dedicated to the reconstruction of the CT image, $\boldsymbol{\mu}_{\mathcal{N}}$, from the signal, $\boldsymbol{y}_{\mathcal{N}}$, and the reduction of the global error, i.e., the reduction of the difference between synthetic and reconstructed images. As a criterion for measuring the quality of image reconstruction, we use Peak Signal-to-noise Ration (PSNR) and Structural Similarity, known as SSIM (WANG et al., 2004). Next we formally present the proposal of this Thesis.

1.8 The contribution of the Thesis

The present work is based on the Bayesian iterative CT image reconstruction model presented in Sections 1.2 and 1.3. In addition, as presented in Section 1.4, Ingrid Daubechies and colleagues (2004) proposed a generalist discussion of constraint functions with norm l_p, $1 \leq p \leq 2$, where sparsity of data can be promoted with respect to an ortogonal basis on Hilbert space ($\mathcal{H}$), and (sparsity can rather be) intensified as we move the l_p norm of constrainging function from $p = 2$ to $p = 1$.

As discussed in Section 1.1, the radiation dose applied to the patient in CT scans is of great concern to the medical community. Thus, as argumented in the same section and supported by the literature reviewed in Sections 1.5 and 1.6, the reconstruction of CT images with low-dose radiation (meaning a small number of scanning angles) is a state of the art problem (BAO et al., 2018; ZHU; PANG, 2018; GU et al., 2019; SUN et al., 2019; SMITH-BINDMAN et al., 2019; YEUNG, 2019). Section 1.6 presents a variety of iterative solutions to the problem of X-ray CT image reconstruction, including some for low-dose. Among the most successful one has the solutions that explore the sparsity of the constraint function in l_1 norm. Nevertheless, although these solutions are effective, they usually converge quite slowly (DAUBECHIES et al., 2004; YU; WANG, 2010a; YU; WANG, 2014).

1.8.1 Our Hypothesis

As a hypothesis, we argue in this work that it is possible to propose a method to reconstruct tomographic images that obtaining good results for both regular and low dosage tomographies, able to reduce noise, preserve borders and generate few artifacts in the reconstructed images.

1.8.2 Objectives of the work

Generally speaking, our proposal is to apply a l_p norm, $1 \leq p \leq 2$, constraining function to accelerate the convergence of the proposed algorithms considering Peak Signal-to-noise Ration (PSNR) metric. We also make some measurements using the Structural Similarity (SSIM) metric. More specifically,

- we have developed a three-stage objective function to address the CT image reconstruction problem, our main contribution. The first stage is characterized by a standard fidelity l_2 norm function, whereas the second one is a noise reduction stage defined by a l_p norm function, $1 \leq p \leq 2$. As for the third one, it is characterized by a l_1 norm function constraint. The three-stage objective function is alternately minimized by a three-step algorithm given by (i) the minimization of the fidelity function using the Simultaneous Algebraic Reconstruction Technique (SART) algorithm, (ii) gradient descent minimization of a Biletaral Edge Preservation (BEP) function for noise reduction, and (iii) total variation minimization of a Discret Gradient Transform (DGT) function by soft-threshold non-linear filtering. We experimentally show a gain in terms of PSNR and SSIM metrics in the first steps of the iterative reconstruction, in comparison with the well-established two-stage approach using

l_2 norm for fidelity with l_1 norm for restriction, for both normal and low dosage (emulated by a limited number of projections).

- we show experimentally that by varying the l_p norm of the noise reduction function (step 2 of the proposed objetive function) appropriately, it is possible to keep the solution stable in terms of the PSNR and SSIM metrics, which is our second contribution. In other words, the difference between the PSNR values of subsequent reconstructions in the iterative process tends to decrease in a global perspective. The same behavior is observed for SSIM values.

In summary, we propose a three-stage method that alternates (i) minimization of a l_2 norm fidelity function by Simultaneous Algebraic Reconstruction Technique (SART), (ii) adaptive regularization of the fidelity function by a l_p norm using Bilateral Edge Preservation (BEP), and (iii) regularization of the resulting function with the sparse operator Discrete Gradient Transform (DGT) term by Total Variation (TV). The resulting image is continuously used to feed back the step (i) of the algorithm until reaching a stopping criterion.

1.9 Materials and methods

The objective of this section is to describe materials and methods used in the work. In the image reconstruction process we start from a signal originated from a synthetic image, known as phantom, as explained in Section 1.7. We used four image phantoms, namelly:

- Shepp-logan head phantom, from Matlab® documentation (MathWorks®, 1994) and (SHEPP; LOGAN, 1973);
- FORBILD head phantom, as defined by Lauritsch and Bruder (2016) and Yu et al. (2012);
- FORBILD abdomen phantom, defined by Schaller (2016);
- Checkerboard image, from Matlab® documentation (MathWorks®, 1998).

The first three images are known as digital phantoms and are widely used in medical imaging reconstruction literature. The last image is used as counterpoint and helps in the analysis of characteristics of the methods here studied.

We used the software Matlab® as development and simulation platform, mainly the Image Processing and Digital Signal Processing (DSP) toolboxes. The AIR Tool Matlab® package (HANSEN; SAXILD-HANSEN, 2012) was used to generate the system matrix $\mathbf{A}$

form the input synthetic image, the phantom. In the sequel we list the main scripts used in this, with the correspondent scripts descriptions. They are:

- `signalModel.m`, to introduce gaussian noise to the generated signal, produced by the author;
- `parallelTomo.m`, to generate the system matrix from the input synthetic image, from AIR Tool Matlab® package;
- `imageGenerator.m`, to generate the image matrix, produced by the author;
- `mainProcess.m`, script used to perform the reconstruction processes with all the methods studied in this work, produced by the author;
- `mainLoop.m`, to repeat the main processing a certain number of times, produced by the author;
- `psnr.m`, implementating the PSNR metric, produced by the author;
- `coreSART.m`, implementating the SART method, produced by the author;
- `coreBEP.m`, implementating the BEP method, produced by the author;
- `coreDGT.m`, to implement the DGT method, produced by the author;
- `coreSTNF.m`, core implementation of soft-threshold non-linear filtering, produced by the author;
- `coreFBP.m`, implementation of the Filtered Backprojection reconstruction technique, produced by the author, and
- `utils.m`, auxiliary functions to produce graphs, table data, and analyze processed data, produced by the author.

To evaluate results of reconstruction methods in this work we use Peak Signal-to-noise Ration (PSNR) and Structural Simiralirity Method (SSIM). As there is noise injection in the input signal, according to Section 1.7, some procedures are executed many times – generally 101 times (HINES et al., 2003) – and the mean values of each step (PSNR and SSIM) is calculated, presented and discussed in the graphs of Chapter 4. We reinforce that average values of the pixels are not calculated. Instead, we calculate the average values of the PSNR and SSIM indices in each iteration of the reconstruction process.

2 Modeling the objective function

First in this chapter we present the Bayesian MAP framework, whose theoretical basis was presented in Section 1.3, and which is widely used in medical image reconstruction problems, including X-ray CT, as well as superresolution problems (YU; WANG, 2009; YU; WANG, 2010b; XU et al., 2011; CAMPONEZ et al., 2012; CHOUDHARY et al., 2014; ZHU; PANG, 2018; SUN et al., 2019; GU et al., 2019). This framework, as dicussed in Section 1.3, generally consists of a fidelity function (discrepancy) minimazed by a l_2 norm operator an a constranining function (restriction) minimized by a l_1 norm sparse operator. Some solutions present a l_2 norm restriction (not sparse). The implications of each type of restriction (related to the norm) was discussed in Section 1.4. After presenting the classic MAP solution with l_1 norm restriction, we present our approach consisting of a three-step solution with the novelty of introducing an adaptive noise reduction stage between the minimization of the fidelity function and the restriction function of the classical model. We also present a new two-steps solution consisting of minimizing a l_2 norm fidelity function concatenated with an adaptive l_p norm restriction function, with $1 \leq p \leq 2$.

2.1 CT image reconstruction objective function modeling with l_2 norm functional for fidelity and l_1 norm for restriction

This method consists of minimizing an objective function with a l_2 norm fidelity function and a prior function, as presented in Equation (1.16). The regularization is performed by minimizing the total variation (TV), a l_1 norm operator. TV is the sum of the absolute coefficients of the discrete gradient transform (DGT) of the reconstructed image. The DGT function is defined as

$$D_j\boldsymbol{\mu} = D_{m,n}\boldsymbol{\mu} = \sqrt{(\mu_{m,n} - \mu_{m+1,n})^2 + (\mu_{m,n} - \mu_{m,n+1})^2}, \tag{2.1}$$

where $j = (m-1) \times W + n$, $m = 1, 2, ..., H$, $n = 1, 2, ..., W$, with W and H being, respectively, the width and height of the matrix representing the image, $\boldsymbol{\mu}$, with $N_J = W \times H$ pixels.

Rewriting Equation (1.16), assuming the regularizaton term as based on DGT function, we have the objective function as follows

$$\Phi(\boldsymbol{\mu}) = \sum_{i=1}^{N_I} \frac{y_i}{2} \left([\mathbf{A}\boldsymbol{\mu}]_i - \hat{p}_i\right)^2 + \beta R_{DGT}(\boldsymbol{\mu}), \tag{2.2}$$

where $\sum_{i=1}^{N_I} \frac{y_i}{2} \left([\mathbf{A}\boldsymbol{\mu}]_i - \hat{p}_i\right)^2$ is the fidelity term, with $\hat{p}_i$ being an estimate of p_i, β being a positive adjustment parameter to balance the terms of fidelity and TV (usually set to 1), and $R_{DGT}(\boldsymbol{\mu})$ is defined as

$$R_{DGT}(\boldsymbol{\mu}) = TV(\boldsymbol{\mu}) = \|D\boldsymbol{\mu}\|_1, \tag{2.3}$$

with $D\boldsymbol{\mu} = (D_1\boldsymbol{\mu}, ..., D_{NJ}\boldsymbol{\mu})^T$.

In order to make our notation more readable, let $\mathcal{C}(\mu_i) = \frac{y_i}{2}\left([\mathbf{A}\boldsymbol{\mu}]_i - \hat{p}_i\right)^2$ be the cost function in Equation (2.2). Then we can write $\mathcal{C}(\mu_i) = \left(\sqrt{\frac{y_i}{2}}\left([\mathbf{A}\boldsymbol{\mu}]_i - \hat{p}_i\right)\right)^2$, and, in order to incorporate $\sqrt{\frac{y_i}{2}}$ into $\mathbf{A}$ and $\hat{\boldsymbol{p}}$, we define the operator $\Lambda = \text{diag}(\sqrt{\frac{y_i}{2}}) \in \mathbb{R}^{N_I} \times \mathbb{R}^{N_I}$ as a diagonal matrix with all the (diagonal) elements described as $a_{\Lambda_i} = \sqrt{\frac{y_i}{2}}$. Therefore, we can apply the transformation

$$\Lambda\mathbf{A} = \mathbf{A}_\Lambda = \{a_{\Lambda_i}\}, \Lambda\hat{\boldsymbol{p}} = \hat{\boldsymbol{p}}_\Lambda, \hat{\boldsymbol{p}} = (\hat{p}_1, \hat{p}_2, ..., \hat{p}_{NI}), \tag{2.4}$$

and, introducing the auxiliary variable $\boldsymbol{\nu} = D\boldsymbol{\mu}$, the objective function in Equation (2.2) can be written in compact form as

$$\Phi(\boldsymbol{\mu}) = F(\boldsymbol{\mu}) + \beta\|\boldsymbol{\nu}\|_1 = \|\mathbf{A}_\Lambda\boldsymbol{\mu} - \hat{\boldsymbol{p}}_\Lambda\|_2^2 + \beta\|\boldsymbol{\nu}\|_1. \tag{2.5}$$

The ultimate goal is to minimize the objective function $\Phi(\boldsymbol{\mu})$, obtaining $\hat{\boldsymbol{\mu}}$ as

$$\hat{\boldsymbol{\mu}} = \underset{\mu}{argmin}\{F(\boldsymbol{\mu}) - \beta R(\boldsymbol{\mu})\}, \tag{2.6}$$

where the fidelity term, $F(\boldsymbol{\mu})$, represented both in the expanded version of Equation (1.16), and in the compact version of Equation (2.5), is

$$F(\boldsymbol{\mu}) = \sum_{i=1}^{N_I} \frac{y_i}{2}\left([\mathbf{A}\boldsymbol{\mu}]_i - \hat{p}_i\right)^2 = \|\mathbf{A}_\Lambda\boldsymbol{\mu} - \hat{\boldsymbol{p}}_\Lambda\|_2^2, \tag{2.7}$$

and $R(\boldsymbol{\mu})$ is the restriction that drives the solution according to certain criteria (l_1 norm in the case of DGT function). The optimization of $F(\boldsymbol{\mu})$, although simple, is an important concept and can be defined as

$$\tilde{\boldsymbol{\mu}} = \underset{\mu}{argmin}\{F(\boldsymbol{\mu})\}, \tag{2.8}$$

with $\tilde{\boldsymbol{\mu}}$ been the estimate of original image, $\boldsymbol{\mu}$. The optimization problem described by Equation (2.8) can be solved by the Simultaneous Algebraic Reconstruction Technique (SART) (ANDERSEN; KAK, 1984), and consists of replacing the cost function of Equation (2.5) by a surogate function that makes the cost function separable, so that all pixels can be updated simultaneously (ELBAKRI; FESSLER, 2002; XU et al., 2011).

Optimization of Equation (2.6) can be solved by performing alternating minimization between (i) optimization of the fidelity term by SART, and (ii) minimizing the total variaton of regularization term, $R(\boldsymbol{\mu})$, by performing a pseudo-inverse of the DGT with soft-threshold filtering algorithm whose convergence and efficiency have been theoretically proven in (DAUBECHIES et al., 2004). In the next section we develop de model for our first contribution.

2.2 Three-stage objective function modeling for CT image reconstruction with adaptive l_p norm for noise reduction

As discussed in Section 1.4, the regularization based on the l_1 norm often introduces artificial edges in smooth transition areas. Moreover, a good regularization strategy should simultaneously perform noise suppression and edge preservation. With this motivation, Charbonnier et al. (1997) proposed the bilateral edge preserving (BEP) regularization function. In addition, Daubechies et al. (2004) proposed regularization by nonquadratic constraint functions that promote sparsity with a l_p norm, $1 \leq p \leq 2$. Inspired by the bilateral total variation (BTV) regularization (FARSIU et al., 2004), a l_1 norm technique, we propose a BEP scheme adapted for CT reconstruction, which uses a l_p norm, $1 \leq p \leq 2$. BTV regularization is defined by

$$R_{BTV}(\mathbf{X}) = \underbrace{\sum_{l=-q}^{q} \sum_{m=0}^{q}}_{l+m \geq 0} \alpha^{|l|+|m|} \| \mathbf{X} - S_x^l S_y^m \mathbf{X} \|_1, \tag{2.9}$$

where q is a positive number, S_x^l and S_y^m are displacements by l and m pixels in the horizontal and vertical directions, respectively, $\mathbf{X}$ is the image in reconstruction/regularization, and α, $0 < \alpha < 1$, is applied to create a spatial decay effect for the sum of terms in BTV regularization. The BEP regulation uses the same principle of BTV but with an adaptive norm (instead of the l_1 norm) defined by

$$\rho(s, a) = \rho_a(s) = a\sqrt{a^2 + s^2} - a^2, \tag{2.10}$$

where a is a positive value and s is the difference that one wants to minimize. This function was initially proposed by Charbonnier et al. (1997) to preserve edges in the image regularization process. The parameter a is used to specify the error value for which the regularization becomes linear (growing with the error) to constant (saturated, regardless of the error). The same adaptive norm definition is also used in super-resolution problems (ZENG; YANG, 2013). The $\rho(s, a)$ function is a M-estimator, since it corresponds to the LM (maximum likelihood) type estimation (RABIE, 2005), and has its influence function given by

$$\psi(s, a) = \psi_a(s) = \frac{\partial \rho(s, a)}{\partial s} = \frac{as}{\sqrt{a^2 + s^2}}. \tag{2.11}$$

The influence function indicates how much a particular measure contributes to the solution (ZENG; YANG, 2013). We illustrate in the graphs of Figure 11a the behavior of $\rho(s, a)$ (the error norm function), and in Figure 11b, its influence function. It can be observed that as parameter a evolves from 0 to 1, the function changes its behavior from l_1 to l_2 norm. Thus, as mentioned in (ZENG; YANG, 2010; ZENG; YANG, 2013), Equation (2.10) behaves adaptively with respect to the norm that it implements.

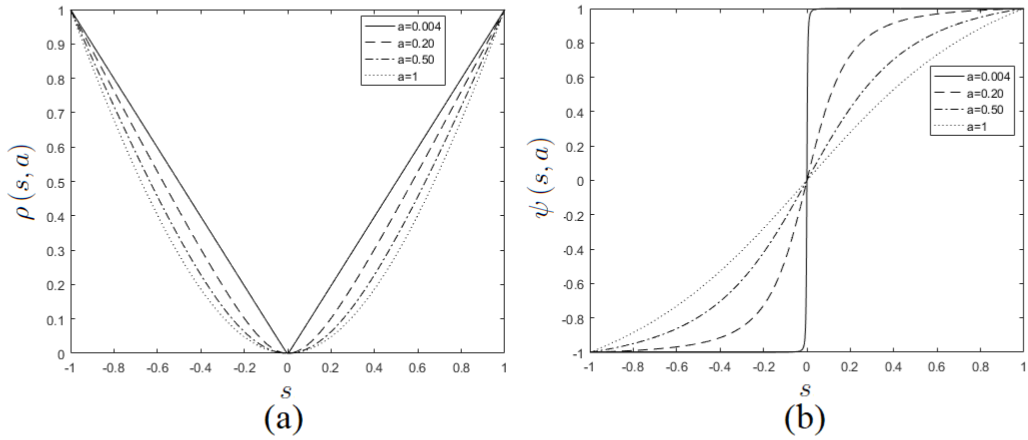

Figure 11 – (**a**) Error norm function, Equation (2.10), and (**b**) influence function, Equation (2.11).

Therefore, combining Equations (2.9) and (2.10), for the particular case of CT image reconstruction, we propose an adaptive operator defined as

$$R_{BEP}(\tilde{\boldsymbol{\mu}}) = \underbrace{\sum_{l=-q}^{q} \sum_{m=0}^{q}}_{l+m\geq 0} \sum_{j=1}^{N_j} \alpha^{|l|+|m|} \rho_a \left(\left(\tilde{\boldsymbol{\mu}} - S_x^l S_y^m \tilde{\boldsymbol{\mu}} \right) [j] \right). \tag{2.12}$$

It is important to note that s in Equation (2.10) is the same as $\left(\tilde{\boldsymbol{\mu}} - S_x^l S_y^m \tilde{\boldsymbol{\mu}}\right)[j]$ in Equation (2.12), that is, $s = \left(\tilde{\boldsymbol{\mu}} - S_x^l S_y^m \tilde{\boldsymbol{\mu}}\right)[j]$, and j is the index of the pixel $\tilde{\mu}_j$ of image $\tilde{\boldsymbol{\mu}}$, with $j = 1, ..., N_j$. The values q, α, S_x^l and S_y^m are the same as in Equation (2.9); and $\tilde{\boldsymbol{\mu}}$, defined in Equation (2.8), is the estimated image obtained in the i-th iteraction by l_2 minimization of the objective function in Equation (2.7). It is noteworthy that the term $R_{BEP}(\tilde{\boldsymbol{\mu}})$ imposes an l_p regularization norm, $1 \leq p \leq 2$, on the image $\tilde{\boldsymbol{\mu}}$. Thus, we can rewrite the objective function of Equation (2.5), $\Phi(\boldsymbol{\mu})$, so that a new regularization term, $R_{BEP}(\tilde{\boldsymbol{\mu}})$, is introduced between the l_2 norm minimization and TV minimization. As a consequence, the objective function proposed in this work incorporates adaptive regularization to the objective function, and defining an auxiliary variable $\boldsymbol{\sigma} = R_{BEP}(\tilde{\boldsymbol{\mu}})$, we have

$$\Phi(\boldsymbol{\mu}) = \|\mathbf{A}_\Lambda \boldsymbol{\mu} - \hat{\boldsymbol{p}}_\Lambda\|_2^2 + \gamma \|\boldsymbol{\sigma}\|_p + \beta \|\boldsymbol{\nu}\|_1, \tag{2.13}$$

where γ is a positive adjustment parameter to balance the terms of fidelity and adaptive regularization, and $\mathbf{A}_\Lambda$ and $\hat{\boldsymbol{p}}_\Lambda$ are defined in Equation (2.4). The other parameters are the same as in Equation (2.5), and p, $1 \leq p \leq 2$, is the norm BEP method imposed on the regularization process.

2.3 Two-stage CT image reconstruction objective function modeling with l_2 norm functional for fidelity and l_p norm for restriction

In this section we present a new two-stage objective function with l_2 norm for fidelity and l_p norm for restriction, with $1 \leq p \leq 2$. The arguments for proposing such a solution are formally explained in Sections 1.4 and 2.2. However, we reinforce that l_2 norm constraining functions tends to be austere with large differences between pixels, which are generally interpreted as edges; and to smooth out small differences, which can be interpreted as noise. In contrast, l_1 norm constraining functions tends to create artifacts in regions with low variation between pixels and preserve differences in regions with relatively large gaps.

The proposal is to minimize an objective function with a l_2 norm fidelity function and a l_p norm prior function, as presented in Equation (1.20). We borrowed the concept of total variation of the DGT to propose the regularization by minimizing the total variation of the l_p norm using the adaptive norm presented in Equation (2.10). In this case, TV is the sum of the absolute coefficients of the bilateral edge preservation (BEP) function of the reconstructed image. The BEP fucntion is defined as

$$Da_j\boldsymbol{\mu} = Da_{m,n}\boldsymbol{\mu} = a\sqrt{a^2 + \left(\mu_{m,n} - \mu_{m+1,n}\right)^2 + \left(\mu_{m,n} - \mu_{m,n+1}\right)^2} - a^2, \tag{2.14}$$

where j, m and n are already defined in Equation (2.1), and a is the parameter that makes the BEP function walks from l_1 to l_2 norm, as a goes from $a = 0^+$ (meaning that a it is infinitesimally greater than 0) to $a = 1$, with $a \in \mathbb{R}$. This behavior is well illustrated in Figure 11.

In analogy with Equation (2.3), we define the adaptive total variation $Ra\left(\boldsymbol{\mu}\right)$ as

$$Ra\left(\boldsymbol{\mu}\right) = TVa\left(\boldsymbol{\mu}\right) = \|Da\boldsymbol{\mu}\|_{p=a+1}, \tag{2.15}$$

with $Da\boldsymbol{\mu} = \left(Da_1\boldsymbol{\mu}, ..., Da_{NJ}\boldsymbol{\mu}\right)^T$ and $p = a + 1$ is the norm of $\|Da\boldsymbol{\mu}\|$, $a \in (0, 1]$, and $a \in \mathbb{R}$. Therefore, introducing the auxiliary variable $\boldsymbol{\vartheta}_a = Da\boldsymbol{\mu}$, the objective function in Equation (1.20) can be written in compact form as

$$\Phi_a\left(\boldsymbol{\mu}\right) = F\left(\boldsymbol{\mu}\right) + \beta\|\boldsymbol{\vartheta}_a\|_{a+1} = \|\mathbf{A}_\Lambda\boldsymbol{\mu} - \hat{\boldsymbol{p}}_\Lambda\|_2^2 + \beta\|\boldsymbol{\vartheta}_a\|_{a+1}, \tag{2.16}$$

with $\mathbf{A}_\Lambda$ and $\hat{\boldsymbol{p}}_\Lambda$ defined in Equation (2.4). The ultimate goal is to minimize the objective function $\Phi_a\left(\boldsymbol{\mu}\right)$, obtaining $\hat{\boldsymbol{\mu}}$, as shown below

$$\hat{\boldsymbol{\mu}} = \underset{\mu}{argmin}\left\{F\left(\boldsymbol{\mu}\right) - \beta Ra\left(\boldsymbol{\mu}\right)\right\}, \tag{2.17}$$

where the fidelity term, $F\left(\boldsymbol{\mu}\right)$, is represented in Equation (2.5), and $Ra\left(\boldsymbol{\mu}\right)$ is the restriction that drives the solution according to l_p norm , $1 \leq p \leq 2$, which is the case of the BEP function.

Optimization problem of Equation (2.16) can be solved by performing alternating minimization between (i) optimization of the fidelity term by SART, and (ii) minimizing the total variaton of regularization term, $Ra\left(\boldsymbol{\mu}\right)$, by performing a pseudo-inverse of the BEP with soft-threshold filtering algorithm, whose convergence has been proved in (DAUBECHIES et al., 2004).

3 Tree-stage objective function optimization

In this chapter the algorithm that minimizes Equation (2.13) is developed. The optimization stages are minimized sequentially, that is, the output of the first stage is used as input to the second one. The output of the second stage serves as input to the third one, and the resulting image is used to re-feed the first stage. The three stages are repeated iteratively until a satisfactory result is obtained or a certain number of steps is reached. Thus, for the proposed method, three stages are necessary: (i) minimizing $F(\boldsymbol{\mu})$ with SART, (ii) applying the gradient descent (GD) method to the result of the first stage, using $R_{BEP}(\boldsymbol{\mu}) = \gamma\|\boldsymbol{\sigma}\|_p$ as a regularization term, and (iii) applying DGT regularization to the previous result, minimizing $\beta\|\boldsymbol{\nu}\|_1$ with soft-threshold filtering. For a better understanding, each one of the three stages is presented in the sequence.

3.1 First stage - minimization of the fidelity term with Simultaneous Algebraic Reconstruction Technique $(SART)$

The first step is to solve the optimization problem described by Equation (2.13). A popular solution was proposed by Ge and Ming (2004), which can be computationally expressed by the iterative equation

$$\tilde{\mu}_j^k = \tilde{\mu}_j^{k-1} + \lambda^k \tfrac{1}{a_{+j}} \sum_{i=1}^{N_I} \tfrac{a_{i,j}}{a_{+i}} \left(\hat{p}_i - A_i \boldsymbol{\mu}^{k-1}\right), \tag{3.1}$$

where $a_{+j} = \sum_{i=1}^{N_I} a_{ij} > 0$, $a_{+i} = \sum_{j=1}^{N_J} a_{ij} > 0$, A_i is the i-th line of $\mathbf{A}$, k is the iteration index, and $0 < \lambda^k < 2$ is an arbitrary relaxation parameter (HANSEN; SAXILD-HANSEN, 2012; YU; WANG, 2014). To simplify the notation, one can establish $\boldsymbol{\Lambda}^{+\boldsymbol{N_J}} \in \mathbb{R}^{N_J} \times \mathbb{R}^{N_J}$ as a diagonal matrix with $\Lambda_{jj}^{+N_J} = \frac{1}{a_{+j}}$, and $\boldsymbol{\Lambda}^{+\boldsymbol{N_I}} \in \mathbb{R}^{N_I} \times \mathbb{R}^{N_I}$ also as a diagonal matrix with $\Lambda_{ii}^{+N_I} = \frac{1}{a_{+i}}$. Then, Equation (3.1) can be rewritten as

$$\tilde{\boldsymbol{\mu}}^k = \tilde{\boldsymbol{\mu}}^{k-1} + \lambda^k \boldsymbol{\Lambda}^{+N_J} \mathbf{A}_\Lambda^T \boldsymbol{\Lambda}^{N_I+} \left(\boldsymbol{p}_\Lambda - \mathbf{A}_\Lambda \tilde{\boldsymbol{\mu}}^{k-1}\right), \tag{3.2}$$

where the term λ^k is usually constant and equal to 1. The method described in Equation (3.1) is commonly known as SART. This method produces a relatively noisy reconstruction, as can be observed in Chapter 4. Now $\tilde{\boldsymbol{\mu}}$ is the inputted to the second stage in the reconstruction process.

3.2 Second stage - bilateral edge-preserving with a gradient descent method

In the second stage, the goal is to solve the optimization problem defined by

$$\hat{\boldsymbol{\mu}} = \underset{\mu}{argmin} \left\{ \tilde{\boldsymbol{\mu}} - \gamma R_{BEP} \left(\tilde{\boldsymbol{\mu}} \right) \right\}, \tag{3.3}$$

where γ is a parameter that weights the contribution of the constraint R_{BEP} (see Equation (2.12)). The gradient descent method can be applied to solve this problem as

$$\boldsymbol{\mu}^{k} = \boldsymbol{\mu}^{k-1} - \gamma \bigtriangledown R_{BEP} \left(\boldsymbol{\mu}^{k-1} \right), \tag{3.4}$$

resulting in an optimization problem written in detail as follows

$$\hat{\boldsymbol{\mu}} = \underset{\mu}{argmin} \left\{ \sum_{j=1}^{N_j} \rho_a \left(\tilde{\boldsymbol{\mu}} \right) + \underbrace{\sum_{l=-q}^{q} \sum_{m=0}^{q}}_{l+m \geq 0} \sum_{j=1}^{N_j} \alpha^{|l|+|m|} \rho_c \left(\tilde{\boldsymbol{\mu}} - S_x^l S_y^m \tilde{\boldsymbol{\mu}} \right) [j] \right\}. \tag{3.5}$$

In Equation (3.5), $\tilde{\boldsymbol{\mu}}$ is the result of first-stage minimization, as defined in Equation (2.8), $\rho_a(s) = \rho(s, a)$ is as in Equation (2.10), but with $s = \tilde{\boldsymbol{\mu}}$, and $\rho_c(s) = \rho(s, c)$ is the same as in Equation (2.10), but with a constant c instead of a constant a and $s = \tilde{\boldsymbol{\mu}} - S_x^l S_y^m \tilde{\boldsymbol{\mu}}$ where S_x^l and S_y^m are the same as in Equation (2.9). Now we derive a computable matrix form from Equation (3.5).

With Equation (3.4) in mind and substituting Equation (2.10) into the core (within the braces) of Equation (3.5), we have

$$\bigtriangledown R_{BEP} \left(\tilde{\boldsymbol{\mu}} \right) = \frac{\partial}{\partial \tilde{\boldsymbol{\mu}}} \left(a \sqrt{a^2 + \tilde{\boldsymbol{\mu}}^2} + \varphi \underbrace{\sum_{l=-q}^{q} \sum_{m=0}^{q}}_{l+m \geq 0} \alpha^{|l|+|m|} c \sqrt{c^2 + \left(\tilde{\boldsymbol{\mu}} - S_x^l S_y^m \tilde{\boldsymbol{\mu}} \right)^2} \right), \tag{3.6}$$

and performing the differentiation with respact to $\tilde{\boldsymbol{\mu}}$ results in

$$\bigtriangledown R_{BEP} \left(\tilde{\boldsymbol{\mu}} \right) = \frac{a \tilde{\boldsymbol{\mu}}}{\sqrt{a^2 + \tilde{\boldsymbol{\mu}}^2}} + \varphi \underbrace{\sum_{l=-q}^{q} \sum_{m=0}^{q}}_{l+m \geq 0} \alpha^{|l|+|m|} \frac{c \left(I - S_x^l S_y^m \right) \left(\tilde{\boldsymbol{\mu}} - \tilde{\boldsymbol{\mu}} S_x^l S_y^m \right)}{\sqrt{c^2 + \left(\tilde{\boldsymbol{\mu}} - S_x^l S_y^m \tilde{\boldsymbol{\mu}} \right)^2}}. \tag{3.7}$$

Assuming the same considerations and notation presented in Section 3.2, Equation (3.6) can be rewritten as

$$\bigtriangledown R_{BEP} \left(\tilde{\boldsymbol{\mu}} \right) = H_a \left(\tilde{\boldsymbol{\mu}} \right) \odot \tilde{\boldsymbol{\mu}} + \varphi \underbrace{\sum_{l=-q}^{q} \sum_{m=0}^{q}}_{l+m \geq 0} \alpha^{|l|+|m|} \left[I - S_x^{-l} S_y^{-m} \right] \odot H_c \left(\mathbf{M} \right) \odot \mathbf{M}, \tag{3.8}$$

where $\odot$ is the element-by-element product of two matrices of compatible dimensions, φ is an adjustment parameter to balance terms inside gradient descent, and I is the identity matrix. The matrix $\mathbf{M} = \tilde{\boldsymbol{\mu}}^k - S_x^l S_y^m \tilde{\boldsymbol{\mu}}^k$ is the difference between $\tilde{\boldsymbol{\mu}}^k$ and its version shifted by $S_x^l S_y^m$, and the operators $H_a(.)$ and $H_c(.)$ are defined, respectively, as

$$H_a(x) = \frac{a}{\sqrt{a^2 + x^2}}, H_c(x) = \frac{c}{\sqrt{c^2 + x^2}}, \tag{3.9}$$

and $H_a\left(\tilde{\boldsymbol{\mu}}^k\right) \odot \tilde{\boldsymbol{\mu}}^k$ and $H_c(\mathbf{M}) \odot \mathbf{M}$ are influence functions, as defined in Equation (2.11), resulting from the application of the gradient descent method.

Equation (3.5) can be written in compact form as

$$\hat{\boldsymbol{\mu}}^k = \tilde{\boldsymbol{\mu}}^k - \gamma \bigtriangledown R_{BEP}\left(\tilde{\boldsymbol{\mu}}^k\right), \tag{3.10}$$

and, finally, Equation (3.10) is presented in a expanded form as

$$\hat{\boldsymbol{\mu}}^k = \tilde{\boldsymbol{\mu}}^k - \gamma_k \left(H_a\left(\tilde{\boldsymbol{\mu}}^k\right) \odot \tilde{\boldsymbol{\mu}}^k + \varphi \underbrace{\sum_{l=-q}^{q} \sum_{m=0}^{q}}_{l+m \geq 0} \alpha^{|l|+|m|} \left[I - S_x^l S_y^m\right] \odot H_c(\mathbf{M}) \odot \mathbf{M} \right), \tag{3.11}$$

where γ_k is an adjustment parameter to balance the k-th value of $\tilde{\boldsymbol{\mu}}^k$ with the gradient descent contribution, $\bigtriangledown R_{BEP}\left(\tilde{\boldsymbol{\mu}}^{k-1}\right)$, as defined in Equation (3.8).

It is important to clarify that, in Equation (3.4), $\boldsymbol{\mu}$ appears with the upper index $k-1$ instead of k because the previous result of the gradient descent, $\boldsymbol{\mu}^{k-1}$, feeds the calculation of the current value, $\boldsymbol{\mu}^k$, and this is the manner in which gradient descent works. In contrast, Equation (3.11) shows $\tilde{\boldsymbol{\mu}}$ with upper index k (as in $\hat{\boldsymbol{\mu}}$) rather than $k-1$ because $\tilde{\boldsymbol{\mu}}$ is obtained in the same interaction step, k, as $\hat{\boldsymbol{\mu}}$, but in a previous stage denoted by the upper mark "tilde" ($\tilde{.}$), while the current stage is denoted by the upper mark "hat" ($\hat{.}$).

3.3 Third stage - Total Variation (TV) minimization by Soft-threshold Non-linear Filtering

The third stage, total variation (TV) optimization of the Discret Gradient Transform (DGT), is to solve the problem $\boldsymbol{\nu} = D\boldsymbol{\mu}$, where D is not invertible, as proposed by Yu and Wang (2010b), which is written as

$$\mu_{m,n}^k = \frac{1}{4}\left(2\mu_{m,n}^{k,a} + \mu_{m,n}^{k,b} + \mu_{m,n}^{k,c}\right), \tag{3.12}$$

with

$$\mu_{m,n}^{k,a} = \begin{cases} \frac{2\tilde{\mu}_{m,n}^k + \tilde{\mu}_{m+1,n}^k + \tilde{\mu}_{m,n+1}^k}{4} & , D_{m,n}\tilde{\boldsymbol{\mu}}^k < \omega \\ \tilde{\mu}_{m,n}^k - \frac{\omega\left(2\tilde{\mu}_{m,n}^k - \tilde{\mu}_{m+1,n}^k - \tilde{\mu}_{m,n+1}^k\right)}{4D_{m,n}\tilde{\boldsymbol{\mu}}^k} & , D_{m,n}\tilde{\boldsymbol{\mu}}^k \geq \omega \end{cases} \tag{3.13}$$

$$\mu_{m,n}^{k,b} = \begin{cases} \frac{\tilde{\mu}_{m,n}^{k} + \tilde{\mu}_{m-1,n}^{k}}{2} & , D_{m-1,n}\tilde{\boldsymbol{\mu}}^{k} < \omega \\ \tilde{\mu}_{m,n}^{k} - \frac{\omega\left(\tilde{\mu}_{m,n}^{k} - \tilde{\mu}_{m-1,n}^{k}\right)}{2D_{m-1,n}\tilde{\boldsymbol{\mu}}^{k}} & , D_{m-1,n}\tilde{\boldsymbol{\mu}}^{k} \geq \omega \end{cases} \tag{3.14}$$

and

$$\mu_{m,n}^{k,c} = \begin{cases} \frac{\tilde{\mu}_{m,n}^{k} + \tilde{\mu}_{m,n-1}^{k}}{2} & , D_{m,n-1}\tilde{\boldsymbol{\mu}}^{k} < \omega \\ \tilde{\mu}_{m,n}^{k} - \frac{\omega\left(\tilde{\mu}_{m,n}^{k} - \tilde{\mu}_{m,n-1}^{k}\right)}{2D_{m,n-1}\tilde{\boldsymbol{\mu}}^{k}} & , D_{m,n-1}\tilde{\boldsymbol{\mu}}^{k} \geq \omega, \end{cases} \tag{3.15}$$

where ω is a pre-established threshold; $\tilde{\boldsymbol{\mu}}^{k} = \left[\tilde{\mu}^{k}\right]_{mn}$, with $m = 1, 2, ..., H$ and $n = 1, 2, ..., W$, with W e H the width and height of the reconstructed image, respectively, and $D_{m,n}\tilde{\boldsymbol{\mu}}^{k}$ is the DGT matrix, as defined in Equation (2.1).

As explained in detail in (YU; WANG, 2010b) and observing Equation (3.13), when $D_{m,n}\tilde{\boldsymbol{\mu}}^{k} < \omega$, the values of $\tilde{\mu}_{m,n}^{k}$, $\tilde{\mu}_{m+1,n}^{k}$ e $\tilde{\mu}_{m,n+1}^{k}$ must be adjusted so that $D_{m,n}\tilde{\boldsymbol{\mu}}^{k} = 0$. This means that if neighbouring pixels in the reconstructed image are very close in value, it is likely that they have equal (or very close) values in the "real image". Then, the method smooths the region around the pixel so that they look alike. Alternately, when $D_{m,n}\tilde{\boldsymbol{\mu}}^{k} \geq \omega$, the goal is to reduce $\left(\tilde{\mu}_{m,n}^{k} - \tilde{\mu}_{m+1,n}^{k}\right)^2$ and $\left(\tilde{\mu}_{m,n}^{k} - \tilde{\mu}_{m,n+1}^{k}\right)^2$, but not cancel them. In this case, the method "recognizes" the differences between values of neighbouring pixels as quite meaningful to be totally eliminated. Instead, the differences are just softened.

4 Experiments and results

In the experiments, we used the synthetic images presented in Section 1.7, that is, FORBILD head phantom, Shepp-Logan head phantom, FORBILD abdomen phantom and a Checkerboard synthetic image, as ilustrated in Figure 12. The signal from the CT equipment is simulated according to the model in Equation (1.21) addressing two scenarios: (1) regular dosage with a regular number of projection (180 scanning angles), and (2) low dosage, considering a limited number of projections (meaning a limited number of scanning angles). On the image reconstruction side, we use the model $\mathbf{y} = \mathbf{A}\mathbf{x} + \boldsymbol{e}$, which, as discussed in Sections 1.4 and 1.7, denotes an inverse and ill-posed problem, where $\mathbf{A}$ $(N_I \times N_J)$ is the matrix that describes the capture system, $\mathbf{x}$ $(N_J \times 1)$ is the phantom represented lexicographically and $\boldsymbol{e}$ $(N_J \times 1)$ is the error, whose features were presented in Section 1.7. It is worth remembering that $\mathbf{y}$ is the input noisy signal from the CT scan process, $\mathbf{x}$ is the image we intend to reconstruct from the input signal, which was represented as $\boldsymbol{\mu}$ in Chapters 1, 2 and 3.

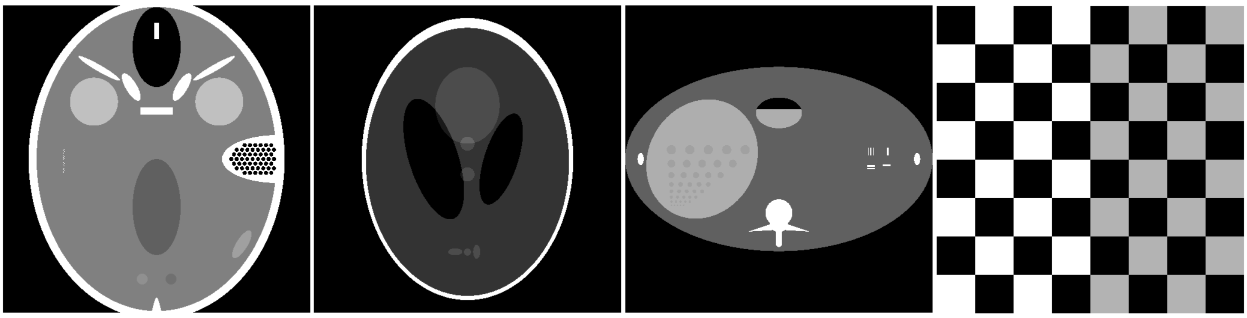

(a) (b) (c) (d)

Figure 12 – The original images: **(a)** FORBILD head phantom, **(b)** Shepp-Logan head phantom **(c)** FORBILD abdomen phantom, and **(d)** Checkerboard.

By improving the system description, $N_I = n_l n_\theta$ is the number of projections, where n_l is the number of projection lines (i.e., the number of detectors) for each scan angle, and n_θ is the total number of scan angles. n_θ is the parameter whose value should be changed when the intention is to set a new dosage value, i. e., when we want to define a different (lower) number of projections, N_I. The image has dimensions $d \times d$, where $d = \sqrt{N_J}$. In the tests with regular dosage, we used $n_l = 300$, $\boldsymbol{\Theta} = \{0°, ..., 180°\}$ (meaning $n_\theta = 181$), $d = 512$, and therefore, $N_I \, (= n_l n_\theta) = 54,300$ and $N_J \, (= d^2) = 262,144$. Thus, $\mathbf{A}$ has dimensions $54,300 \times 262,144$, which are compatible with the dimensions of $\mathbf{y}$ and $\boldsymbol{\mu}$, respectively, i.e., $54,300 \times 1$ and $262,144 \times 1$. For low dosage we maintain all parameters as defined above, except the number of scanning angles, n_θ. Thus, we consider subsets of $\boldsymbol{\Theta}$, i.e., equally spaced sets of integer values between 0 and 180 degrees named $\boldsymbol{\Theta}_g$. For example, $\boldsymbol{\Theta}_{g=5} = \{0, 45, 90, 135, 180\}$ would be a possible subset, in which the $g = 5$ angles are equally spaced at 45 degrees[1]. Using this notation, $\mathbf{\Theta}$ is equivalent to $\mathbf{\Theta}_{180}$, meaning that there are $g = 180$ scan angles equally spaced by 1 degree. In the experiments with low dosage the sets $\mathbf{\Theta}_g$, with g in $\{15, 30\}$ will be used. $\mathbf{A}$ was obtained for a parallel architecture scanner.

Although the focus of this Thesis is the reconstruction of X-rays CT images of low-dose, we dedicate a section of tests to reconstruction with regular dosage. As discussed in Section 1.1 and again in the begining of this chapter, we promote regular dosage by scanning fully through 180 degrees, generating a set of projections every 1 degree scanned. For both normal and low dosages we will perform tests using the SART, SART+DGT, SART+BEP+DGT – which is our proposal – and FPB techniques. The latter is a non-iterative technique, or a direct reconstruction technique, but is considered here because it is still used as a basis for comparison in current works (CUI et al., 2014; KIM et al., 2016; BAO et al., 2018). For each of the iterative methods tested, it was arbitrarily established that the iterator, k, ranges from 1 to limit, L, with $350 \leq L \leq 5000$. In order to compress the notation, especially in tables and graphs, we call the SART method as "A", SART+DGT as "B", SART+BEP+DGT as "C" and FBP as "D".

Because Gaussian noise and Poisson process are random, each experiment is performed a considerable number of times[2], defined arbitrarily as 101 executions by experiment, according to Hines et al. (2003). The result of each execution is presented both as a SSIM and a PSNR value, and the results of the experiment are presented as the mean of the 101 SSIM and PSNR values. Following are the tests for regular and low dosages[3].

4.1 Regular dosage tests and results

In the batch of tests with regular dosage, as already mentioned, we consider $n_\theta = 180$ scanning angles, which represents, in our model, a normal amount of photon emission (which can be understood as a normal radiation dosage), and the main results appear in Tables 1 and 2. Although the photon detection process is Poissonian, we consider that the amount of photons detected is sufficient for the signal to be influenced by Gaussian additive noise. Thus, the input signal can be written as $\boldsymbol{y}_{\mathcal{N}} = \mathcal{R}(I) + \mathcal{N}_g$, as in Eq. (1.21).

[1] However, this should not be used because the number of projection lines, $N_I = n_l g$, is insufficient for a reasonable reconstruction.

[2] The idea of using the average of a considerable number of iterations is based on the central limit theorem, which states that the arithmetic mean of a sufficiently large number of iterations of independent random variables will be approximately normally distributed, regardless of the underlying distribution, provided that each iteration has a finite expected value.

[3] It is important to note that the result presented for each experiment (with a particular additive Gaussian noise, or a certain number of projections) is the mean of 101 executions performed. Each execution produces a particular SSIM and the PSNR result. We do not average pixels in any reconstructed image, but the SSIM an PSNR of the 101 executions performed for each testing case.

Table 1 – Comparison of CT reconstruction methods A (for SART), B (for SART+DGT), C (for SART+BEP+DGT) and D (for FBP) applied to reconstruction of the FORBILD abdomen phantom, Shepp-Logan phantom, FORBILD head phantom and Checkerboard images using PSNR metric. Higher values are highlighted.

Image	Method	SNR (dB) Regular dosage					
		60	46	40	32	26	20
FORBILD abd.	A	73.6756	73.4856	72.9461	70.3194	66.1661	60.7454
	B	**82.9253**	**82.7136**	**82.1934**	**79.9417**	**76.4433**	**71.7315**
	C	82.1618	82.0177	81.6321	79.5944	76.1299	71.2977
	D	61.6066	61.5032	61.3771	61.0078	60.3821	58.9827
Shepp-Logan	A	68.5743	68.5547	68.4941	68.0870	66.8950	63.9715
	B	76.5842	76.5662	76.5114	76.2250	75.3923	73.2920
	C	**76.7768**	**76.7664**	**76.7161**	**76.4297**	**75.5958**	**73.3809**
	D	63.4764	63.4045	63.2907	63.0066	62.5260	61.4253
FORBILD head	A	67.3267	67.1976	66.8216	64.8104	61.1696	56.0221
	B	**73.2859**	**73.1754**	**72.9275**	**71.7489**	**69.6805**	**66.3748**
	C	73.1939	73.1036	72.8559	71.7029	69.5673	65.9970
	D	57.5840	57.4722	57.3508	56.9422	56.2399	54.9444
Checkerboard	A	62.9987	62.9021	62.6139	60.9975	57.7587	52.8747
	B	**72.5736**	**72.5045**	**72.2997**	**70.9555**	68.1817	**64.2046**
	C	72.1864	72.1481	71.9838	70.9159	**68.2774**	64.1873
	D	55.6984	55.5890	55.4443	55.0544	54.1965	53.2041

A careful discussion of this model was conducted in Section 1.7. The means (of 101 SSIM and PSNR executions) of the results for each testing combination are shown in Table 1 for PSNR metric, and Table 2 for SSIM metric, both comparing the reconstructed image with the FORBILD head phantom, Shepp-Logan phantom, FORBILD abdomen phantom and Checkerboard synthetic images, respectively, for $k = 350$ iterations. The number of iterations was chosen for presenting a good cost-benefit relation between result and processing time. Tests were performed for the following signal-to-noise ratios (SNR): 20 dB, 26 dB, 32 dB, 40 dB, 46 dB and 60 dB. The SART implementation used $\lambda = 1$, such as in (XU et al., 2011; HANSEN; SAXILD-HANSEN, 2012). The DGT implementation maintained $\beta = 1$, as discussed in Section 2.1, and used as a threshold, ω, the average of the DGT for each k iteration. The BEP implementation used $\gamma = 0.001$, $q = 3$, $\alpha = 0.6$, $a = 0.1$ and $c = 0.5$, as in (CHARBONNIER et al., 1997; ZENG; YANG, 2010; ZENG; YANG, 2013). In more detail, the parameter γ, as explained in Section 3.2, is a weighting factor for the constraint R_{BEP}. The parameter α, as explained in Section 2.2, is a weighting factor that attenuates the contribution of ρ_a according to the distance $|l| + |m|$ related to pixel j, and the parameter q is the limiter of l and m, as described in Section 2.2. Parameters are used with the same values for all methods where they apply and for all reconstructed images.

By definition, PSNR is the ratio between the maximum possible signal power and the noise power that affects the fidelity of its representation, and it is straightforward that the PSNR value decreases as Gaussian noise increases. Thus, the reader can observe in Table

Table 2 – Comparison of CT reconstruction methods A (for SART), B (for SART+DGT), C (for SART+BEP+DGT) and D (for FBP) applied to reconstruction of the FORBILD abdomen phantom, Shepp-Logan phantom, FORBILD head phantom and Checkerboard images using SSIM metric. Higher values are highlighted.

Image	Method	SNR (dB) Regular dosage					
		60	46	40	32	26	20
FORBILD abd.	A	0.3874	0.3631	0.3067	0.1567	0.0639	0.0207
	B	0.9803	0.9781	0.9719	0.9264	0.8095	0.6359
	C	**0.9807**	**0.9794**	**0.9756**	**0.9372**	**0.8226**	**0.6471**
	D	0.7181	0.6503	0.5825	0.5120	0.4417	0.3201
Shepp-Logan	A	0.3500	0.3419	0.3197	0.2278	0.1307	0.0636
	B	0.9662	0.9656	0.9639	0.9529	0.9208	0.8156
	C	**0.9755**	**0.9751**	**0.9741**	**0.9674**	**0.9448**	**0.8473**
	D	0.6365	0.5966	0.5322	0.4732	0.4279	0.3403
FORBILD head	A	0.2547	0.2361	0.1979	0.1133	0.0608	0.0272
	B	0.9511	0.9468	0.9349	0.8692	0.7102	0.4771
	C	**0.9579**	**0.9549**	**0.9463**	**0.8935**	**0.7395**	**0.4971**
	D	0.6365	0.5966	0.5322	0.4732	0.4279	0.3403
Checkerboard	A	0.1153	0.1124	0.1079	0.0919	0.0689	0.0390
	B	0.8838	0.8783	0.8608	0.7745	0.6220	0.4118
	C	**0.9424**	**0.9394**	**0.9310**	**0.8776**	**0.7367**	**0.4861**
	D	0.4086	0.3587	0.3437	0.3153	0.2604	0.1933

1 that methods B (SART+DGT) and C (SART+BEP+DGT) present near PSNR values, while methods A (SART) and D (FBP) presents the lower ones, considering that the same level of Gaussian noise is added. The FBP method has the worst performance regardless of the signal-to-noise ratio in dB (SNR dB) of the input signal or the reconstructed image.

From the point of view of the SSIM metric, for all reconstructed images, the proposed method (C) presents significantly better results as the SNR dB decreases (noise increases), as shown in Table 2. In more detail, as the SNR dB decreases, the SSIM results diverge more clearly between the methods C (SART+BEP+DGT) and B (SART+DGT) for all the results observed in Table 2. It is noteworthy that the SSIM and PSNR metrics are consistent with each other and this reinforces the assumption that the SSIM metric works as a quality indicator for the reconstruction of CT images. The SSIM metric tends to consider more effectively the structural features of the image(WANG et al., 2004). PSNR result, in turn, compares the overall power of the reconstructed image without taking into account its structural characteristics.

Figure 13 shows one of the reconstructed FORBILD head phantom images (among 101 executions) for methods A (SART), B (SART+DGT), C (SART+BEP+DGT) and D (FBP) with SNR = 40 dB. The image of Figure 13a, and its detailed region in Figure 13e, represents the SART reconstruction. Images in Figure 13b and Figure 13f represents the reconstruction for the SART+DGT method. Figures 13c and 13g represents the reconstruction for SART+BEP+DGT method, and Figures 13d and 13h, the reconstruction using the FBP method. The arrows in the images show relevant elements of comparison and the visual results are coherent with Table 2. Figure 13g shows more clearly defined details compared to Figure 13f. Figure 13h, result of FBP reconstruction, shows clearly defined details, but also shows stripes and marks common in the FPB reconstruction process. As it can be seen in Table 2, SSIM results are favorable to the proposed method, SART+BEP+DGT, compared to the iterative methods SART, without any regularization, and SART+DGT, which regularizes the solution using l_1 norm. We assign this difference to the ability of the proposed method to remove noisy signal from the SART step and deliver a better quality signal for the DGT step, which applies the minimization by total variation in l_1 norm.

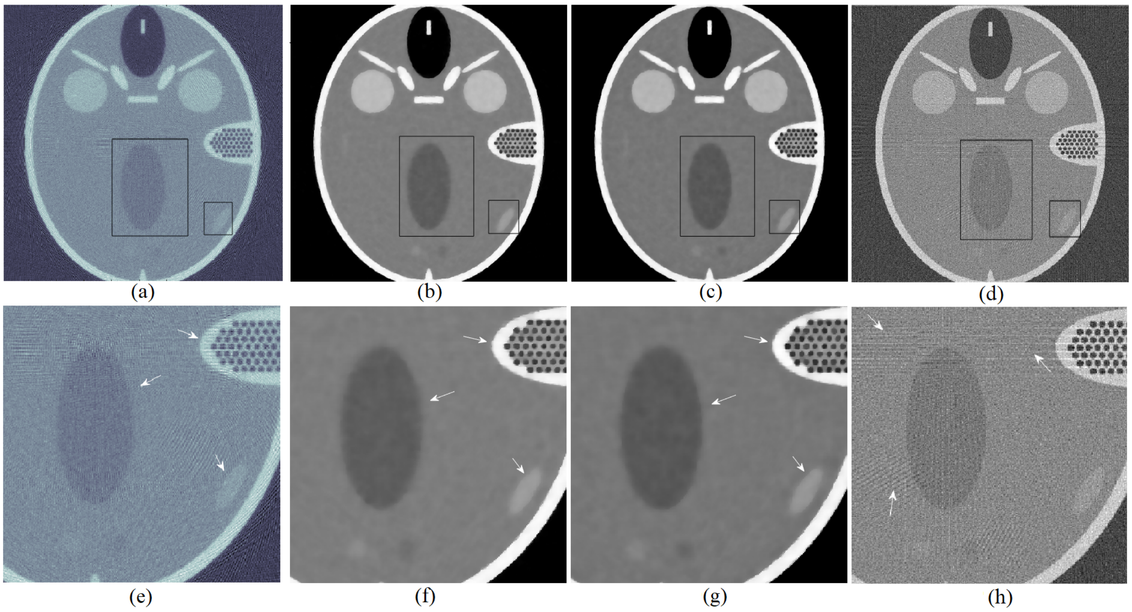

Figure 13 – Comparison of images reconstructed with **(a)** SART, **(b)** SART+DGT, **(c)** SART+BEP+DGT, and **(d)** FBP methods, and their respective details in **(e)**, **(f)**, **(g)** and **(h)** for the FORBILD head phantom input signal with Gaussian additive noise of 40 dB. This plot represents one single aleatory reconstruction experiment.

Figure 14 shows the results for methods A, B, C and D for the Shepp-Logan head phantom with SNR= 60 dB. As can be seen, method B (SART+DGT) and C (SART+BEP+DGT), repectively, Figures 14f and 14g, shows consistent edges and relatively low noise, if in comparison with metods A (SART) and D (FBP), Figures 14e and 14h. In addition, we can observe that, as discussed in Section 1.4, the restriction by l_1 norm tends to produce artificial edges on the smooth areas, as highlighted in Figure 14f. Note that these artifacts do not appear in the reconstruction shown in Figure 14g, performed by the proposed method (SART+BEP+DGT), while preserving the edges with certain quality. We attribute this behavior to the introduction of BEP in the process, as discussed in Section 3.2. In more detail, the l_p norm imposed by BEP smoothes the relatively small differences between neighbor pixels, minimizing the impact of the later applied l_1 norm. The proposed method presents SSIM results subtly superior to the other methods, as shown in Table 2. Methos B and C present similar noise level according to PSNR metric, as shown in Table 1. It is noteworthy that methods A and D visually produce better defined edges, but with a large amount of noise, as indicated in Table 1.

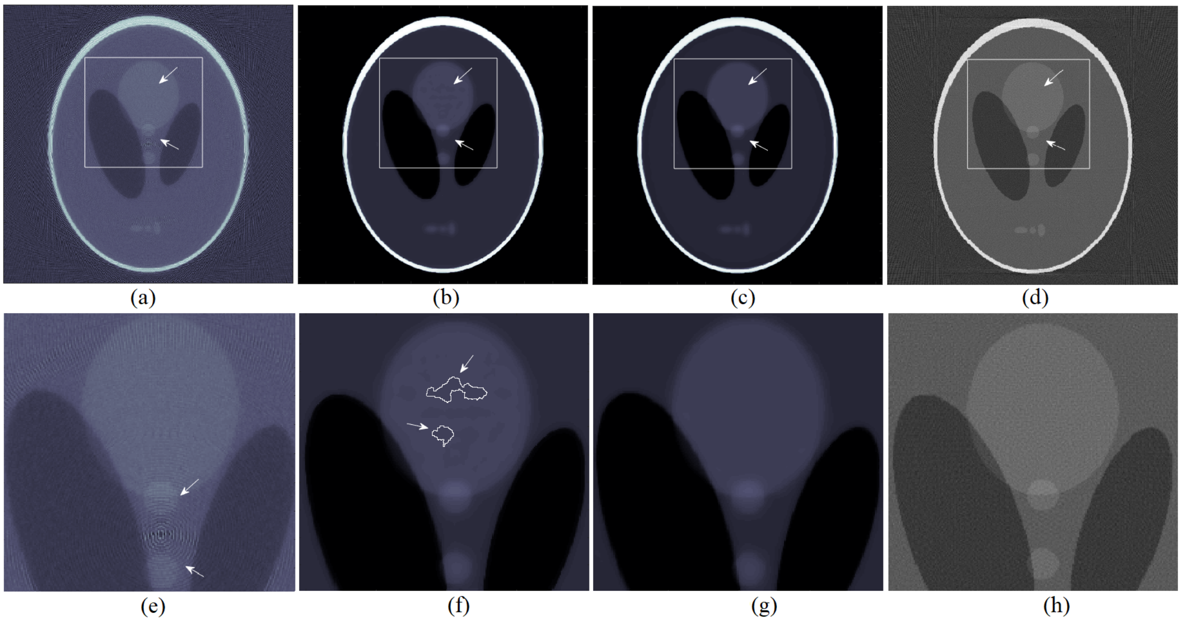

Figure 14 – Comparison of images reconstructed with **(a)** SART, **(b)** SART+DGT, **(c)** SART+BEP+DGT, and **(d)** FBP methods, and their respective details in **(e)**, **(f)**, **(g)** and **(h)** for the Shepp-Logan head phantom input signal with Gaussian additive noise of 60 dB. This plot represents one single aleatory reconstruction experiment.

Figure 15 shows the reconstruction of the FORBILD abdomen phantom for SNR 46 dB. As usual, the A (SART) and D (FBP) methods deliver the noisiest reconstructions. However, this time, SART+DGT and SART+BEP+DGT reconstructions present visually very close results, and PSNR and SSIM values in Tables 1 and 2 support this observation.

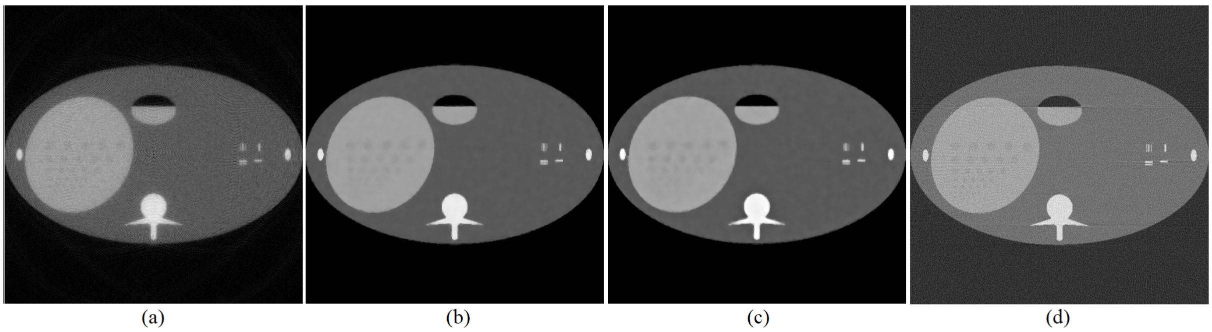

Figure 15 – Comparison of images reconstructed with **(a)** SART, **(b)** SART+DGT, **(c)** SART+BEP+DGT, and **(d)** FBP methods for the FORBILD abdomen phantom input signal with Gaussian additive noise of 46 dB. This plot represents one single aleatory reconstruction experiment.

Next, Figure 16 shows the reconstruction of the synthetic Checkerboard image. This is not a typical image for CT, but serves as a counterpoint for the analysis of the methods. The A (SART) and D (FBP) methods present characteristic noise from their reconstruction processes. Methods B (SART+DGT) and C (SART+BEP+DGT) present visually similar results. However, when checking the data in Table 2, as well as the graphs of Figures 17j,k,l, we observe that their SSIM values are markedly different. This difference is associated with the distance between the gray level of each pixel of the reconstructed image and its original pair. As an example, we chose two boxes within the checkerboard, named 1 and 2. Then, we calculated the mean intensity of the pixels in boxes 1 and 2 in the reconstructed SART+DGT image and in SART+BEP+DGT image, as well as with the correspondent boxes in the original Checkerboard image. For boxes 1 and 2 in Figure 17b, the average of pixel intensities is, respectively, 0.9465 and 0.6579. In Figure 17c, the same calculation results in 0.9696 and 0.6693. Finally, the mean intensities of the pixels in boxes 1 and 2 of the orignal image are, respectively, 1 and 0.7. Therefore, the differences between the boxes 1 and 2 of the reconstructed images in relation to the original image favor (are smaller for) the reconstruction using the SART+BEP+DGT method. Consequently, the average pixels intensities for the reconstruction with the proposed method are closer to original image in comparison to the other methods. This is the working principle of the SSIM metric. Indeed, structural similarity compares luminance, contrast and structure between images (WANG et al., 2004).

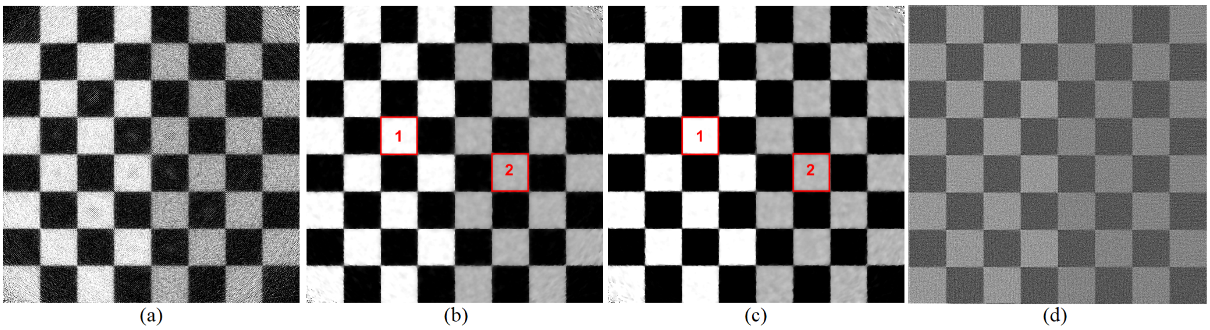

Figure 16 – Comparison of images reconstructed with **(a)** SART, **(b)** SART+DGT, **(c)** SART+BEP+DGT, and **(d)** FBP methods for the Cherckerboard synthetic input signal with Gaussian additive noise of 32 dB. This plot represents one single aleatory reconstruction experiment.

In spite of the results obtained so far, by analyzing the reconstruction process more closely (step by step), as shown in Figure 17, it is clear that, the lower the SNR value of (the higher the noise in) the input signal, the earlier the proposed method reaches the final result obtained by the reference method. For example, in the graph of Figure 17a that shows the results for the FORBILD head phantom image, with an SNR of 60 dB, the result of method B (with $k = 350$ steps) is matched by the proposed method, C, in step $k = 239$; in the graph of Figure 17b, with an SNR of 40 dB, the result is matched in step $k = 196$; and in the graph of Figure 17c, with an SNR of 32 dB, the result is reached earlier, in step $k = 118$. SART+BEP+DGT method presents a better response to Gaussian noise in comparison to SART+DGT method with respect to the SSIM metric.

The same behavior can be observed for the Shepp-Logan head phantom. As shown

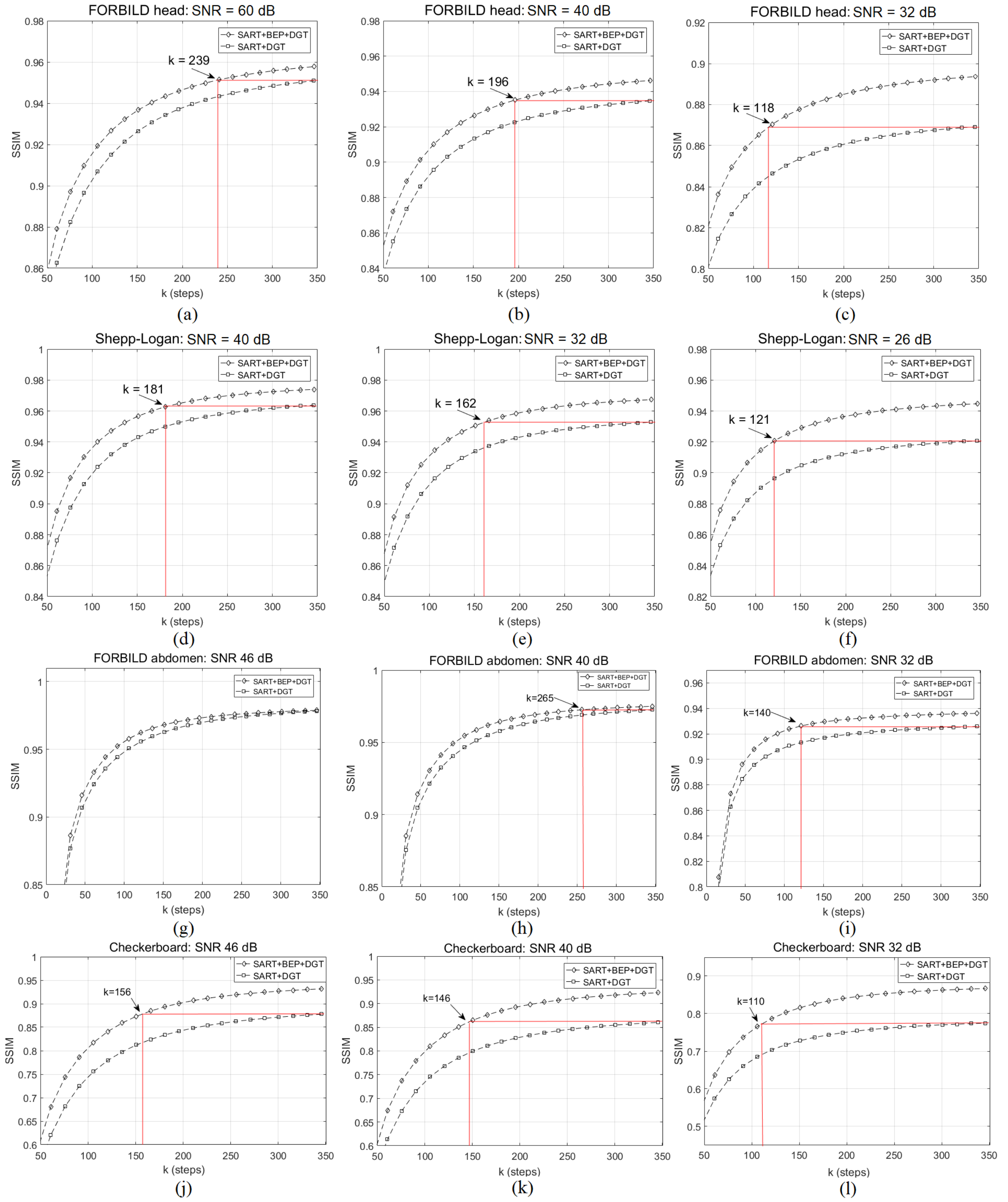

Figure 17 – Comparing reconstruction methods measured by SSIM with SNR values of **(a)** 60 db, **(b)** 40 db, and **(c)** 32 db for the FORBILD head phantom; SNR values of **(d)** 40 db, **(e)** 32 db, and **(f)** 26 db for the Shepp-Logan head phantom; SNR values of **(g)** 46 db, **(h)** 40 db, and **(i)** 32 db for the FORBILD abdomen phantom; and SNR values of **(j)** 46 db, **(k)** 40 db, and **(l)** 32 db for the Checkerboard image. This plot represents a single reconstruction experiment, ramdomly selected.

in Figure 17d, for a Gaussian noise of 40 dB, the result of SART+BEP+DGT method is reached with $k = 181$ steps; for 32 dB, with $k = 162$ steps; and for 26 dB, the result of SART+DGT method is equated with $k = 121$ steps in SART+BEP+DGT method. Figures 17g, 17h and 17i present the evolution of SSIM values for reconstruction methods B and C for the FORBILD abdomen phantom. Figures 17j, 17k and 17l present the same for the

Checkerboard image. In both cases, the behavior is maintained, that is, the SSIM values show greater dissociation between methods B and C (in favor of method C) as the SNR dB decreases (or noise increases). An observation should be made to the graph of Figure 17g. In this case there is no gain of the proposed method compared to the SART+DGT method, since both reach practically the same value for step $k = 350$. Regarding to the SART method, it is not represented step by step in the graphs of Figure 17 because of its low performance when compared with SART+DGT and SART+BEP+DGT values.

In more accurate analysis, Figure 18 shows box plot graphs comparing the reconstruction methods SART+DGT and SART+BEP+DGT for all the phantoms studied in this work, for $k = 350$ iteractions.

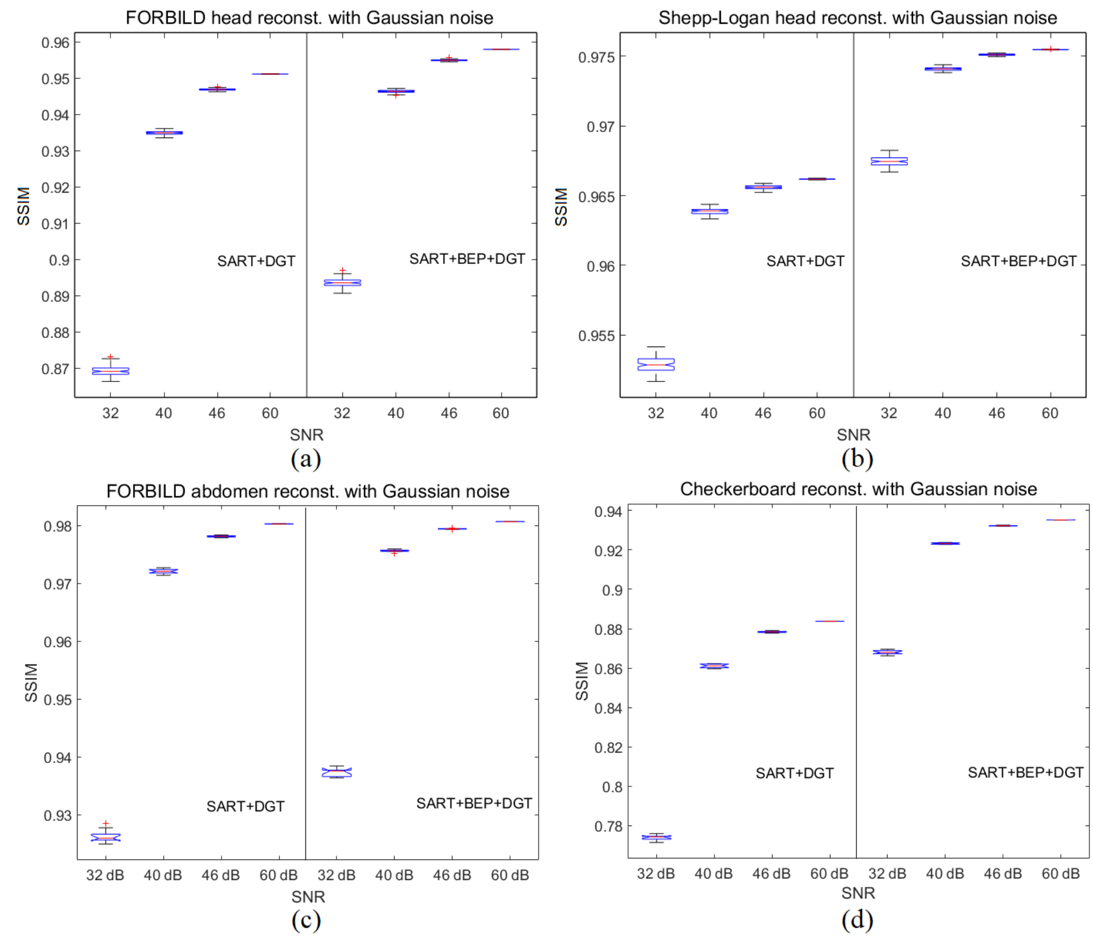

Figure 18 – Box plots of the **(a)** FORBILD head phantom, **(b)** Shepp-Logan head phantom, **(c)** FORBILD abdomen phantom and **(d)** Checkerboard image reconstructions, both with SNR = 32, SNR = 40, SNR = 46 and SNR = 60 dBs for both SART+DGT (left side) and SART+BEP+DGT (right side) for $k = 350$ iteractions. Each box plot is obtained by a sequence of 101 executions of a particular testing case.

Each graph of Figure 18 shows two groups of box plots, one on the left and one on the right, separated by a vertical line in the middle. The left one represents the 101 reconstructions performed for the 32, 40, 46 and 60 dB SNR bands using the SART+DGT method; and the one on the right reproduces the box plots of the proposed method, SART+BEP+DGT under the same conditions.

It is noteworthy that the results of the proposed method outperform the SART+DGT method in terms of the SSIM metric. For example, for the reconstruction of the FORBILD head phantom signal, Figure 18a, the result of the proposed method with SNR = 46 dB overcomes the SART+DGT method result for 60 dB. For reconstruction with Shepp-Logan signal, Figure 18(b), the results are even more prominent. Note that in this case the result of the proposed method with SNR = 32 dB Gaussian noise overlaps the reference method result to 60 dB. The same results holds for FORBILD abdomen phantom and Checkerboard image. All these results are also presented in Table 2. In Appendix A.1, Table 3 shows the mean, median, standard deviation, maximum and minimum for reconstruction methods B (SART+DGT) and C (SART+BEP+DGT) for the FORBILD head, Shepp-Logan, FORBILD abdomen and Checkerboard phamtons for the SNR válues in Figure 18. Each box plot in Figure 18 corresponds to a row in Table 3. It is important to note that there is no overlap between the minimum and maximum values of each experiment.

4.2 Low dosage tests and results

As recommended by the ALARA principle, an alternative to reduce the total amount of radiation applied to a patient is decreasing the number of projections in the acquisition of the CT signal. According to the signal model proposed in Equation (1.21), we will consider the projections as individually influenced by Gaussian additive noise, and the low dosage signal is provided by reducing the number of scanning angles. In the batch of tests with low dosage projections, we consider using the sets of angles $\mathbf{\Theta}_g$, with g in $\{15, 30\}$, where g is the amount of angles in Θ_g. This means $\mathbf{\Theta}_{g=15} = \{0^o, 12^o, 24^o, 36^o, ..., 168^o, 180^o\}$ and $\mathbf{\Theta}_{g=30} = \{0^o, 6^o, 12^o, 18^o, ..., 174^o, 180^o\}$. In our model, these limited number of projections represent a reduced amount of photon emission, which can be understood as a low radiation dosage, as discussed in Section 1.1. All low dosage presented in this section is performed with signal-to-noise ratio (SNR) = 32, 46, and 60 dB. The SART stage used $\lambda = 1$, as in (XU et al., 2011; HANSEN; SAXILD-HANSEN, 2012). The DGT stage maintained $\beta = 1$, as discussed in Section 2.1, and used as a threshold, ω, the average of the DGT for each k iteration. The BEP stage used $\gamma = 0.001$, $\varphi = 0.150$ (Section 3.2), $a = 0.5$, $q = 3$, $\alpha = 0.6$, and $c = 0.1$ (Section 2.2). All parameters were empirically set.

A batch of experiments using the set Θ_g, with g in $\{15, 30\}$, of projections for SART (A), SART+DGT (B), SART+BEP+DGT (C) and FBP (D) for PSNR and SSIM metrics are shown in Appendix A.2, Table 4, for the FORBILD head phantom (FH) and Shepp–Logan head phantoms (SL); and, in Appendix A.3, Table 5, for the FORBILD abdomen phantom (FA) and Checkerboard (CH) synthetic images. Analyzing the results for the PSNR metric with 15 and 30 projections, it is observed that for $k = 350$ steps, the results of the SART+BEP+DGT method present a higher PSNR value in general. The exceptions are the FA and FH images, with an SNR of 32 dB. For $k = 700$ and 1000 steps and 30 projections, the results suggest a balance between methods B and C according to the PSNR metric. Again with the PSNR metric, of 15 projections, results for $k = 700$ steps favor the SART+BEP+DGT method in most tests performed. For the SSIM metric, the proposed method presents interesting results when compared to the SART, SART+DGT and FBP methods.

For the reconstruction of Shepp–Logan head phantom with 15 angles of projection, Figure 19 shows the evolution of the SSIM and PSNR values for SART+BEP+DGT (proposed), SART+DGT, and pure SART methods for SNR = 60 dB. In this particular experiment, marker 1 in Figure 19a indicates the highest SSIM value, 0.9240, reached by the proposed method and corresponding to the highest PSNR value, 72.7103, indicated by marker 1 in Figure 19b. Marker 2 shows in Figures 19a and 19b, respectively, the SSIM (0.8819) and PSNR (71.7521) values obtained in step $k = 551$. Marker 3 in Figure 19b highlights the point at which the SART+DGT method reaches the same PSNR value as the proposed method, in step $k = 1015$, approximately, and the graphs in Figure 19 agree with Table 4, Appendix A.2.

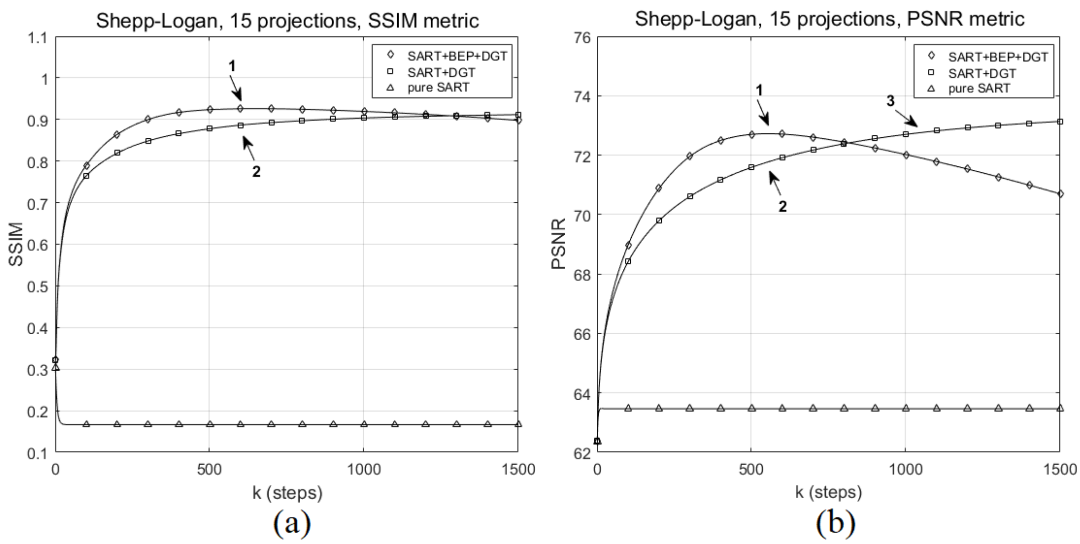

Figure 19 – Evolution of (**a**) SSIM and (**b**) PSNR values for the reconstruction of the Shepp–Logan phantom with 15 projections for pure SART, SART+DGT, and SART+BEP+DGT methods with SNR = 60 dB..

Looking closely at Figures 20b,c, it is possible to note the presence of random noise (indicated by the white arrows) that manifests as small white dots in Figure 20b, while in Figure 20c this phenomenon is not easily perceived. This is because the BEP regularization used in the proposed method (Figure 20c) tends to eliminate noise faster. For reconstructed images with such a small number of projections (15 projections), the noise level in the initial steps of the process is relatively high, and the application of the l_p norm, $1 < p < 2$, through BEP restriction tends to eliminate relatively large differences in comparison to the l_1 norm restriction with DGT. Even so, reconstruction performed by the SART+DGT method produces a more homogeneous image, as shown in Figure 20b, but images in Figure 20b,c reaches the same PSNR value, 72.7103, in different k steps, respectively, $k = 1015$ and $k = 551$. Thus, method C is, in this sense, more efficent them the other iterative methods presented. This is also related to the elimination of random noise by the introduction of BEP regularization in the reconstruction process. Figures 20a,d presents, respectively, the results of SART and FBP reconstructions. It is important to note that for the FBP reconstruction, in cases of low dosage (few projection angles or limited number of projections), the results are unsatisfactory when compared with iterative methods.

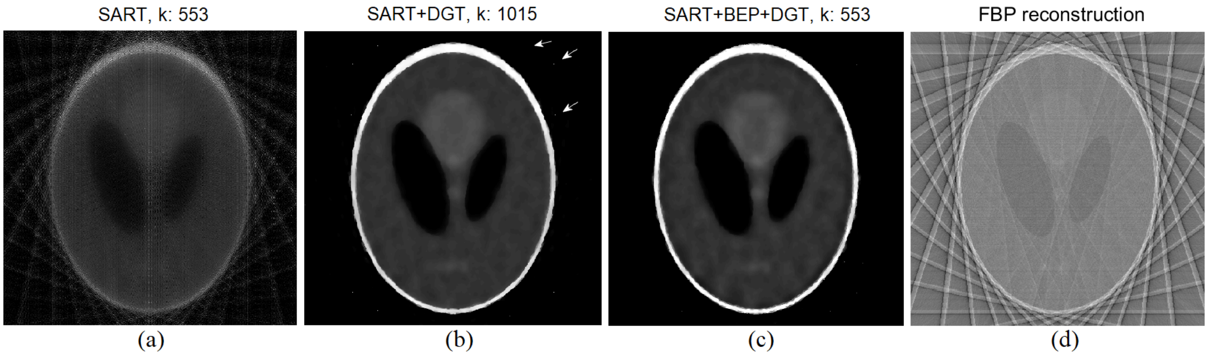

Figure 20 – (**a**) The pure SART reconstruction with $k = 553$ steps, PSNR: 63.4625, SSIM: 0.1662, (**b**) the SART+DGT reconstruction with $k = 1015$ steps, PSNR: 72.7103, SSIM: 0.8920, (**c**) the SART+BEP+DGT reconstruction with $k = 553$ steps, PSNR: 72.7103, SSIM: 0.9240, and (**d**) the FBP reconstruction with PSNR: 62.2881 and SSIM: 0.1480. All with SNR = 60 dB with 15 projections for the Shepp–Logan head phantom.

For the reconstruction of the FORBILD head phantom with 30 projections with SNR = 46 dB, shown in Figure 21, we observe that the best PSNR (70.7700) obtained by the SART+BEP+DGT (proposed) method in step $k = 550$ (Figure 21b, marker 1) is reached by the SART+DGT method in step $k = 650$ (Figure 21b, marker 3). Marker 2 shows, in Figure 21a,b, respectively, the SSIM (0.8728) and PSNR (70.6901) values obtained in step $k = 550$ for SART+DGT method. Note that these values are smaller than those of marker 1, from method SART+BEP+DGT, for both metrics. The SSIM values remain higher for the proposed method, according the graph of Figure 21a. We show the evolution of the pure SART method in terms of SSIM and PSNR for comparison purposes only, since its performance is evidently worse than those of methods B and C.

Observing the reconstructions of methods B and C, shown, respectively, in Figure 22b (with $k = 650$ steps, PSNR = 70.7706, SSIM = 0.8774) and 22c (with $k = 550$ steps, PSNR = 70.7700, SSIM = 0.9015), despite the slight advantage in index, k, and metrics, SSIM and PSNR in favor of SART+BEP+DGT, the images practically do not present a difference, except for a better contrast level presented by Figure 22c. This visual perception regarding contrast has support in the results of structural similarity presented in the graph of Figure 21a. In fact, for the SSIM metric, the proposed method, SART+BEP+DGT, is supeior to SART, SART+DGT and FBP methods. The pure SART reconstruction is shown in Figure 22a, the FBP reconstruction is shown in Figure 22d, and, in both cases, results are not competitive.

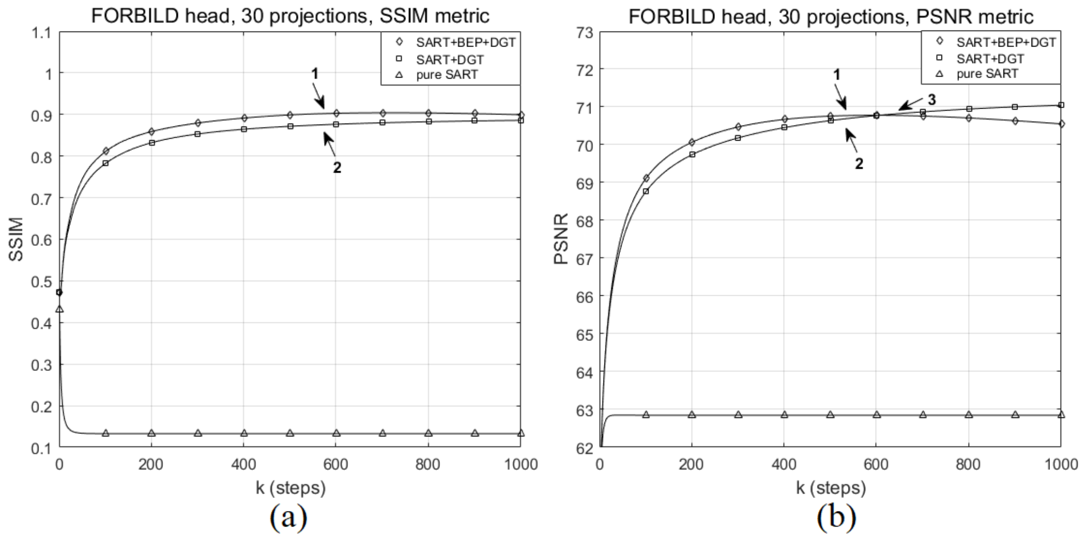

Figure 21 – Evolution of (**a**) SSIM and (**b**) PSNR values for a particular reconstruction of the FORBILD head phantom with 30 projections using the pure SART, SART+DGT, and SART+BEP+DGT methods with SNR = 46 dB.

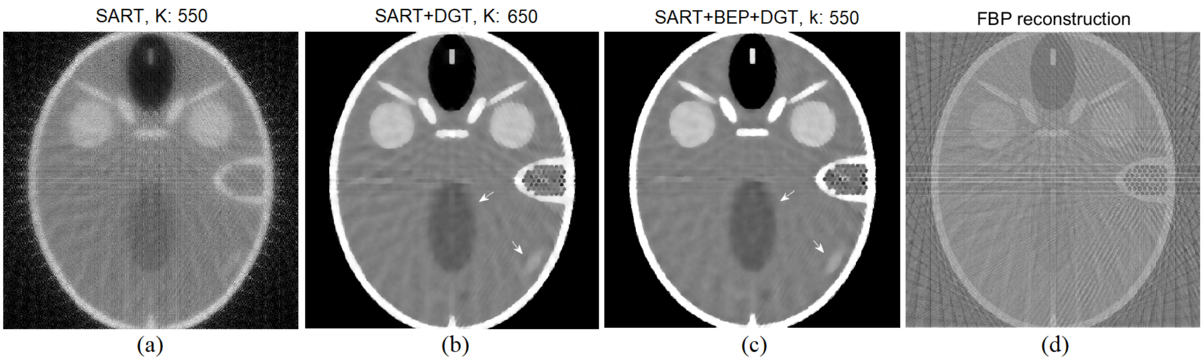

Figure 22 – (**a**) The pure SART reconstruction with $k = 550$ steps, PSNR: 62.8476, SSIM: 0.1332, (**b**) the SART+DGT reconstruction with $k = 650$ steps, PSNR: 70.7706, SSIM: 0.8774, (**c**) the SART+BEP+DGT reconstruction with $k = 550$ steps, PSNR: 70.7700, SSIM: 0.9015, and (**d**) the FBP reconstruction with PSNR: 57.1816 and SSIM: 0.0955. All with SNR = 46 dB with 30 projections for the FORBILD head phantom.

We can argue that the introduction of the BEP stage in CT reconstruction, as theorized in Section 2.3, contributes not only to contrast enhancement but also to improve edge definition, as can be seen in the comparison already made between the images in the Figures 22b,c. In fact, optimization by the l_p norm through the BEP function has the property of preserving both the homogeneous surfaces and the edges, allowing the next step (soft-threshold filtration with DGT) to work with a less noisy image. In this sense, in the third step of the process, presented in Section 3.3, the soft-threshold algorithm has better conditions to separate what can be maintained (approximately homogeneous surfaces) from what must be filtered and smoothed (relevant differences that can be noise or edge).

Figure 23 shows the evolution of the SSIM and PSNR values for the reconstruction with 15 angles of projection with SNR = 60 dB for the FORBILD abdomen phantom using the SART, SART+DGT and SART+BEP+DGT methods. In this particular experiment, marker 1 in Figure 23a indicates the highest SSIM value, 0.9419, reached by the proposed method and corresponding to the highest PSNR value, 77.7180, indicated by marker 1 in Figure 23b, both obtained in step $k = 685$, approximately. Marker 2 shows, in Figures 23a,b, respectively, the SSIM (0.9327) and PSNR (77.2279) values obtained in step $k = 685$ by method SART+DGT. Marker 3 in Figure 23b highlights the point at which the SART+DGT method reaches the same PSNR value of the proposed method, in step $k = 920$, approximately. This means SART+BEP+DGT reaches the PSNR value of 77.7180 at about 235 steps earlier than SART+DGT method.

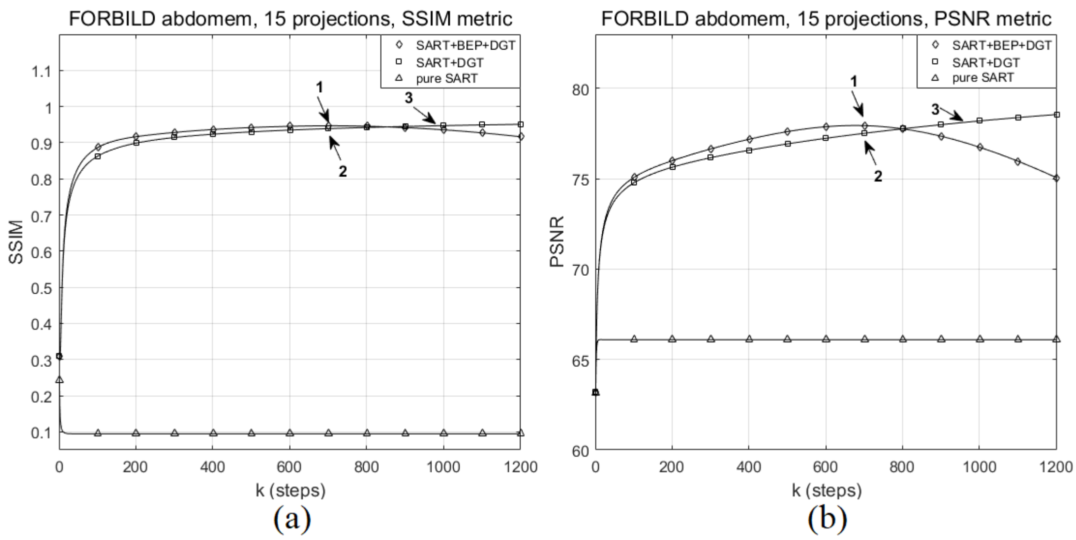

Figure 23 – Evolution of (**a**) SSIM and (**b**) PSNR values for a particular reconstruction of the FORBILD abdomen phantom with 15 projections for pure SART, SART+DGT, and SART+BEP+DGT methods with SNR = 60 dB.

Looking at the images of Figure 24a,b,c,d, representing, respectively, reconstructions with SART, SART+BEP, SART+BEP+DGT and FBP, we can make a few comments. Firstly, the reconstruction with pure SART, Figure 24a, presents itself quite noisy and with edge definition consequently impaired by this noise. However, it tends to present a good contrast, especially with respect to the black background. This, as can be seen so far, is a positive feature of iterative methods in general (HSIEH, 2009c; ANDERSEN; KAK, 1984; KIM et al., 2016; DEáK et al., 2013). Second, the reconstruction using the non-iterative FBP method suffers greatly with the low sampling of the input signal. This poor response to low dosage input is a hallmark of non-iterative methods (SHEPP; LOGAN, 1973; HORN, 1979). Finally, when comparing the methods SART+DGT and SART+BEP+DGT, we observed that the proposed method delivers an image that tends to

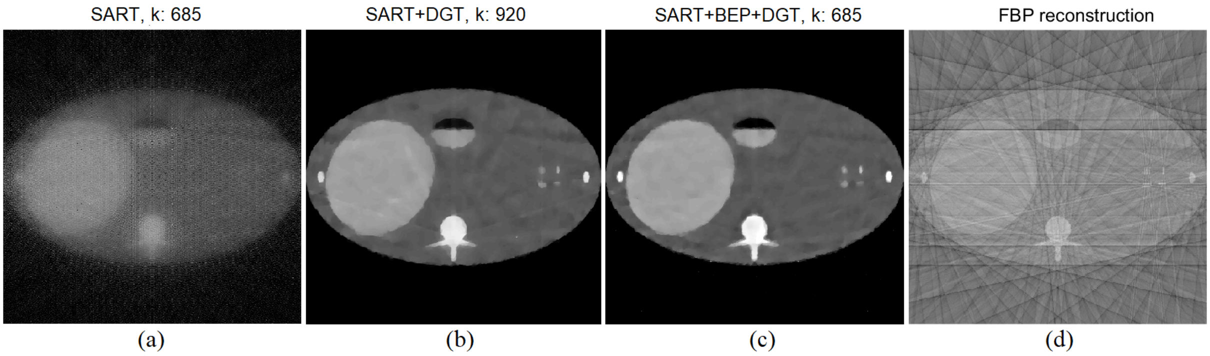

Figure 24 – (**a**) The pure SART reconstruction with $k = 685$ steps, PSNR: 66.0972, SSIM: 0.0946, (**b**) the SART+DGT reconstruction with $k = 920$ steps, PSNR: 77.7197, SSIM: 0.9397, (**c**) the SART+BEP+DGT reconstruction with $k = 685$ steps, PSNR: 77.7180, SSIM: 0.9419, and (**d**) the FBP reconstruction with PSNR: 61.3600 and SSIM: 0.2157. All with SNR = 60 dB with 15 projections for the FORBILD abdomen phantom.

eliminate the prominent radial lines and bands, characteristic of low-dose reconstructions. We attribute this result to the relaxed behavior of the l_p norm, $1 \leq p \leq 2$, with respect to edge preservation in comparison to the l_1 norm. This result is predicted by Daubechies et al. 2004 and is discussed in Section 1.4.

Finally, an example of reconstruction for the Checkerboard image with 30 projections and SNR 46 dB is analyzed in Figures 25 and 26. Note that although the proposed method (SART+BEP+DGT) is overcame by the SART+DGT method in terms of PSNR values, around $k = 450$, as indicated by markings 1 and 2 of Figure 25b, it remains superior in terms of SSIM metrics, as shown in the graph of Figure 25a.

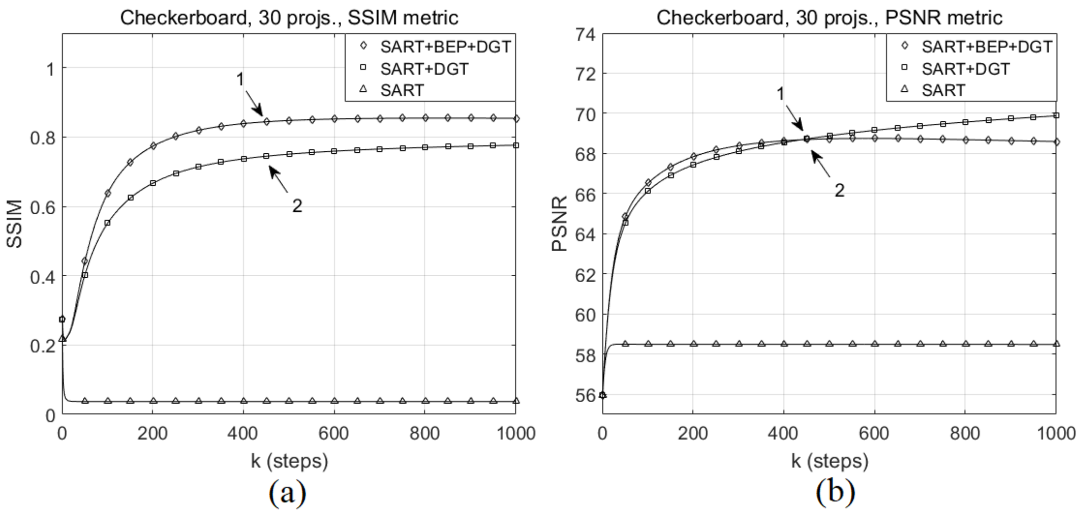

Figure 25 – Evolution of (**a**) SSIM and (**b**) PSNR values for a particular reconstruction of the Checkerboard image with 30 projections for pure SART, SART+DGT, and SART+BEP+DGT methods with SNR = 46 dB.

It is worth noting that the SSIM result presented in Figure 25 implies that, among the reconstructions presented in Figure 26, comparing the average of the gray levels for the same region, the results that are closest to the original image, Figure 12d, are those of the proposed method. In other words, the average gray level of boxes 1, 2 and 3 of Figure 26b, obtained by the SART+DGT method, are, respectively, 0.9439, 0.0555 and 0.6544. For Figure 26c, obtained by the SART+BEP+DGT method, are 0.9640, 0.0205 and 0.6655. It is important to note that although Figure 26 is the representation of a single reconstruction event out of 101 experiments, the average of the intesities of pixels in boxes 1, 2 and 3 is calculated for all the experiments performed. This means that the proposed method produces average gray levels closer to the original values of Figure 12d, which are respectively 1, 0, 0.7.

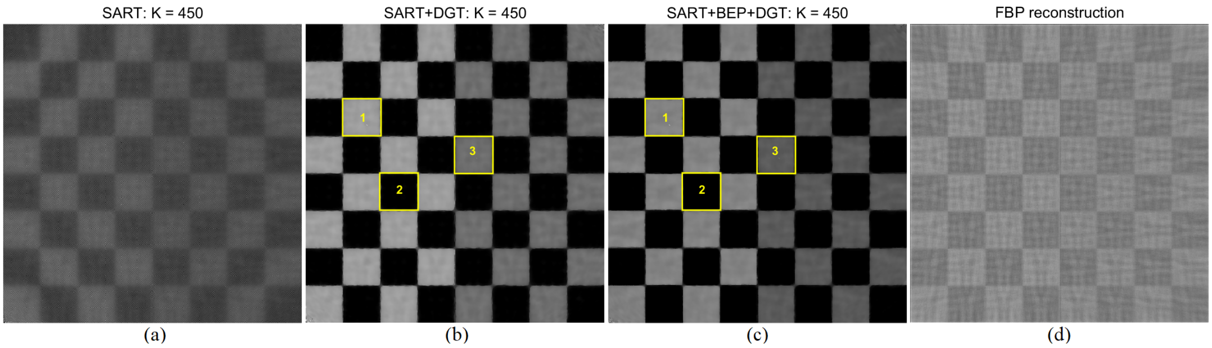

Figure 26 – (**a**) The pure SART reconstruction with $k = 450$ steps, PSNR: 58.4894, SSIM: 0.0371, (**b**) the SART+DGT reconstruction with $k = 450$ steps, PSNR: 68.7222, SSIM: 0.7440, (**c**) the SART+BEP+DGT reconstruction with $k = 450$ steps, PSNR: 68.6883, SSIM: 0.8439, and (**d**) the FBP reconstruction with PSNR: 55.3843 and SSIM: 0.0678. All with SNR = 46 dB with 30 projections for the Checkerboard image.

As previously explained, the experiments are performed 101 times for each combination of composite image experiment, SNR and number of projections and metrics (PSNR and SSIM). Each experiment combination then generates an array of $101 \times k$ values (SSIM or PSNR), where k is the number of steps and each row of the array is an experiment event. Therefore, each value of the SSIM and PSNR charts shown so far is the average of 101 different experiment events. In Figure 27, we show in boxplot the values of some experiments. More specifically, Figure 27a shows the boxplot distribution of the PSNR values for the Shepp-Logan image reconstruction with SNR of 46 and 60 dBs, with 15 projections only for the SART+DGT and SART+BEP+DGT methods for step $k = 600$. Note that this graphs are consistent with the evolution of the PSNR values shown for this specific case in Figure 19b. Figure 27b shows the boxplot distribution of the PSNR values for the FORBILD head phantom image reconstruction with SNR of 46 and 60 dBs, with 30 projections only for the SART+DGT and SART+BEP+DGT methods for step $k = 400$. This graphs are consistent with the evolution of the PSNR values shown for this specific case in Figure 21b. Figure 27c shows the boxplot distribution of the PSNR values for the FORBILD abdomen phantom image reconstruction with SNR of 46 and 60 dBs, with 15 projections only for the SART+DGT and SART+BEP+DGT methods for step $k = 600$. Also this graphs are consistent with the evolution of the PSNR values shown for this specific case in Figure 23b. Finally, Figure 27b shows the boxplot distribution of the PSNR values for the Checkerboard image reconstruction with SNR of 46 and 60 dBs, with 30 projections only for the SART+DGT and SART+BEP+DGT methods for step $k = 300$, and the graphs are consistent with the evolution of the PSNR values shown for this specific case in Figure 25b.

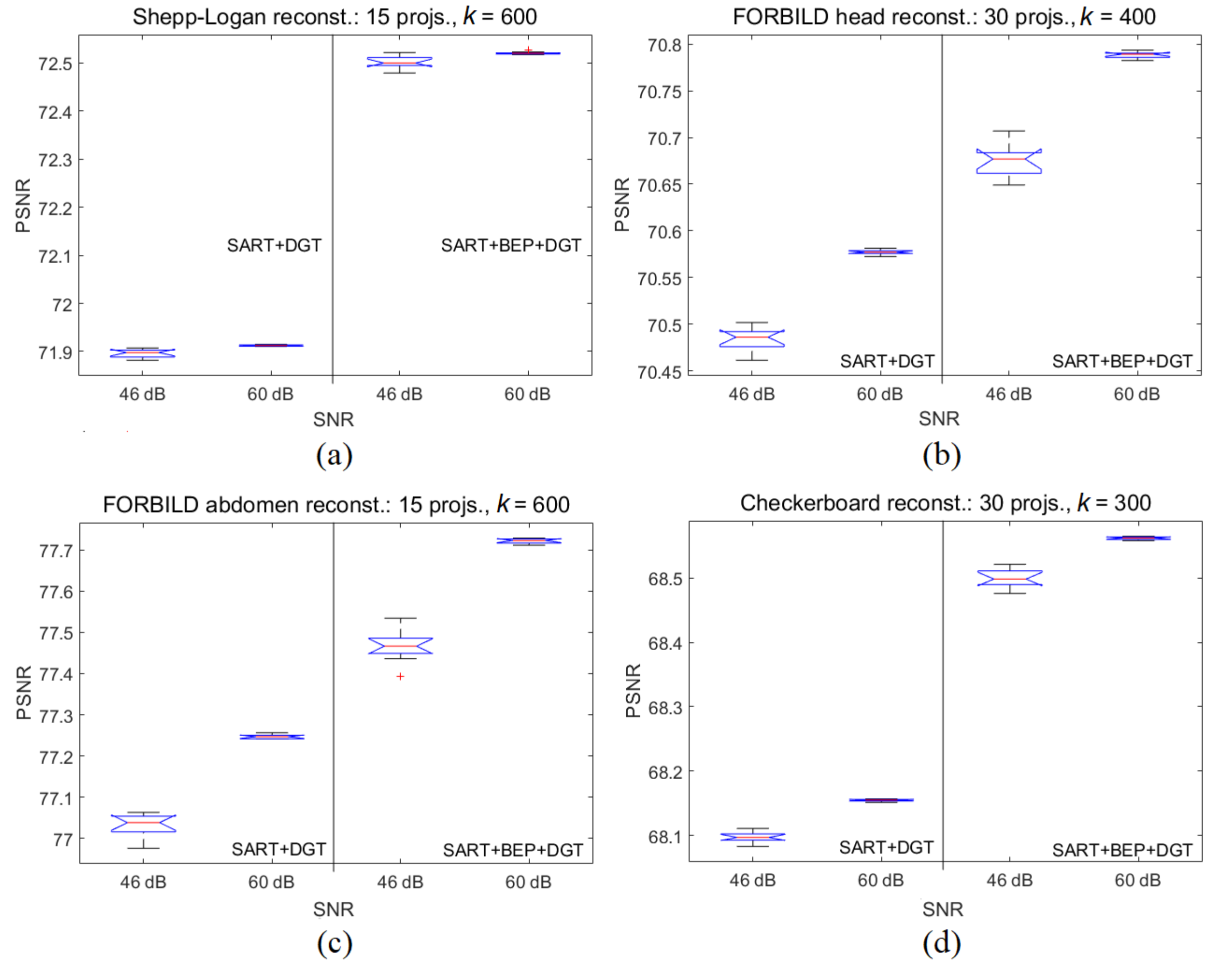

Figure 27 – Box plots of reconstructions for **(a)** Shepp-Logan head phantom (15 projections), **(b)** FORBILD head phantom (30 projections), **(c)** FORBILD abdomen phantom (30 projections) and **(d)** Checkerboard image (15 projections), both with SNR = 46 and SNR = 60 dBs, and for both SART+DGT (left side) and SART+BEP+DGT (right side) for different k iteraction values. Each box plot is obtained by a sequence of 101 executions of a particular testing case.

4.3 Low-dose reconstruction with variation of parameter p in l_p norm

So far, the model proposed in Section 2.2 has been tested with different dosage levels. In these tests it was observed that with fixed norm parameters applied to Equation (3.10) ($a = 1$ for normal dosage, as described in Section 4.1, or $a = 5$ for low dosage, as described at the beginning of Section 4.2), the results are relatively favorable to the proposed method, at least up to a certain number of iterations, k. From there, the PSNR and SSIM results generally worsen together for the reconstructions performed, as can be seen in the graphs of Figures 19,21,23,25. The graphs below, Figure 28, exemplify the SSIM evolution of a particular reconstruction for the FORBILD head phantom, Figure 28a, and Shepp-Logan head phantom, Figure 28b; and PSNR evolution for the same images, shown in Figures 28c and 28d. The number of iteraction is $k = 10000$ steps, with 21 scan angles and no gaussian noise added. The parameter a started from $a = 0.5$, growing linearly up to $a = 1$. The evolution of parameter a started at about step $k = 100$ and ended up to $k = 600$ in both exemples. Explaining in more detail, the BEP stage had norm ranging from $p = 1.5$ to $p = 2$, and, as soon as the norm $p = 2$ is reached, the BEP step is smoothed by gradually decreasing (linearly) the γ coefficient, Equation (3.10), until it reaches 0 at the end of iteractions in step $k = 10000$.

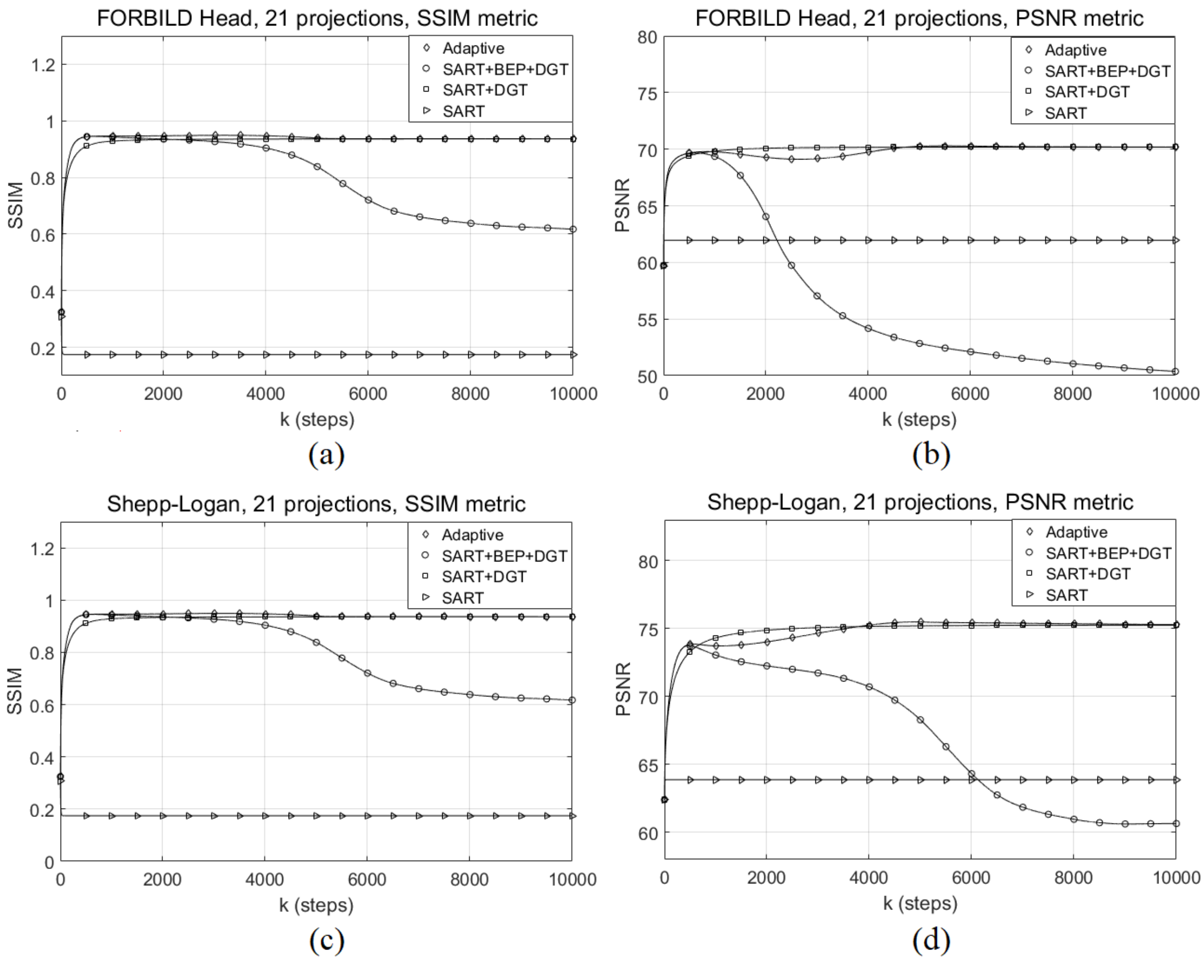

Figure 28 – Values for reconstruction of (**a**) FORBILD head phantom (SSIM values), (**b**) FORBILD head phantom (PSNR values), (**c**) Shepp-Logan head phantom (SSIM values), and (**d**) Shepp-Logan head phantom (PSNR values), for both Adaptive SART+BEP+DGT (show in the grapha as Adaptive), SART+BEP+DGT, SART+DGT and SART for $k = 10000$ iteraction values and 21 projections.

At the beginning of the reconstruction process with low dosage, there are many discrepancies between neighboring pixels that should not be treated as edges. Thus, the BEP stage begins to operate using the standard $p = 1.5$, contributing to the early reduction of such large discrepancies. As the iterations evolve, the large differences tend to be more penalized as p approaches limit value 2. The DGT stage performs the shrinkage of the large differences, contributing to their relative smoothing. The BEP stage with $p = 2$ works as a softener for the soft-threshold filtration algorithm of step 3. With the passage of the iterations, the effect of the BEP stage is mitigated by linear reduction of the γ parameter, until the process is finalized.

With this in mind, it is reasonably acceptable to infer that might exist some kind of adjustment that can be made in parameter a, which defines the norm, so that the process continues to gain in terms of PSNR and SSIM. Therefore, it is important to know how this model behaves in long-term processing. In Figures 29, for the SSIM metric, and, in Figure 30, for PSNR metric, it can be observed that the Adaptive version of SART+BEP+DGT method is consistent with respect to convergence and presents better error reduction in terms of the PSNR and SSIM metrics in comparison to SART and SART+DGT methods.

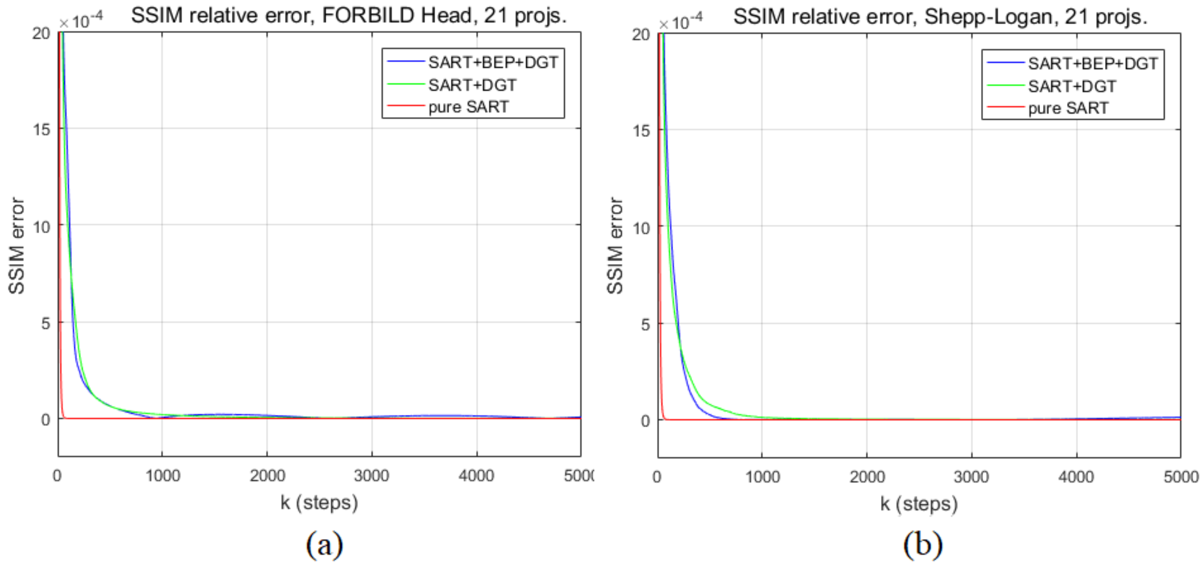

Figure 29 – Structural similarity (SSIM) difference along k iterations, $1 < k \leq 5000$, for pure SART, SART+DGT, and SART+BEP+DGT reconstructions for (**a**) Shepp–Logan head phantom and (**b**) FORBILD head phantom.

In Figure 30, the PSNR value of the k–th iteration is obtained in relation to the previous reconstruction, $k - 1$. In this sense, it is important to note that the SART + DGT method promotes some instability in relation to the PSNR metric. It can be inferred that this behavior is related to the restriction by the l_1 norm, since neither SART, nor SART+BEP+DGT present such behavior.

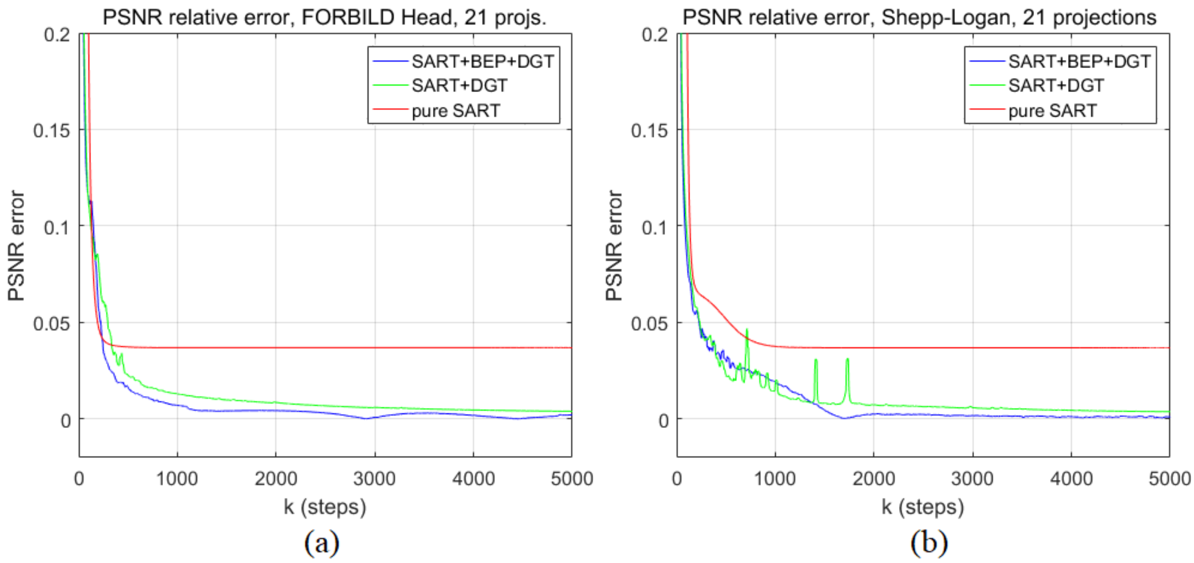

Figure 30 – Peak signal-to-noise ratio (PSNR) difference along k iterations, $1 < k \leq 5000$, for the SART, SART+DGT, and SART+BEP+DGT reconstructions for (**a**) Shepp–Logan head phantom and (**b**) FORBILD head phantom.

5 Conclusion and future works

The proposed method consists of the steps (i) SART reconstruction, (ii) BEP adaptive minimization and (iii) TV minimization via DGT, synthetized in equation (2.13). It presents, in the first steps of the processing, better results for both the SSIM and PSNR metrics, as it can be seen in Chapter 4. These results may indicate reconstructed images with better visual quality, better contrast and edge definition, according to the hypothesis in Subsection 1.8.1.

As mentioned in Section 1.4, regularization with l_1 norm usually leads to the piecewise constant result and hence will produce artificial edges on the smooth areas. The reconstruction with the proposed method tends to mitigate this problem, as highlighted in Figure12g. In that example of Section 4.1, the reduction of artifacts in constant reconstructed areas is attributed to the application of the l_p norm imposed by BEP which smoothes relatively small differences between neighboring pixels, minimizing the impact of the later applied l_1 norm.

In the study performed in Section 4.1, summarized in Figure 15, it is straightforward to note that the lower the SNR value of the input signal, the earlier the proposed method reaches the final result obtained by the reference method. This result is confirmed for practically all the reconstructions, with $k = 350$ steps, presented in Figure 15 with the proposed method in comparison to the SART+DGT method, which applies l_1 norm constraint to the reconstrucion process.

It is important to emphasize also the result presented by the proposed method in relation to the contrast, in comparison with the other methods studied in this work, both for regular dosage and for low dosage, as it can be observed, respectively, in Section 4.1, Figure 14, and Section 4.2, Figure 24. It is reinforced here that, in both cases, the average of the intesities of pixels in boxes 1, 2 and 3 is calculated for all the experiments performed. This means that this result is not a casuality, but represents a standard for the entire set of 101 experiments performed.

At some point the proposed method reaches its maximum PSNR value. From this point forward, the reference method gives higher values of PSNR and, consequently, a less noisy reconstruction (from the point of view of the PSNR metric). Even after the apex of the proposed method with regard to the value of PSNR, the value of SSIM remains, in many of the cases studied, above when compared to the result of the reference method. Best values for SSIM generally result in images with better contrast, as discussed in previous paragraphs, and this is very important for artifact viewing and contour distinction in the reconstructed image. Structural similarity works considering morphological features in the evaluation of reconstruction results and, for this reason presents results more suitable to human standards, when compared with the PSNR metric.

Since we injected noise into the signal used to perform the reconstruction, as discussed in Section 1.7, in all the tests performed in Sections 4.1 and 4.2, it is important to note that the experiments are performed 101 times for each combination of composite image experiment, SNR and number of projections for SSIM and PSNR metrics. This procedure is based on the Central Limit Theorem, which states that the arithmetic mean of a sufficiently large number of iterations of independent random variables will be approximately normally distributed, regardless of the underlying distribution, provided that each iteration has a finite expected value. However, it is observed that we do not average pixels in any reconstructed image, but the SSIM an PSNR of the 101 executions performed for each testing case shown in the graphs of Chapter 4.

In Section 4.3 it is argued whether PSNR and SSIM levels can be mantained for a recosnctruction (without considering addition of Gaussian noise) with the proposed method. As it can be seen in the graphs in Figure 26, both the PSNR and SSIM values remain close (sometimes above) to the corresponding values for the SART+DGT method. For low dosage, the BEP stage begins to operate with $p = 1.5$. This suggests that at the beginning of the reconstruction there are both large and small differences, with no predominance of one over the other. As the edges become better defined, the l_p norm can go to $p = 2$, smoothing the small differences. This is, in fact, an inference and further study should be performed on this topic as future work.

Finally, in Section 2.3 we proposed a new two-stage model with fidelity of l_2 norm and restriction of adaptive l_p norm, $1 \leq p \leq 2$. Initial tests were conducted with promising results. Therefore, we suggest as future work the optimization and implementation of an algorithm, possibly using soft threshold filtering, that promotes the reconstruction of CT images benefiting from the adaptive norm l_p, as suggested by the proposed method, but with two stages.

References

ANDERSEN, A.; KAK, A. Simultaneous algebraic reconstruction technique (sart): A superior implementation of the art algorithm. *Ultrasonic Imaging.*, v. 6, n. 1, p. 81 – 94, 1984. ISSN 0161-7346. Cited 3 times in pages 40, 50, and 72.

BAO, P.; ZHOU, J.; ZHANG, Y. Few-view ct reconstruction with group-sparsity regularization. *International Journal for Numerical Methods in Biomedical Engineering*, v. 34, n. 9, p. e3101, 2018. Available in: <https://onlinelibrary.wiley.com/doi/abs/10.1002/cnm.3101>. Cited 4 times in pages 40, 41, 45, and 60.

BRODY, A. S.; FRUSH, D. P.; HUDA, W.; BRENT, R. L. Radiation risk to children from computed tomography. *Pediatrics*, American Academy of Pediatrics, v. 120, n. 3, p. 677–682, 2007. ISSN 0031-4005. Available in: <https://pediatrics.aappublications.org/content/120/3/677>. Cited in page 29.

CAMPONEZ, M. O.; SALLES, E. O. T.; SARCINELLI-FILHO, M. Super-resolution image reconstruction using nonparametric bayesian inla approximation. *IEEE Transactions on Image Processing*, v. 21, n. 8, p. 3491–3501, Aug 2012. ISSN 1057-7149. Cited 2 times in pages 42 and 49.

CARSON, R. E.; LANGE, K. E-m reconstruction algorithms for emission and transmission tomography. *Journal of Computer Assisted Tomography*, 1984. Cited in page 41.

CHARBONNIER, P.; BLANC-FERAUD, L.; AUBERT, G.; BARLAUD, M. Deterministic edge-preserving regularization in computed imaging. *IEEE Transactions on Image Processing*, v. 6, n. 2, p. 298–311, Feb 1997. Cited 5 times in pages 38, 41, 44, 51, and 61.

CHOUDHARY, C.; MALIK, R.; CHOI, A.; WEIGOLD, W. G.; WEISSMAN, G. Effect of adaptive statistical iterative reconstruction on coronary artery calcium scoring. *Journal of the American College of Cardiology*, v. 63, n. 12, p. A1157, 2014. ISSN 0735-1097. Available in: <http://www.sciencedirect.com/science/article/pii/S0735109714611578>. Cited 3 times in pages 41, 42, and 49.

CLARK, D. P.; LEE, C.-L.; KIRSCH, D. G.; BADEA, C. T. Spectrotemporal ct data acquisition and reconstruction at low dose. *Medical Physics*, v. 42, n. 11, p. 6317–6336, 2015. Available in: <https://aapm.onlinelibrary.wiley.com/doi/abs/10.1118/1.4931407>. Cited in page 41.

COSTELLO, J. E.; CECAVA, N. D.; TUCKER, J. E.; BAU, J. L. Ct radiation dose: Current controversies and dose reduction strategies. *American Journal of Roentgenology*, American Roentgen Ray Society, v. 201, 2013. ISSN 0361-803X. Available in: <https://doi.org/10.2214/AJR.12.9720>. Cited in page 29.

CUI, X.; YU, H.; WANG, G.; MILI, L. Total variation minimization-based multimodality medical image reconstruction. In: . [S.l.: s.n.], 2014. v. 9212. Cited in page 60.

DAUBECHIES, I.; DEFRISE, M.; MOL, C. D. An iterative thresholding algorithm for linear inverse problems with a sparsity constraint. *Communications on Pure and Applied*

Mathematics, v. 57, n. 11, p. 1413–1457, 2004. Cited 8 times in pages 36, 37, 44, 45, 50, 51, 54, and 73.

DEáK, Z.; GRIMM, J. M.; TREITL, M.; GEYER, L. L.; LINSENMAIER, U.; KöRNER, M.; REISER, M. F.; WIRTH, S. Filtered back projection, adaptive statistical iterative reconstruction, and a model-based iterative reconstruction in abdominal ct: An experimental clinical study. *Radiology*, v. 266, n. 1, p. 197–206, 2013. Cited 2 times in pages 41 and 72.

ELBAKRI, I. A.; FESSLER, J. A. Statistical image reconstruction for polyenergetic x-ray computed tomography. *IEEE Transactions on Medical Imaging*, v. 21, 2., February 2002. Cited 3 times in pages 35, 41, and 50.

FARSIU, S.; DIRK, M.; ELAD, M.; ; MILANFAR, P. Fast and robust multiframe super resolution. *IEEE Trans. Image Process*, v. 13(10), p. 1327–1344, 2004. Cited in page 51.

FLORES, L.; VIDAL, V.; VERDú, G. Iterative reconstruction from few-view projections. *Procedia Computer Science*, v. 51, p. 703 – 712, 2015. ISSN 1877-0509. International Conference On Computational Science, ICCS 2015. Available in: <http://www.sciencedirect.com/science/article/pii/S1877050915009965>. Cited 2 times in pages 40 and 41.

GE, W.; MING, J. Ordered-subset simultaneous algebraic reconstruction techniques (os-sart). *Journal of X-Ray Science and Technology*, v. 12, n. 3, p. 169 – 177, 2004. Cited 2 times in pages 40 and 55.

GORDON, R.; BENDER, R.; HERMAN, G. T. Algebraic reconstruction techniques (art) for three-dimensional electron microscopy and x-ray photography. *Journal of Theoretical Biology*, v. 29, n. 3, p. 471–481, 1970. Cited in page 40.

GU, P.; JIANG, C.; JI, M.; ZHANG, Q.; GE, Y.; LIANG, D.; LIU, X.; YANG, Y.; ZHENG, H.; HU, Z. Low-dose computed tomography image super-resolution reconstruction via random forests. *Sensors*, v. 19, n. 1, 2019. ISSN 1424-8220. Available in: <http://www.mdpi.com/1424-8220/19/1/207>. Cited 3 times in pages 42, 45, and 49.

HANSEN, P. C.; SAXILD-HANSEN, M. Air tools - a matlab package of algebraic iterative reconstruction methods. *Journal of Computational and Applied Mathematics*, v. 236), p. 2167–2178, 2012. Cited 4 times in pages 46, 55, 61, and 68.

HEISENBERG, W. Über den anschaulichen inhalt der quantentheoretischen kinematik und mechanik". *Zeitschrift für Physik*, v. 43, n. 3-4, p. 127–198, 1927. Cited in page 40.

HINES, W. W.; MONTGOMERY, D. C.; GOLDSMAN, D. M.; BORROR, C. M. Probability and statistics in engineering. In: *Probability and Statistics in Engineering*. 4th. ed. [S.l.]: Jhon Wiley and Sons, Inc., 2003. cap. 7, p. 153–154. Cited 2 times in pages 47 and 60.

HORN, B. K. P. Fan-beam reconstruction methods. *Proc. IEEE*, v. 67, p. 1616–1623, 1979. Cited 2 times in pages 39 and 72.

HSIEH, J. Computed tomography - principles, design, artifacts and recent advances. In: *Computed Tomography - Principles, Design, Artifacts and Recent Advances*. 2nd. ed. Bellingham, Washington USA: Wiley Inter-science, 2009. cap. 2, p. 23–54. Cited 2 times in pages 30 and 32.

HSIEH, J. Computed tomography - principles, design, artifacts and recent advances. In: *Computed Tomography - Principles, Design, Artifacts and Recent Advances*. 2nd. ed. Bellingham, Washington USA: Wiley Inter-science, 2009. cap. 2, p. 29–30. Cited in page 35.

HSIEH, J. Computed tomography - principles, design, artifacts and recent advances. In: *Computed Tomography - Principles, Design, Artifacts and Recent Advances*. 2nd. ed. Bellingham, Washington USA: Wiley Inter-science, 2009. cap. 3, p. 56–117. Cited 5 times in pages 39, 40, 41, 42, and 72.

KIM, J. H.; CHOO, K. S.; MOON, T. Y.; LEE, J. W.; JEON, U. B.; KIM, T. U.; HWANG, J. Y.; YUN, M.-J.; JEONG, D. W.; LIM, S. J. Comparison of the image qualities of filtered back-projection, adaptive statistical iterative reconstruction, and model-based iterative reconstruction for ct venography at 80 kvp. *European Radiology*, v. 26, n. 7, p. 2055–2063, Jul 2016. Cited 3 times in pages 41, 60, and 72.

KIM, Y. Y.; SHIN, H. J.; KIM, M. J.; LEE, M.-J. Comparison of effective radiation doses from x-ray, ct, and pet/ct in pediatric patients with neuroblastoma using a dose monitoring program. *Diagnostic and interventional radiology*, Turkish Society of Radiology, v. 22, 2016. ISSN 1305-3825. Cited in page 29.

LANGE, K.; BAHN, M.; LITTLE, R. A theoretical study of some maximum likelihood algorithms for emission and transmission tomography. *IEEE Transactions on Medical Imaging*, 1987. Cited in page 41.

LAURITSCH, G.; BRUDER, H. *Head Phantom*. 2016. Available in: <http://www.imp.uni-erlangen.de/phantoms/head/head.html>. Cited in page 46.

MAN, B. D.; NUYTS, J.; DUPONT, P.; MARCHAL, G.; SUETENS, P. Reduction of metal streak artifacts in x-ray computed tomography using a transmission maximum a posteriori algorithm. *IEEE Transactions on Nuclear Science*, v. 47, Jun 2000. Cited in page 41.

MAN, B. D.; NUYTS, J.; DUPONT, P.; MARCHAL, G.; SUETENS, P. An iterative maximum-likelihood polychromatic algorithm for ct. *IEEE Transactions on Medical Imaging*, v. 20, n. 10, p. 999–1008, Oct 2001. Cited in page 41.

MathWorks®. *phantom Documentation*. 1994. Available in: <https://www.mathworks.com/help/images/ref/phantom.html>. Cited in page 46.

MathWorks®. *checkerboard Documentation*. 1998. Available in: <https://www.mathworks.com/help/images/ref/checkerboard.html>. Cited in page 46.

MAYO-SMITH, W. W.; HARA, A. K.; MAHESH, M.; SAHANI, D. V.; PAVLICEK, W. How i do it: Managing radiation dose in ct. *Radiology*, v. 273, n. 3, p. 657–672, 2014. PMID: 25420167. Available in: <https://doi.org/10.1148/radiol.14132328>. Cited in page 29.

MIGLIORETTI, D. L.; JOHNSON, E.; WILLIAMS, A.; GREENLEE, R. T.; WEINMANN, S.; SOLBERG, L. I.; FEIGELSON, H. S.; ROBLIN, D.; FLYNN, M. J.; VANNEMAN, N.; SMITH-BINDMAN, R. The Use of Computed Tomography in Pediatrics and the Associated Radiation Exposure and Estimated Cancer RiskComputed Tomography in PediatricsComputed Tomography in Pediatrics.

JAMA Pediatrics, v. 167, n. 8, p. 700–707, 08 2013. ISSN 2168-6203. Available in: <https://doi.org/10.1001/jamapediatrics.2013.311>. Cited in page 29.

NEWMAN, B.; CALLAHAN, M. J. Alara (as low as reasonably achievable) ct 2011—executive summary. *Pediatric Radiology*, v. 41, n. 2, p. 453, Aug 2011. ISSN 1432-1998. Available in: <https://doi.org/10.1007/s00247-011-2154-8>. Cited in page 29.

PAN, J.; ZHOU, T.; HAN, Y.; JIANG, M. Variable weighted ordered subset image reconstruction algorithm. *International Journal of Biomedical Imaging*, v. 2006, p. 7 pages, 2006. Cited in page 40.

PEARCE, M. S.; SALOTTI, J. A.; LITTLE, M. P.; MCHUGH, K.; LEE, C.; KIM, K. P.; HOWE, N. L.; RONCKERS, C. M.; RAJARAMAN, P.; CRAFT, A. W.; PARKER, L.; GONZáLEZ, A. B. de. Radiation exposure from ct scans in childhood and subsequent risk of leukaemia and brain tumours: a retrospective cohort study. *The Lancet*, v. 380, n. 9840, p. 499 – 505, 2012. ISSN 0140-6736. Available in: <http://www.sciencedirect.com/science/article/pii/S0140673612608150>. Cited in page 29.

PERELLI, A.; LEXA, M. A.; CAN, A.; DAVIES, M. E. Denoising message passing for x-ray computed tomography reconstruction. *CoRR*, abs/1609.04661, 2016. Available in: <http://arxiv.org/abs/1609.04661>. Cited in page 42.

RABIE, T. Robust estimation approach for blind denoising. *IEEE Transactions on Image Processing*, v. 14, n. 11, p. 1755–1765, Nov 2005. Cited in page 51.

SCHALLER, S. *Abdomen Phantom.* 2016. Available in: <http://www.imp.uni-erlangen.de/phantoms/index.htm>. Cited in page 46.

SHEPP, L. A.; LOGAN, B. F. The fourier reconstruction of a head section. *IEEE Trans. Nucl. Sci.*, NS-21 pp, p. 21–43, 1973. Cited 3 times in pages 39, 46, and 72.

SMITH-BINDMAN, R.; WANG, Y.; CHU, P.; CHUNG, R.; EINSTEIN, A. J.; BALCOMBE, J.; COCKER, M.; DAS, M.; DELMAN, B. N.; FLYNN, M.; GOULD, R.; LEE, R. K.; YELLEN-NELSON, T.; SCHINDERA, S.; SEIBERT, A.; STARKEY, J.; SUNTHARALINGAM, S.; WETTER, A.; WILDBERGER, J. E.; MIGLIORETTI, D. L. International variation in radiation dose for computed tomography examinations: prospective cohort study. *BMJ*, BMJ Publishing Group Ltd, v. 364, 2019. ISSN 0959-8138. Available in: <https://www.bmj.com/content/364/bmj.k4931>. Cited 2 times in pages 29 and 45.

SNYDER, D. L.; HELSTROM, C. W.; LANTERMAN, A. D.; FAISAL, M.; WHITE, R. L. Compensation for readout noise in ccd images. *J. Opt. Soc. Am.*, v. 12, n. 2, February 1995. Cited in page 41.

SODHI, K. S.; KRISHNA, S.; SAXENA, A. K.; SINHA, A.; KHANDELWAL, N.; LEE, E. Y. Clinical application of 'justification' and 'optimization' principle of alara in pediatric ct imaging: "how many children can be protected from unnecessary radiation?". *European Journal of Radiology*, Elsevier, v. 84, 2015. ISSN 0720-048X. Cited in page 29.

Sreehari, S.; Venkatakrishnan, S. V.; Wohlberg, B.; Buzzard, G. T.; Drummy, L. F.; Simmons, J. P.; Bouman, C. A. Plug-and-play priors for bright field electron tomography and sparse interpolation. *IEEE Transactions on Computational Imaging*, v. 2, n. 4, p. 408–423, Dec 2016. ISSN 2333-9403. Cited in page 42.

SUETENS, P. Fundamentals of medical imaging. In: *Fundamentals of Medical Imaging*. 2nd. ed. The Edinburgh Building, Cambridge CB2 8RU, UK: Cambridge University Press, 2009. cap. 3, p. 32–34. Cited in page 32.

SUN, Y.; CHEN, H.; TAO, J.; LEI, L. Computed tomography image reconstruction from few views via log-norm total variation minimization. *Digital Signal Processing*, v. 88, p. 172 – 181, 2019. ISSN 1051-2004. Available in: <http://www.sciencedirect.com/science/article/pii/S1051200418303658>. Cited 3 times in pages 42, 45, and 49.

SWINEHART, D. F. The beer-lambert law. *Journal of Chemical Education*, v. 39, n. 7, p. 333, 1962. Available in: <https://doi.org/10.1021/ed039p333>. Cited in page 31.

WANG, Z.; BOVIK, A. C.; SHEIKH, H. R.; SIMONCELLI, E. P. Image quality assessment: from error visibility to structural similarity. *IEEE Transactions on Image Processing*, v. 13, n. 4, p. 600–612, April 2004. Cited 3 times in pages 44, 62, and 65.

WHITING, B. R. Signal statistics in x-ray computed tomography. *Proc. SPIE*, v. 4682, p. 53–60, 2002. Cited 2 times in pages 41 and 44.

XU, Q.; MOU, X.; WANG, G.; SIEREN, J.; HOFFMAN, E. A.; YU, H. Statistical interior tomography. *IEEE Transactions on Medical Imaging*, v. 30, 5., May 2011. Cited 7 times in pages 35, 41, 42, 49, 50, 61, and 68.

YEUNG, A. *The "As Low As Reasonably Achievable" (ALARA) principle: a brief historical overview and a bibliometric analysis of the most cited publications*. 2019. 103-109 p. Available in: <https://doi.org/10.1051/radiopro/2019016>. Cited 3 times in pages 29, 39, and 45.

YU, H.; WANG, G. Compressed sensing based interior tomography. *Physics in Medicine and Biology*, 2009. Cited 4 times in pages 35, 41, 42, and 49.

YU, H.; WANG, G. Sart-type image reconstruction from a limited number of projections with the sparsity constraint. *International Journal of Biomedical Imaging*, v. 2010, p. 9 pages, 2010. Cited 2 times in pages 40 and 45.

YU, H.; WANG, G. A soft-threshold filtering approach for reconstruction from a limited number of projections. *PHYSICS IN MEDICINE AND BIOLOGY*, v. 1, n. 55, p. 3905–3916, 2010. Cited 5 times in pages 41, 42, 49, 57, and 58.

YU, H.; WANG, G. Sart-type half-threshold filtering approach for ct reconstruction. *Access, IEEE*, v. 2, p. 602–613, 2014. Cited 4 times in pages 40, 41, 45, and 55.

YU, Z.; NOO, F.; DENNERLEIN, F.; WUNDERLICH, A.; LAURITSCH, G.; HORNEGGER, J. Simulation tools for two-dimensional experiments in x-ray computed tomography using the forbild head phantom. *Physics in Medicine and Biology*, v. 57, n. 13, p. N237, 2012. Cited in page 46.

ZENG, G. L. Medical image reconstruction: A conceptual tutorial. In: . 1st. ed. Beijing, China: Higher Education Press Beijing and Springer-Verlag Berlin Heidelberg, 2010. cap. 6, p. 126–171. Cited in page 38.

ZENG, X.; YANG, L. Mixed impulse and gaussian noise removal using detail-preserving regularization. *Optical Engineering*, v. 49, p. 9, 2010. Cited 3 times in pages 38, 51, and 61.

ZENG, X.; YANG, L. A robust multiframe super-resolution algorithm based on half-quadratic estimation with modified btv regularization. *Digital Signal Processing*, v. 1, n. 23, p. 98–109, 2013. Cited 4 times in pages 38, 42, 51, and 61.

Zhang, G.; Tzoumas, S.; Cheng, K.; Liu, F.; Liu, J.; Luo, J.; Bai, J.; Xing, L. Generalized adaptive gaussian markov random field for x-ray luminescence computed tomography. *IEEE Transactions on Biomedical Engineering*, v. 65, n. 9, p. 2130–2133, Sep. 2018. ISSN 0018-9294. Cited in page 41.

ZHU, Z.; PANG, S. Few-photon computed x-ray imaging. *Applied Physics Letters*, v. 113, n. 23, p. 231109, 2018. Cited 4 times in pages 41, 42, 45, and 49.

Appendix

APPENDIX A – Statistical data

A.1 SART+DGT and SART+BEP+DGT regular dosage reconstruction data

Table 3 – Maximum, minimum, mean, median and standard deviation for reconstructions with methods B (SART+DGT) and C (SART+BEP+DGT) according to box plot graphs in Figure 15.

Image	Method	SNR dB	Max	Min	Mean	Median	Standard deviation
FORBILD head	B	32	0.90288	0.90065	0.90168	0.90168	0.000490
	B	40	0.91026	0.90939	0.90987	0.90988	0.000165
	B	46	0.91129	0.91080	0.91108	0.91109	0.000094
	B	60	0.91152	0.91143	0.91148	0.91147	0.000018
	C	32	0.91824	0.91683	0.91751	0.91749	0.000287
	C	40	0.92325	0.92276	0.92298	0.92297	0.000115
	C	46	0.92394	0.92366	0.92379	0.92379	0.000056
	C	60	0.92411	0.92405	0.92408	0.92408	0.000012
Shepp-Logan	B	32	0.83690	0.83116	0.83370	0.83368	0.001144
	B	40	0.88843	0.88644	0.88748	0.88749	0.000422
	B	46	0.89714	0.89605	0.89656	0.89656	0.000192
	B	60	0.89974	0.89956	0.89964	0.89964	0.000036
	C	32	0.85839	0.85383	0.85615	0.85616	0.000925
	C	40	0.90113	0.89952	0.90038	0.90037	0.000325
	C	46	0.90793	0.90690	0.90730	0.90730	0.000152
	C	60	0.90975	0.90961	0.90968	0.90968	0.000028
FORBILD abdomen	B	32	0.92845	0.92496	0.92628	0.92595	0.001111
	B	40	0.97272	0.97142	0.97210	0.97209	0.000408
	B	46	0.97839	0.97792	0.97815	0.97816	0.000155
	B	60	0.98035	0.98025	0.98029	0.98029	0.000032
	C	32	0.93845	0.93640	0.93740	0.93757	0.000690
	C	40	0.97597	0.97522	0.97564	0.97564	0.000195
	C	46	0.97959	0.97928	0.97944	0.97946	0.000086
	C	60	0.98073	0.98067	0.98070	0.98070	0.000023
Checkerboard	B	32	0.77589	0.77138	0.77375	0.77420	0.001383
	B	40	0.86223	0.85968	0.86104	0.86113	0.000993
	B	46	0.87908	0.87775	0.87836	0.87838	0.000390
	B	60	0.88383	0.88369	0.88376	0.88376	0.000047
	C	32	0.86959	0.86622	0.86797	0.86791	0.001101
	C	40	0.92380	0.92282	0.92330	0.92328	0.000383
	C	46	0.93265	0.93205	0.93230	0.93227	0.000179
	C	60	0.93530	0.93520	0.93527	0.93529	0.000036

A.2 SART (A), SART+DGT (B), SART+BEP+DGT (C) and FBP (D) low dose reconstructions for FORBILD Head (FH) phantom and Shepp-Logan Head (SL) phantom

Table 4 – Comparison of CT reconstruction methods A, B, C and D for the FORBILD head and Shepp-Logan head phantom images using PSNR and SSIM metrics for 15 and 30 projections and SNR of 32, 46, and 60 dB. Each result is the mean of 101 executions of a particular testing case. The values in bold represent the highest value comparing methods A, B, C and D for PSNR or SSIM metrics, number of projections (15 or 30) and iterations (350, 700 or 1000). D* implies that the reconstruction by the FBP (D) method is independent of the number of iterations, since it is a direct (non-iterative) method.

Image	SNR (dB)	Method	PSNR metric						SSIM metric					
			30 projections			15 projections			30 projections			15 projections		
			k=350	700	1000	k=350	700	1000	k=350	700	1000	k=350	700	1000
FH	32	A	62.6576	62.6576	62.6576	61.3241	61.3241	61.3241	0.1096	0.1096	0.1096	0.1013	0.1013	0.1013
		B	**68.8981**	**69.0161**	**69.043**	67.3406	**67.4181**	**67.4202**	0.7236	0.7340	0.7368	0.6998	0.7112	0.7143
		C	68.8491	68.7420	68.5457	**67.4093**	67.0085	66.2663	**0.753**	**0.7624**	**0.7607**	**0.7292**	**0.7313**	**0.7203**
		D*		55.4141			54.0239			0.0242			0.0153	
	46	A	62.8480	62.8480	62.8480	61.3975	61.3975	61.3975	0.1327	0.1327	0.1327	0.1130	0.1130	0.1130
		B	70.3511	**70.9038**	**71.0856**	68.0724	68.4681	**68.6376**	0.8605	**0.8815**	**0.8876**	0.7985	0.8216	**0.8292**
		C	**70.5681**	70.7268	70.5159	**68.3913**	**68.4761**	68.1521	**0.8852**	0.9028	0.898	**0.8288**	**0.8394**	0.8361
		D*		57.1855			56.6594			0.0947			0.0581	
	60	A	62.8551	62.8551	62.8551	61.4002	61.4002	61.4002	0.1342	0.1342	0.1342	0.1136	0.1136	0.1136
		B	70.4422	**71.0466**	**71.2518**	68.1110	68.5327	**68.7161**	0.8679	**0.8899**	**0.8964**	0.8033	0.8274	**0.8356**
		C	**70.6733**	70.8539	70.6321	**68.4433**	**68.5563**	68.2407	**0.8919**	0.9100	0.9049	**0.8337**	**0.8450**	0.8420
		D*		57.3471			56.8668			0.1294			0.0850	
SL	32	A	64.5268	64.5268	64.5268	63.4489	63.4489	63.4489	0.1800	0.1800	0.1800	0.1604	0.1604	0.1604
		B	73.5586	**74.3921**	**74.6588**	70.7452	**71.812**	**72.2027**	0.9036	0.9151	0.9174	0.8433	0.8740	0.8831
		C	**74.0945**	74.0583	73.8128	**71.9549**	72.1447	71.5547	**0.9325**	**0.9358**	**0.9350**	**0.8938**	**0.9066**	**0.8989**
				61.7955			60.6799			0.0536			0.0281	
	46	A	64.5592	64.5592	64.5592	63.4619	63.4619	63.4619	0.1940	0.1940	0.1940	0.1661	0.1661	0.1661
		B	73.9486	**75.1170**	**75.5809**	70.8990	72.1570	**72.6781**	0.9298	0.9444	0.9477	0.8575	0.8917	0.9026
		C	**74.6383**	74.6475	74.3422	**72.2586**	**72.5832**	72.0034	**0.9542**	**0.9579**	**0.9572**	**0.9093**	**0.9251**	**0.9186**
		D*		62.8883			62.1892			0.1837			0.1176	
	60	A	64.5606	64.5606	64.5606	63.4625	63.4625	63.4625	0.1946	0.1946	0.1946	0.1663	0.1663	0.1663
		B	73.9636	**75.1504**	**75.6263**	70.9047	72.1699	**72.6975**	0.9309	0.9458	0.9491	0.8580	0.8925	0.9036
		C	**74.6588**	74.6647	74.3552	**72.2741**	**72.6033**	72.0213	**0.955**	**0.9587**	**0.9581**	**0.9099**	**0.9257**	**0.9193**
		D*		62.9774			62.2886			0.2103			0.1480	

A.3 SART (A), SART+DGT (B), SART+BEP+DGT (C) and FBP (D) low dose reconstructions for FORBILD Abdomen phantom and Checkerboard image

Table 5 – Comparison of CT reconstruction methods A, B, C and D for the SL (Shepp-Logan head) and FA (FORBILD abdomen) phantom images using PSNR and SSIM metrics for 15 and 30 projections and SNR of 32, 46, and 60 dB. Each result is the mean of 101 executions of a particular testing case. The values in bold represent the highest value comparing methods A, B, C and D for PSNR or SSIM metrics, number of projections (15 or 30) and iterations (350, 700 or 1000). D* implies that the reconstruction by the FBP (D) method is independent of the number of iterations, since it is a direct (non-iterative) method.

Image	SNR (dB)	Method	PSNR metric						SSIM metric					
			30 projections			15 projections			30 projections			15 projections		
			k=350	700	1000	k=350	700	1000	k=350	700	1000	k=350	700	1000
FA	32	A	62.6576	62.6576	62.6576	61.3241	61.3241	61.3241	0.1096	0.1096	0.1096	0.1013	0.1013	0.1013
		B	**76.1405**	**76.2478**	**76.2701**	74.4034	**74.5392**	**74.587**	0.8389	0.8452	0.8470	0.8277	0.8368	0.8403
		C	75.9859	75.8311	75.5142	**74.4987**	74.502	73.8998	**0.8522**	**0.8568**	**0.8548**	**0.8424**	**0.8506**	**0.8480**
		D*		59.5957			58.5678			0.0294			0.0145	
	46	A	68.1199	68.1199	68.1199	66.0941	66.0941	66.0941	0.1418	0.1418	0.1418	0.0942	0.0942	0.0942
		B	79.5257	**80.759**	**81.2113**	76.2466	77.2650	**77.8593**	0.9506	**0.9630**	0.9662	0.9147	0.9334	**0.9412**
		C	**79.7397**	79.7947	79.1235	**76.7531**	**77.7001**	76.634	**0.9589**	0.9625	**0.9572**	**0.9278**	**0.9418**	0.9318
		D*		61.3642			61.1689			0.2158			0.1337	
	60	A	68.1290	68.1290	68.1290	66.0973	66.0973	66.0973	0.1424	0.1424	0.1424	0.0947	0.0947	0.0947
		B	79.7982	**81.2432**	**81.8295**	76.3869	77.5277	**78.2139**	0.9564	**0.9692**	**0.9727**	0.9194	0.9390	**0.9473**
		C	**80.0246**	80.0840	79.3894	**76.9335**	**77.9510**	76.7656	**0.9634**	0.9665	0.9615	**0.9328**	**0.9468**	0.9356
		D*		61.5167			61.3604			0.3124			0.2162	
CB	32	A	58.2554	58.2199	58.1975	56.9565	56.9564	56.9564	0.0359	0.0359	0.0358	0.0268	0.0268	0.0268
		B	66.6515	**66.9395**	**67.0102**	**62.8740**	**63.4005**	**63.6129**	0.5835	0.6007	0.6040	0.3863	0.4125	0.4245
		C	**66.8209**	66.7835	66.6913	62.8678	62.6172	61.6882	**0.6813**	**0.6914**	**0.6901**	**0.4196**	**0.4546**	**0.4493**
		D*		53.7724			52.5913			0.0236			0.0139	
	46	A	58.4901	58.4881	58.4867	57.0766	57.0766	57.0766	0.0371	0.0371	0.0371	0.0276	0.0276	0.0276
		B	68.3423	69.3741	**69.8766**	63.6704	**64.6899**	**65.2349**	0.7273	0.7654	0.7766	0.4555	0.5073	0.5318
		C	**68.5364**	**68.7302**	68.5984	**63.9017**	64.0553	63.0975	**0.8310**	**0.8540**	**0.8542**	**0.5001**	**0.5626**	**0.5576**
		D*		55.3639			54.7455			0.0664			0.0463	
	60	A	58.5003	58.5002	58.5001	57.0810	57.0810	57.0810	0.0373	0.0373	0.0373	0.0276	0.0276	0.0276
		B	68.4032	**69.4816**	**70.0262**	63.7144	**64.7692**	**65.3402**	0.7387	0.7793	0.7914	0.4617	0.5166	0.5427
		C	68.5926	68.7858	68.6452	**63.9479**	64.1073	63.1332	**0.8402**	**0.8640**	**0.8644**	**0.5079**	**0.5714**	**0.5661**
		D*		55.5374			54.9247			0.1015			0.0630	

A.4 SART+DGT and SART+BEP+DGT low-dose reconstruction data

Table 6 – Maximum, minimum, mean, median and standard deviation for reconstructions with methods B (SART+DGT) and C (SART+BEP+DGT) according to box plot graphs in Figure 15.

Image	Method	SNR dB	Max	Min	Mean	Median	Standard deviation
Shepp-Logan	B	46	71.90717	71.88161	71.89587	71.89771	0.008409
	B	60	71.91477	71.91034	71.91222	71.91198	0.001509
	C	46	72.52158	72.47905	72.50213	72.50002	0.012305
	C	60	72.52684	72.51747	72.52046	72.52013	0.002728
FORBILD head	B	46	70.50175	70.46123	70.48382	70.48602	0.013098
	B	60	70.58128	70.57247	70.57714	70.57710	0.002610
	C	46	70.70697	70.64906	70.67387	70.67692	0.017415
	C	60	70.79360	70.78239	70.78839	70.78918	0.003182
FORBILD abdomen	B	46	77.06331	76.97629	77.03127	77.03865	0.027104
	B	60	77.25636	77.24148	77.24695	77.24677	0.004781
	C	46	77.53407	77.39273	77.46855	77.46626	0.041331
	C	60	77.72815	77.71099	77.72098	77.72212	0.005621
Checkerboard	B	46	68.11085	68.08280	68.09738	68.09688	0.007917
	B	60	68.15683	68.15127	68.15474	68.15496	0.001678
	C	46	68.52148	68.47624	68.50018	68.49863	0.013743
	C	60	68.56514	68.55833	68.56222	68.56244	0.002284